Optical Phase Coherence in the Adiabatic Rapid Passage Force

A Thesis Presented

by

Taichi Jason Inaki

to

The Graduate School

in Partial Fulfillment of the Requirements

for the Degree of

Master of Science

in

Physics and Astronomy

Stony Brook University

July 2017

Stony Brook University

The Graduate School

Taichi Jason Inaki

We, the thesis committee for the above candidate for the Master of Science degree, hereby recommend acceptance of this thesis.

Harold Metcalf – Thesis Advisor
Distinguished Teaching Professor, Department of Physics and Astronomy

Thomas K. Allison – Chairperson of Defense
Assistant Professor, Department of Physics and Astronomy & Chemistry

Dominik A. Schneble
Associate Professor, Department of Physics and Astronomy

Mengkun Liu
Assistant Professor, Department of Physics and Astronomy

This thesis is accepted by the Graduate School.

Charles Taber
Dean of the Graduate School

Abstract of the Thesis

Optical Phase Coherence in the Adiabatic Rapid Passage Force

by

Taichi Jason Inaki

Master of Science

in

Physics and Astronomy

Stony Brook University

2017

For decades, optical forces have been used in experiments to control the motion of atoms with great precision. However, in many of these experiments, the spontaneous emission rate of the chosen atom will limit the overall strength of the force. The use of a stimulated emission process to drive atoms back to the ground state, and recent studies have shown that the adiabatic rapid passage force (ARP) can be used to exhibit much greater forces on atoms than the radiative force.

ARP is familiar to the Nuclear Magnetic Resonance community, and we employ the same technique here with an optical pulse as opposed to a radio-frequency pulse. An ARP sequence in our experiment generally consists of synchronized, counter-propagating pulses that have their frequencies swept through resonance. The synchronization of these pulses plays a key role in the overall strength of the force, and we present an upgrade to our laser system that provides phase coherence to our optical fields. This phase locking mechanism has shown improvements in our results that now show resemblance to our numerical simulations in terms of the velocity dependence of the ARP force. We continue to explore this parameter space and force map as we look at the possibilities of our upgraded system.

Stony Brook University
The Graduate School

Taichi Jason Inaki

We, the thesis committee for the above candidate for the
Master of Science degree, hereby recommend
acceptance of this thesis.

Harold Metcalf

Harold Metcalf – Thesis Advisor
Distinguished Teaching Professor of Physics

Thomas K. Allison – Committee Chair
Assistant Professor of Physics & Chemistry

Mengkun Liu – Committee Member
Assistant Professor of Physics

Dominik A. Schneble – Committee Member
Associate Professor of Physics

This thesis is accepted by the Graduate School

Charles Taber
Dean of the Graduate School

In loving memory of my grandparents
Shigeru and Akiko.

Contents

List of Tables

List of Figures

Acknowledgements

I came to Stony Brook because of a short email from my quantum mechanics professor suggesting a possible grad school opportunity. We were using a certain book on "Laser Cooling and Trapping" in my undergraduate lab when the author's name happened to appear in this email. I would meet Hal Metcalf a few months after that and join his group in the Fall of 2015 with only some experience with atomic physics experiments. Hal helped me in countless ways in the past two years from the fundamentals of what I needed to know all the way up to making major upgrades to the setup so that we could get the results we started seeing as I wrote this thesis. I can't even begin to repay him for all he's done and will miss him greatly.

I'd like to thank my thesis committee for putting up with me the past two years. It originally began as Tom Allison, Mengkun Liu, and Abhay Deshpande who were a great help in guiding me through the process of completing an MSI project. Unfortunately, Abhay could not attend my defense due to scheduling conflicts with conferences over the summer, and I'd really like to thank Dominik Schneble for filling this role. This degree would not have been possible without this committee, and I will be forever grateful for their contributions. And I must mention Eden Figueroa and Tom Weinacht as well for their help and insights as well in this short time.

The grad students in the group welcomed me with open arms and were a huge help throughout this process. I need to begin with John Elgin for training a clueless newcomer like me, and landing a position at NIST-Boulder where I hope he continues to find success. Next, I thank Brian Arnold for putting up with me as we spent the last year getting the entire setup to behave and produce data as we rushed to get something out for DAMOP. I thank Yifan Fang and Xiaoyang Liu for the same reasons and wish them the best of luck moving forward with their degrees as well. And I also need to thank our visiting scholar, Marty Cohen, for all of expertise and insights regarding this experiment and could not have

gotten here without him.

The entire Stony Brook AMO division and a few other students also need mentioning as they became a network for discussing anything from physics, politics, arts, sports, and really anything else you can imagine. Spencer, Yusong, Vince, Brian, Ludwig, Mike, Arturo, Jun, Bertus, Mehdi, Sonali, Miles, Yuning, Oumarou, and Yuta. Congrats to Arthur and Rasmus for also just finishing, and always inviting me out for soccer each week.

Everyone always asked me why I moved from California out to Long Island just to go study physics. To be fair, I applied to Stony Brook sight unseen and ended up enrolling in classes before I even realized it. I can't mother and her side of the family enough for supporting me during my time on Long Island. I also only recently discovered that I had some roots here as my mother's sister spent several years at Stony Brook as my grandfather was looking at research positions at Brookhaven some decades ago. Truth sometimes really is stranger than fiction, and sometimes wonder if fate really exists.

Long Island meant I'd live near New York City as well and I absolutely took full advantage of that. Anyone that's talked to me knows that I'm a sports junkie, and this was an opportunity I couldn't let pass. I eventually got to go to the US Open at Flushing , and even meet some professional golfers while volunteering at a PGA Tour event. The message here is that you can never really expect everything that happens in life and should experience as much as possible before it's too late. Following this I will be living in Japan for several years teaching English to K-12 kids for the same reasons I just stated. Life is too short to let these chances go by so I'm going to go spread my wings and see the world while I can.

Chapter 1

Introduction

Enormous progress has been made in the field of laser cooling and trapping after four decades since the first inception of its experimental possibility [1–3]. As the field has grown, so too have its applications, ranging from high precision spectroscopy, producing degenerate Fermi gases, atomic clocks, and cooling molecules [4].

The radiative force, generally thought of as the primary means of slowing and cooling atoms, has a linear dependence upon the natural decay rate (γ) of any given atomic transition. As a result, the magnitude of this force is greatly limited by this single factor. However, other atom-light interactions have been shown to exhibit much greater forces on atoms. Stimulated emission, in place of the natural decay process, can produce a significantly greater force as demonstrated by both the bichromatic and adiabatic rapid passage (ARP) forces [5–7]. This thesis centers around the major upgrade to the ARP laser system in our lab in order to close the gap between the numerical simulations and the experimental results regarding the velocity dependence of the force [7].

In this chapter, I will discuss the basic properties of the interaction of light on neutral atoms as well as the traditional radiative force associated with this process. This will be followed by an introduction to the ARP force in Chapter 2 along with the numerical simulations and experimental results seen before the upgrade. Chapter 3 and onwards will look at the various experimental setups conceived and tested along with any remaining suggested upgrades to the system in the final chapter.

1.1 Two-Level Atoms

The most fundamental understanding of the atom-light interaction for a neutral atom in a monochromatic light field is derived from the two-level case of an atomic ground state and single excited state. This model will act as the foundation to understanding the motivation for exploring the ARP force. The following derivation will closely follow material seen in Ref. [8] and Ref. [9].

We begin with the time dependent Schrödinger equation:

$$\mathcal{H} = i\hbar \frac{d\psi}{dt} \tag{1.1}$$

$$\mathcal{H} = \mathcal{H}_0 + \mathcal{H}'(t) \tag{1.2}$$

where $\mathcal{H}_0$ represents the Hamiltonian for an atom in free space and $\mathcal{H}'(t)$ describes the time-dependent interaction with the light field. $\vec{\mathcal{E}} = \frac{1}{c}\frac{d\vec{A}}{dt}$ for the electric field of the light that couples the two levels together. We use the vector potential of the field, $\vec{A}(\vec{r},t)$ to write the canonical momentum $p + (e/c)\vec{A}(\vec{r},t)$. As a result, the original time dependent Schrödinger equation becomes:

$$\mathcal{H}\psi(r,t) = [\mathcal{H}_0 + \mathcal{H}'(t)] \sum_k c_k(t)\phi_k(\vec{r})e^{i\omega_{jk}t} \tag{1.3a}$$

$$= i\hbar \frac{\partial}{\partial t} \sum_k c_k(t)\phi_k(\vec{r})e^{i\omega_{jk}t} \tag{1.3b}$$

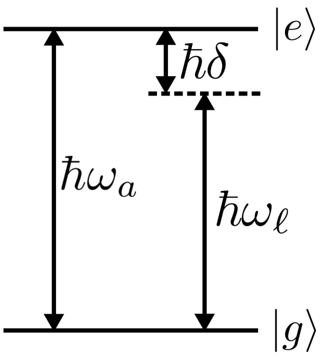

Figure 1.1: A diagram of a two-level atom with a ground state $|g\rangle$ and excited state $|e\rangle$. An energy separation of $\hbar\omega_a$ is shown based on the atomic resonance frequency (ω_a), and the laser frequency is represented by ω_ℓ with a detuning of δ below resonance. Modified from [10].

Here the ϕ_k's represent a complete set of eigenfunctions of $\mathcal{H}_0$ that allows the time-dependent wave function to be represented as in Eq. 1.3. Next we multiply by $\phi_k^*(t)$ on the left and integrate over all space. The result is:

$$i\hbar\frac{d}{dt}c_j(t) = \sum_k c_k(t)\mathcal{H}'_{jk}(t)e^{i\omega_{jk}t} \tag{1.4}$$

where

$$\mathcal{H}'_{jk}(t) \equiv \langle j|\mathcal{H}'(t)|k\rangle \tag{1.5}$$

However, this new form requires the use of some approximations in order to produce an analytic solution. For this experiment, we can consider a two-level problem since we are interested in a specific excitation for metastable helium (He*) using laser light of 1083.33 nm seen in Figure 1.1.

This two level scheme for this atom-light interaction will be coupled to laser light with a frequency ω_ℓ that has a detuning of $\delta \equiv \omega_\ell - \omega_a$ from the resonance frequency ω_a. The ground state or lower state can be denoted as $|g\rangle$ and the excited state as $|e\rangle$. As the atom oscillates between these two energy levels, a new wave function comprising these two states can be described as:

$$|\psi(t)\rangle = c_e(t)|e\rangle + c_g(t)|g\rangle \tag{1.6}$$

A well known problem named after I. I. Rabi arises as a result of this cycling of the atom between two states where the Schrödinger equation can be separated into a pair of coupled differential equations. Any diagonal elements of $\mathcal{H}'(t)$ will be included into $\mathcal{H}_0$, which leaves only $\mathcal{H}'_{eg}$ and $\mathcal{H}'_{ge}$:

$$i\hbar\dot{c_g}(t) = c_e(t)\mathcal{H}'_{ge}(t)e^{-i\omega_{jk}t} \tag{1.7a}$$

$$i\hbar\dot{c_e}(t) = c_g(t)\mathcal{H}'_{eg}(t)e^{i\omega_{jk}t} \tag{1.7b}$$

$\mathcal{H}'_{ge}$ can be written in a general form with time independent ($\mathcal{H}_0$) and dependent ($\mathcal{H}'(t)$) components:

$$\mathcal{H}_0 = p^2/2m + V \tag{1.8}$$

$$\mathcal{H}'(t) = -e\vec{\mathcal{E}}(\vec{r},t)\cdot\vec{r} \tag{1.9}$$

The laser wavelength driving this excitation is on the order of several hundreds of nanometers while the atomic wave function is contained within a sphere on the order of 1 nm. Thus, the assumption arises for treating the incoming light as a plane wave traveling in the z-direction, which allows the electric field operator to be treated as:

$$\vec{\mathcal{E}}(\vec{r},t) = E_0\hat{\epsilon}\cdot\cos(\omega_\ell t - \vec{k}\cdot\vec{z})e^{-i\phi} \tag{1.10}$$

This is known as the electric-dipole approximation and the time dependent Hamiltonian can now be written as:

$$\mathcal{H}'_{ge} = \hbar\Omega\cos(\omega_\ell t - \vec{k}\cdot\vec{z})e^{-i\phi} \tag{1.11}$$

With the complex Rabi frequency (Ω) defined as:

$$\Omega \equiv -\frac{eE_0}{\hbar}\hat{\epsilon} \cdot \langle e|\vec{r}|g\rangle \tag{1.12}$$

And the differential equations seen earlier now rewritten as:

$$\dot{c_g}(t) = -i\frac{\Omega e^{-i\phi}}{2}(e^{-i\omega_\ell t} + e^{i\omega_\ell t})e^{-i\omega_a t}c_e(t) \tag{1.13a}$$

$$\dot{c_e}(t) = -i\frac{\Omega^* e^{-i\phi}}{2}(e^{-i\omega_\ell t} + e^{i\omega_\ell t})e^{-i\omega_a t}c_g(t) \tag{1.13b}$$

A second approximation is now considered to further eliminate parameters that we will not consider in our experiment. At a glace, the solution for the coupled differential equations above include two time scales for the oscillation: $e^{\pm(-i\omega_\ell+\omega_a)t}$ (fast) and $e^{\pm(\omega_\ell-\omega_a)t}$ (slow). Integrating over time, the resulting demoninator term will include a $1/\omega_\ell \pm \omega_a$ term where ω_ℓ oscillates on the order of 10^{15} Hz while ω_a oscillates on the order of a hundreds of MHz. The rotating wave approximation (RWA) allows us to neglect terms on the order of $1/\omega_\ell$ and keeping smaller demoninator terms with $\delta = \omega_\ell - \omega_a$.

The remaining oscillation related to the atom is on a time scale more relevant to our experimental setup. And the differential equations can be further reduced to:

$$\dot{c_g}(t) = -\frac{i}{2}\Omega e^{-i\phi}c_e(t)e^{-i\delta t} \tag{1.14a}$$

$$\dot{c_e}(t) = -\frac{i}{2}\Omega e^{-i\phi}c_g(t)e^{-i\delta t} \tag{1.14b}$$

Given the initial conditions of $c_g(0) = 1$ and $c_e(0) = 0$, the solutions for these equations become:

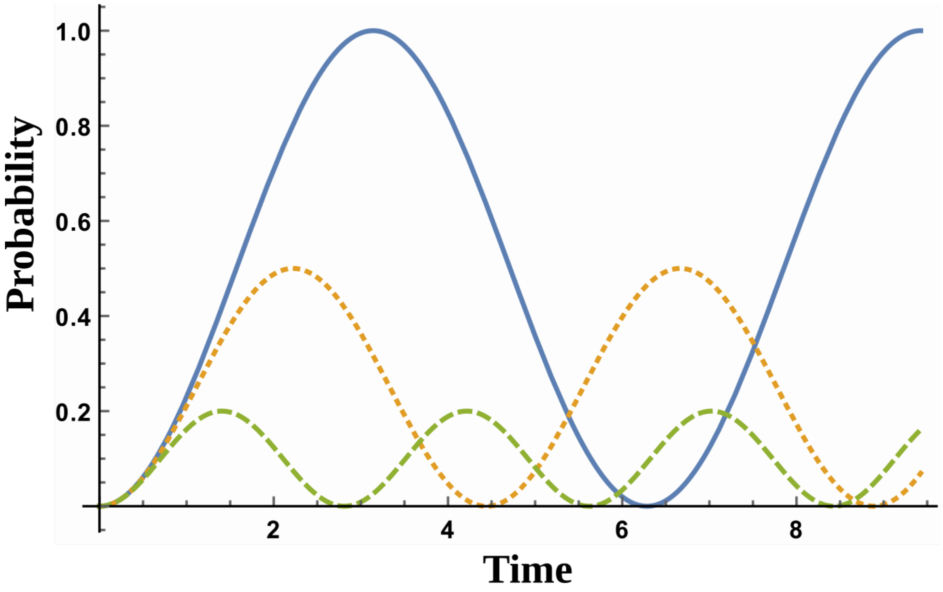

Figure 1.2: The probability of an atom being in excited state, $|c_e(t)|^2$ over time based on units of $1/|\Omega|$. The solid line describes the situation where there is no detuning from resonance, $\delta = 0$. The dotted line represents $\delta = |\Omega|$, and the dashed line represents $\delta = 2|\Omega|$. Figure from Ref. [7]

$$c_g(t) = \left(\cos\frac{\Omega' t}{2} - i\frac{\delta}{\Omega'}\sin\frac{\Omega' t}{2}\right)e^{i\delta t/2} \tag{1.15a}$$

$$c_e(t) = -i\frac{\Omega e^{i\phi}}{\Omega'}\sin\frac{\Omega' t}{2}e^{i\delta t/2} \tag{1.15b}$$

where

$$\Omega' \equiv \sqrt{|\Omega|^2 + \delta^2} \tag{1.16}$$

$|c_e(t)|^2$ represents the probability of the atom being in the excited state, which is described by Figure 1.2 that shows said probability as a function of time. The atom subsequently oscillates between the ground and excited states at the general Rabi frequency Ω'.

1.2 Optical Bloch Equations

The system now is described by a pair of complex amplitudes that provide information regarding the time-dependence of our atomic system. A density matrix formalism is appropriate for describing not just probabilities of being in the ground and excited states, but also the partial coherence, along with how it may affect the spontaneous emission process. This density matrix (ρ) based on complex amplitudes c_e and c_g can be written as:

$$\rho = |\psi\rangle\langle\psi| = \begin{pmatrix} |c_g|^2 & c_g c_e^* \\ c_e c_g^* & |c_e|^2 \end{pmatrix} = \begin{pmatrix} \rho_{gg} & \rho_{ge} \\ \rho_{eg} & \rho_{ee} \end{pmatrix} \tag{1.17}$$

When looking at the time evolution of this density matrix, a unique approach can be taken as shown by Feynman, et. al. [11] by considering a rotating coordinate system pictorially represented on a Bloch sphere. A state vector $\vec{R}$ that is confined to the surface of this unit sphere where:

$$|R(t)| = |c_e(t)|^2 + |c_g(t)|^2 \tag{1.18}$$

In this form, the excited state can be represented by the north pole and the ground state by the south pole. Anywhere else on the sphere is otherwise represented by a superposition state, where probability is conserved based on:

$$|c_e|^2 + |c_g|^2 = 1 \tag{1.19}$$

It is important to keep in mind that the Rabi frequency contains both real and imaginary components, which can generally be expressed as $\Omega = \Omega_{\text{Real}} + i\Omega_{\text{Imag}}$. Breaking down the Bloch vector into components can be done in terms of the Pauli matrices since a combination of the identity matrix $\mathcal{I}$ and the Pauli matricies span the two dimensional Hilbert space for a two state system [4].

$$\sigma_x = \begin{pmatrix} 0 & 1 \\ 1 & 0 \end{pmatrix}, \sigma_y = \begin{pmatrix} 0 & -i \\ i & 0 \end{pmatrix}, \sigma_z = \begin{pmatrix} 1 & 0 \\ 0 & -1 \end{pmatrix} \tag{1.20}$$

The expectation value for each component can be calculated using a basis wavefunction $\Psi\left(t\right) = c_g\left(t\right)\psi_g + c_e\left(t\right)\psi_e$:

$$\langle\sigma_x\rangle = \begin{pmatrix} c_e^* & c_g^* \end{pmatrix} \begin{pmatrix} 0 & 1 \\ 1 & 0 \end{pmatrix} \begin{pmatrix} c_e \\ c_g \end{pmatrix} = c_g^* c_e + c_e^* c_g = u \tag{1.21a}$$

$$\langle\sigma_y\rangle = \begin{pmatrix} c_e^* & c_g^* \end{pmatrix} \begin{pmatrix} 0 & i \\ -i & 0 \end{pmatrix} \begin{pmatrix} c_e \\ c_g \end{pmatrix} = i(c_g c_e^* - c_g^* c_e) = v \tag{1.21b}$$

$$\langle\sigma_z\rangle = \begin{pmatrix} c_e^* & c_g^* \end{pmatrix} \begin{pmatrix} 1 & 0 \\ 0 & -1 \end{pmatrix} \begin{pmatrix} c_e \\ c_g \end{pmatrix} = |c_e|^2 - |c_g|^2 = w \tag{1.21c}$$

and the time dependence of the Bloch vector and respective components can be represented by:

$$\frac{d\vec{R}}{dt} = \vec{\Omega} \times \vec{R} \tag{1.22}$$

$$\dot{u} = \Omega_{\text{Imag}} w - \delta v - (\gamma/2) u \tag{1.23a}$$

$$\dot{v} = -\Omega_{\text{Real}} w + \delta u - (\gamma/2) v \tag{1.23b}$$

$$\dot{w} = \Omega_{\text{Real}} v - \Omega_{\text{Imag}} u - \gamma(w + 1) \tag{1.23c}$$

Relaxation based on the natural decay rate (γ), whose inverse provides the lifetime for the

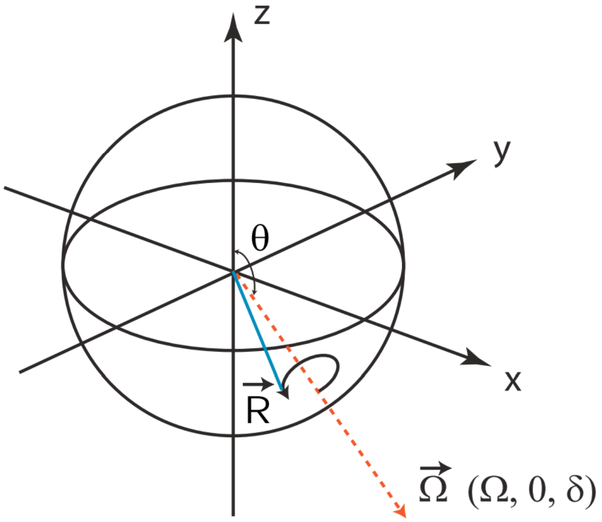

Figure 1.3: The projection of the Bloch and torque vectors onto the Bloch sphere. Here the Bloch vector ($\vec{R}$) is represented by the solid line precesses about the torque vector ($\vec{\Omega}$) is represented by the rotation centered on the dashed line. Figure from Ref. [6].

excited state. Collisions would play a role as another means of relaxation, but the likelihood of this occurring in the experiment is low enough to neglect it here. As the internal energy state of an atom changes, the spontaneous emission process can lead to a decoherence that will be discussed further in later sections.

1.3 Radiative Force

An atom with a mass M will interact with light through an absorption-emission process with light that carries a frequency of $\omega_\ell/2\pi$. It is necessary to conserve energy, linear momentum, and angular momentum. The energy from the light goes towards the excitation of the atom and the angular momentum is transferred to the orbital motion of the electron. Linear momentum transferred from the light to the atom results in a recoil of the atom with a velocity on the order of $\hbar k/M \sim 1$ cm/s. When the atom decays back down to the ground state this process can be repeated.

However, this method of producing a force on an atom largely depends upon the natural decay rate (γ) of the atom for a particular transition. Producing as large a force as possible depends upon how quickly this process can be repeated, which is limited by γ. This section will briefly discuss methods of exploiting this part of the atom-light interaction process.

The situation already mentioned paints most of the picture for the process involving the radiative force for stationary atoms. In order to complete the picture and further develop an understanding for atoms in motion, it becomes necessary to describe how momentum and energy are conserved by the system. The monochromatic light field with a well defined path of propagation produced by a laser source provides the key properties that allows one to address these questions.

Since the laser in this system operates at a fixed frequency, there will be a high probability to cause the atom to absorb this light. The laser beam's path of propagation will determine the direction in which the atom will receive a momentum kick of $\hbar k$ as the atom is raised to the excited state while the momentum imparted onto the atom by absorption is well defined, because of the symmetry of multiple spontaneous emission cycles there is to no net momentum exchange from decay.

A step-by-step description of a single absorption/emission event can be seen in Figure 1.4. The force experienced by the atom is proportional to both the momentum imparted onto the atom ($\hbar k$) and the scattering rate γ_p of the light from the laser field:

$$\vec{F}_{rad} = \gamma_p \hbar \vec{k} \tag{1.24}$$

$$\gamma_p = \gamma \rho_{ee} = \frac{s_0 \gamma / 2}{1 + s_0 + (2\delta/\gamma)^2} \tag{1.25}$$

s_0 represents the ratio of laser field intensity to the saturation intensity (I_s) of the particular

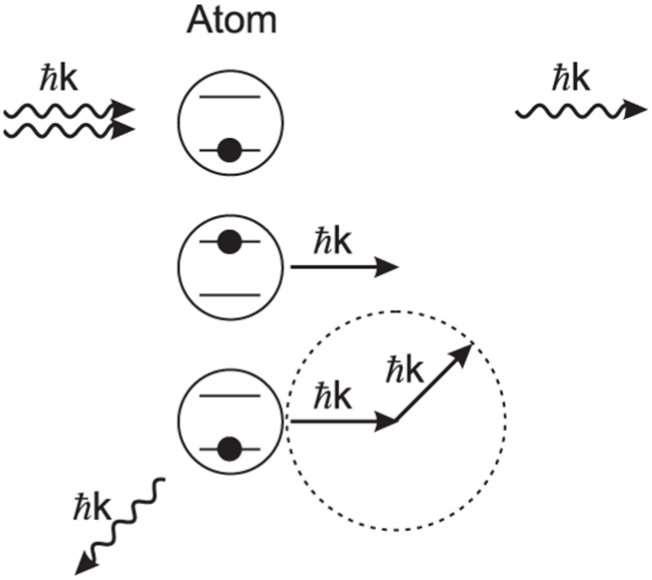

Figure 1.4: A diagram describing the step-by-step sequence for a single absorption/emission cycle. The atom begins in the ground state where upon absorbing light becomes driven into the excited state. Linear momentum of $\hbar k$ is then transferred to the atom along the initial light path. The atom will remain in the excited state for some amount of time and decay down to the ground state based on the natural decay rate of the transition (γ). During decay the atom will emit light in a random direction while undergoing a recoil that opposes the direction of the emitted light in order to conserve momentum. Over many cycles a net momentum change arises in the direction of the initial light path. Figure from Ref. [6] [7].

transition defined as:

$$s_0 \equiv 2\frac{|\Omega|^2}{\gamma^2} = \frac{I}{I_s} \quad \text{where} \quad I_s \equiv \frac{\pi h c}{3\lambda^3 \tau} \tag{1.26}$$

where λ and τ represent the wavelength and natural lifetime of the transition respectively. Subsequently, the radiative force can be written as:

$$\vec{F}_{rad} = \frac{\hbar \vec{k} s_0 \gamma/2}{1 + s_0 + (2\delta/\gamma)^2} \tag{1.27}$$

In the case of the transition becoming saturated, where $s_0 \gg 1$ and $s_0 \gg (2\delta/\gamma)^2$, which reduces $\vec{F}_{rad}$ to $\vec{F}_{rad,max} = \hbar\vec{k}\gamma/2$. But to reiterate, this model is only valid in the case of a stationary atom. In order to optically cool and trap atoms, a slightly different $\vec{F}_{rad}$ must now be considered to take into account the velocity of the atoms along with the Doppler shifts that consequently arise.

For an atom moving with a velocity, $\vec{v}$ in the laboratory frame of reference, a Doppler shift (ω_D) arises. This shift takes into account the frequency of the light field the atom sees compared to the lab frame frequency, $\omega_D = -\vec{k} \cdot \vec{v}$. Modifying the radiative force model for stationary atoms to now include these motional effects, $\vec{F}_{rad}$ can be written as:

$$\vec{F}_{rad} = \hbar\vec{k}\frac{s_0\gamma/2}{1 + s_0 + [2(\delta - \vec{k} \cdot \vec{v})/\gamma]^2} \tag{1.28}$$

Not all of the atoms will be traveling in the same direction as the path of the laser, but many will have a velocity component that is either the same or counter to said laser path. Thus, the effective detuning of the laser frequency is modified to include frequencies for both resonant and slightly non-resonant cases.

When the laser's path runs counter to the velocity of the atoms, the radiative force begins to oppose atomic motion. Slowing down an atomic beam becomes a possibility with this force, but a complication arises from this process. As these atoms are slowed, the resonance conditions of the system changes because the Doppler shift changes. One common method to compensate for this is to send the atoms through a spatially-varying magnetic field oriented along the atomic beam path. The resulting varying Zeeman shifts can be tuned to compensate for the effects of changing the Doppler shift, and maintain the resonance condition for the moving atoms [12].

With sufficiently slowed atoms, the cooling process can begin with multiple beams counter-propagating to oppose the motion of atoms in three directions. In the case where $s_0 \sim 1$, the forces produced by two counter-propagating beams in one dimension can be reduced to

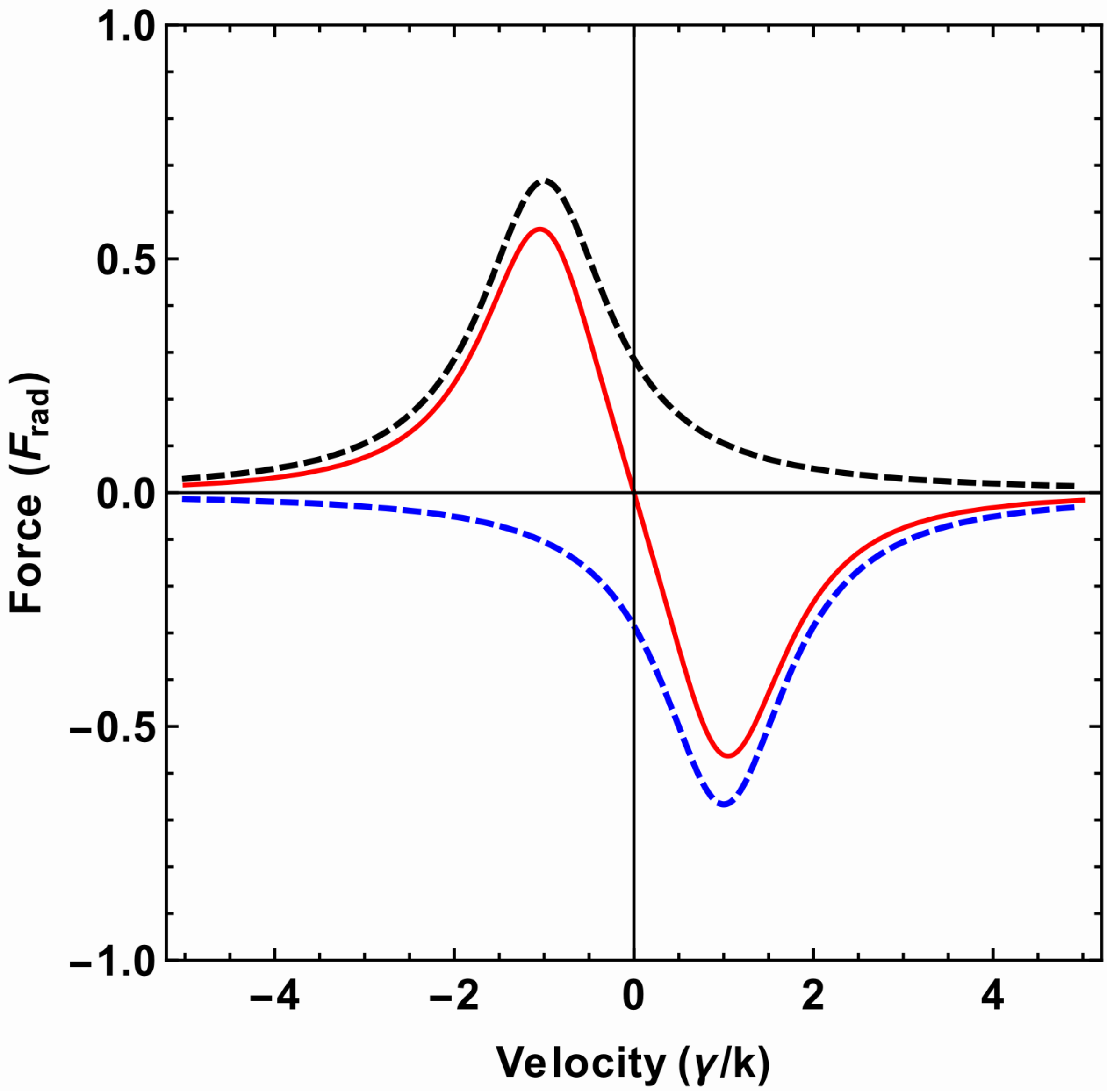

Figure 1.5: A plot of the force vs. velocity for an optical molasses setup for counter-propagating beams with parameters of $s_0 = 2$ and $\delta = -\gamma$. The dashed lines represent situations for each individual beam, which simply leads to a force on the atoms in the same direction, as the light as seen in the scattering example. The solid line represents the result of combining the two beams. For an atom with a velocity of $|v| < \gamma/k$, it will feel a damping force that opposes its motion and ultimately drive it to zero velocity. Figure from Ref. [7].

a single term:

$$\vec{F}_{rad} = \hbar\vec{k}\frac{s_0\gamma/2}{1+s_0+[2(\delta-\vec{k}\cdot\vec{v})/\gamma]^2} - \hbar\vec{k}\frac{s_0\gamma/2}{1+s_0+[2(\delta+\vec{k}\cdot\vec{v})/\gamma]^2} \tag{1.29a}$$

$$\vec{F}_{rad} \approx \frac{8\hbar k^2\delta s_0\vec{v}}{\gamma[1+s_0+(2\delta/\gamma)^2]^2} \equiv \beta\vec{v} \tag{1.29b}$$

When the laser is red-detuned below resonance ($\delta < 0$), the force opposes the atomic motion. Since this is a purely purely optical setup, it is named optical molasses since the atoms move through a viscous field of light.

However, a lower limit exists with this method of cooling as heating begins to influence atomic motion and absolute zero cannot be reached. With each absorption or emission event, the momentum of an interacting atom will change by discrete steps of $\hbar k$ while its kinetic energy will change on the order of the recoil energy. For a stationary atom, the resulting energy lost from the light field as a result of the absorption and emission events is a loss of $2\hbar\omega_{\text{recoil}}$. The atoms take on this energy in the form of kinetic energy, and thus constitutes heating. A competition between this heating and the damping force seen earlier leads to a steady state for the system where kinetic energy is nonzero, and the Doppler cooling limit arises for the special case of $\delta = -\gamma/2$ and $T_d = \hbar\gamma/2k_B$. It is typically on the order of hundreds of μK for atomic experiments [9].

Chapter 2

Adiabatic Rapid Passage

The nuclear magnetic resonance community has studied the ability to manipulate the spin orientation of atoms or molecules [13]. Central to this technique is a process known as Adiabatic Rapid Passage (ARP), which can be employed in the optical regime to invert the population of a two-level system. A light pulse whose frequency is swept through resonance (chirped) can be made to invert the atomic system and thereby produce a force considerable larger than the radiative force described earlier. A key requirement to this process involves a coherent exchange of momentum with the light beams such that a momentum change of $2\hbar k$ can be successfully imparted to the atoms [14].

2.1 What is Adiabatic Rapid Passage?

Any particular atomic transition will have a certain lifetime associated with the excited state denoted by $\tau \equiv 1/\gamma$. On average, atoms will undergo spontaneous emission after time τ has elapsed. With a chirped pulse sequence of duration π/ω_m that is shorter than τ ($\omega_m \gg \gamma$), but slower than either the peak Rabi frequency (Ω_0) or sweep range of the detuning (δ_0), adiabatic rapid passage (ARP) becomes possible. The inequality below summarizes the order of magnitude comparisons among the relevant frequencies:

$$\Omega_0 \approx \delta_0 \gg \omega_m \gg \gamma \tag{2.1}$$

The passage sequence is adiabatic since the process is slow enough for the system to adapt to the changing frequency while rapid enough to occur in less than τ. The Hamiltonian for this system can be written as:

$$\mathcal{H}(t) = \frac{\hbar}{2} \begin{pmatrix} \delta(t) & \Omega(t) \\ \Omega(t) & -\delta(t) \end{pmatrix} \tag{2.2}$$

Here $\delta(t)$ and $\Omega(t)$ represent the instantaneous detuning and Rabi frequency respectively. The eigenenergies of (2.2) are $E(t)_{\pm} = \pm(\hbar/2)\sqrt{\delta^2(t) + \Omega^2(t)}$. In the low-intensity domain ($\Omega < \delta$, but $\delta > 0$), the upper eigenstate approaches the ground state $|g\rangle$ while the lower approaches $|e\rangle$ [14]. The reverse case arises when $\delta < 0$. The dressed atom picture provides a tidy description of the population inversion of atomic states during an ARP sequence as seen in Figure 2.1.

A synchronized sweep of the detuning and Rabi frequency can be viewed as following the path on upper of the two eigenenergy sheets, and results in a population inversion [15]. The path along the lower sheet is not shown, but would represent the inversion in the opposite direction.

Another useful way to visualize an ARP sequence can be shown in a Bloch sphere diagram mentioned earlier but now adapted to depict an ARP sequence (Figure 2.2a). The south and north poles still respectively represent the ground and excited states, and the time dependence of the Bloch vector $\vec{R} = (u, v, w)$ is still given by $d\vec{R}/dt = \vec{\Omega}(t) \times \vec{R}(t)$ [16]. As

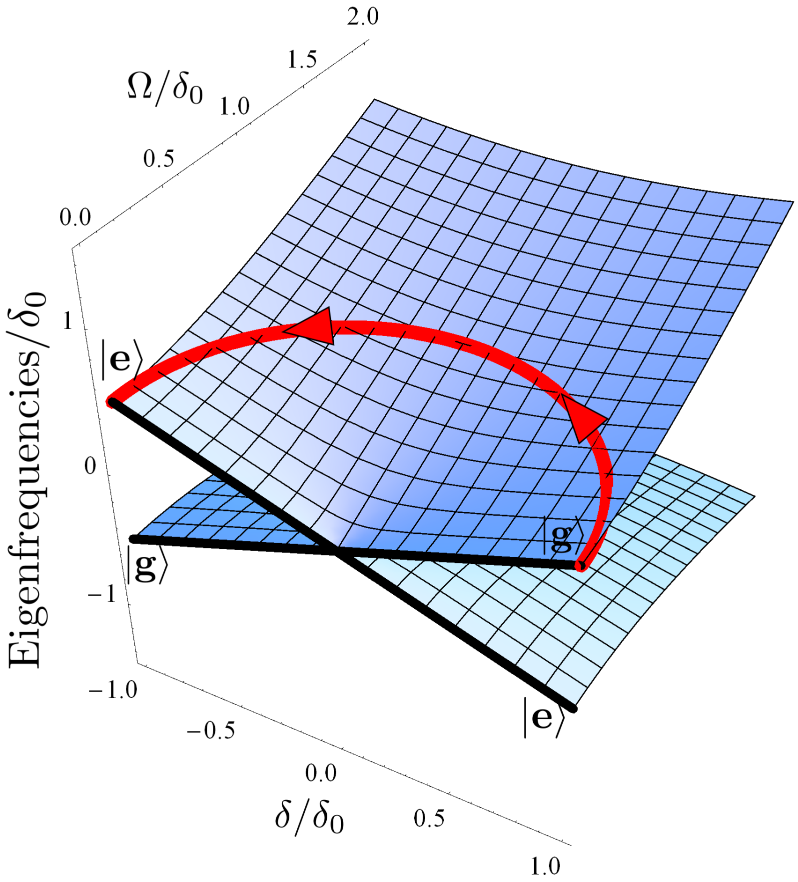

Figure 2.1: The dressed state representation showing energy sheets that are the eigenvalues of Eq. (2.2) as functions of Ω and δ. The upper energy sheet changes from $|g\rangle$ to $|e\rangle$ as δ changes from positive to negative. The curved path shown is a possible trajectory for ARP. Figure from Ref. [6].

the Bloch vector is raised from the ground to excited state it will precess around to $\Omega(t)$, but this can only occur while maintaining a slow enough frequency sweep.

The meaning of slow (adiabatic) can be quantitatively shown in terms of $\vec{\Omega}$ and the time derivative of the mixing angle, $\dot{\theta}(t)$:

$$|\vec{\Omega}(t)| \gg \frac{d\theta}{dt} \tag{2.3}$$

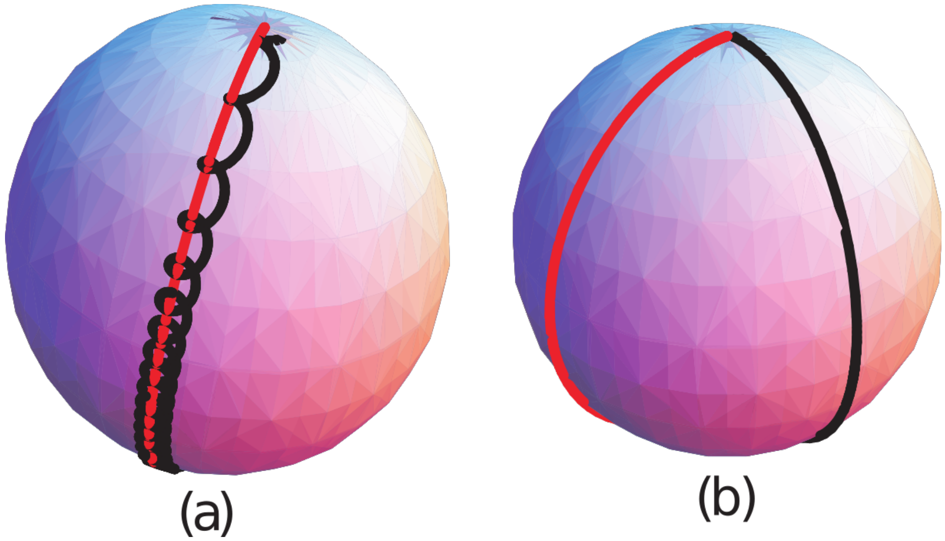

Figure 2.2: A plot showing the trajectories of the Bloch vector, $\vec{R}(t)$ in black, and the torque vector, $\vec{\Omega}(t)$ in red/gray. Part (a) is for $\delta \sim \Omega \gg \omega_m \gg \gamma$ and shows the spiral path taken by $\vec{R}$ as it precesses about Ω. ω_m represents the sweep frequency of the excitation, which needs to be slow enough to maintain an adiabatic process. Part (b) shows the case for $\omega_m \sim \delta_0 \sim \Omega_0$ in order to show population inversion is possible, and the resulting path becomes a simple arc. Figure from Ref. [6].

The mixing angle of eigenstates in the dressed-atom description is defined as $2\theta(t) \equiv \arctan(\delta(t)/\Omega(t))$. In the Bloch sphere description, this mixing angle is the angle between $\vec{\Omega}$ and the vector pointing to the north pole. The "adiabatic" part of ARP involves the condition requiring the angular frequency of the torque vector always being small compared to the angular frequency of the Bloch vector. The "rapid" part of ARP describes how the entire ARP process occurs faster than the natural relaxation process of the system.

2.2 ARP Force

Calculating the optical force from multiple ARP sequences experienced by the atoms can be performed using Newtons laws. The Ehrenfest Theorem simply demands that the expectation value of an operator must correspond to the behavior of its classical counterpart [9].

The force can be expressed in terms of the laser light pressure felt by an atom:

$$\vec{F} = \langle \vec{\mathcal{F}} \rangle = \frac{d}{dt} \langle \vec{p} \rangle \tag{2.4}$$

$\mathcal{F}$ represents a general quantum mechanical force operator. In the case of an ARP sequence, the force will be described in terms of the dressed atom Hamiltonian ($\mathcal{H}$), $\vec{\Omega}$ and $\vec{R}$:

$$\vec{F} = \langle -\nabla \mathcal{H} \rangle = \frac{\hbar}{2} (u \nabla \Omega_{\text{Real}} + v \nabla \Omega_{\text{Imag}}) \tag{2.5}$$

When considering the case of two counter-propagating pulses with a wavenumber k, only one dimension need be described and the force can be rewritten as:

$$\vec{F} = \frac{\hbar \vec{k}}{2} [(\vec{\Omega}_+ - \vec{\Omega}_-) \times \vec{R}]_z \tag{2.6}$$

where the force is given by the third component of the cross product. Ω_+ and Ω_- respectively represent the torque vectors of the right (+) and left (-) propagating fields. In the case of pulses that are not temporally overlapped, each pulse is not coupled to the other and can be treated individually. When only $\vec{\Omega}_+$ or $\vec{\Omega}_-$ is considered, the resulting force simplifies as:

$$\vec{F} = \frac{\hbar \vec{k}}{2} (\vec{\Omega}_\pm \times \vec{R})_z = \frac{\hbar \vec{k}}{2} \dot{w} \tag{2.7}$$

When $\dot{w}$ is discretized in steps of ω_m/π as the atoms are driven between the ground and excited states, the force becomes:

$$\vec{F} = \frac{\hbar \vec{k}}{2} (\vec{\Omega}_\pm \times \vec{R})_z = \frac{\hbar \vec{k}}{2} \frac{\omega_m}{\pi} \Delta w \tag{2.8}$$

And the ideal force experienced would be:

$$\vec{F}_{ARP} = \frac{\hbar\vec{k}\omega_m}{\pi} \tag{2.9}$$

2.2.1 Previous Results and Understanding Coherence

The most recent results from determining the velocity dependence of the ARP force showed significant discrepancies between numerical simulations and the experimental results. The simulations focused on integrating the optical Bloch equations to understand the trajectories taken by the atoms largely based on γ, Ω_0, δ_0, and the transverse velocities possible for the experiment. These results can be seen in Figures 2.3 and 2.4, which are further detailed in Ref. [7] and Ref. [16].

The experimental results show measured deflections corresponding to the simulations as δ_0 was varied to positive and negative deflections, but failed to produce a smooth force profile as seen inthe simulations. The immediate culprit that we pointed to was the use of two independent lasers that were each only frequency stabilized with no phase coherence between them. The effect of phase coherence between the two ARP laser fields became a prominent question that required further study in order to close the gap between simulation and experiment. When atoms are excited from the ground state and reach a point on the Bloch sphere that does not correspond exactly with the north pole (excited state), a superposition between ground and excited state results. When a second ARP pulse arrives to drives the atoms down through stimulated emission, it once again may not arrive back to the south pole (ground state) exactly.

Spontaneous decay on average will occur after a certain amount of time has passed based on the lifetime of the transition (τ), and this can be thought of as a spontaneous decay

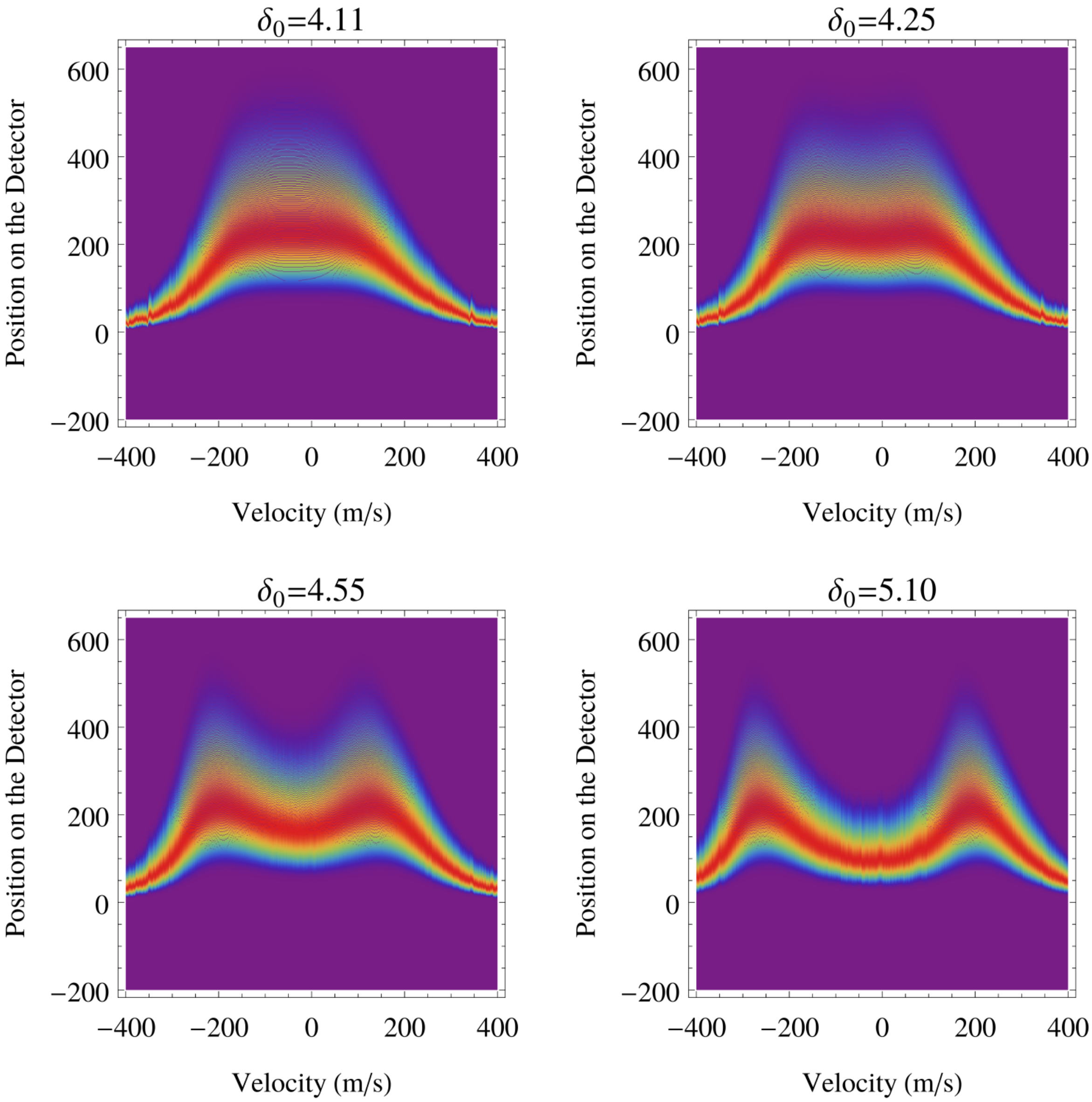

Figure 2.3: The simulation results as seen in Ref. [7] showing the force vs. velocity profiles with the spontaneous emission parameter included to represent what would be seen experimentally. The red color represents the highest number of atom detections while violet represents the least. The most prominent result was the central peak splitting into two as δ_0 increased, but experimental results would show otherwise.

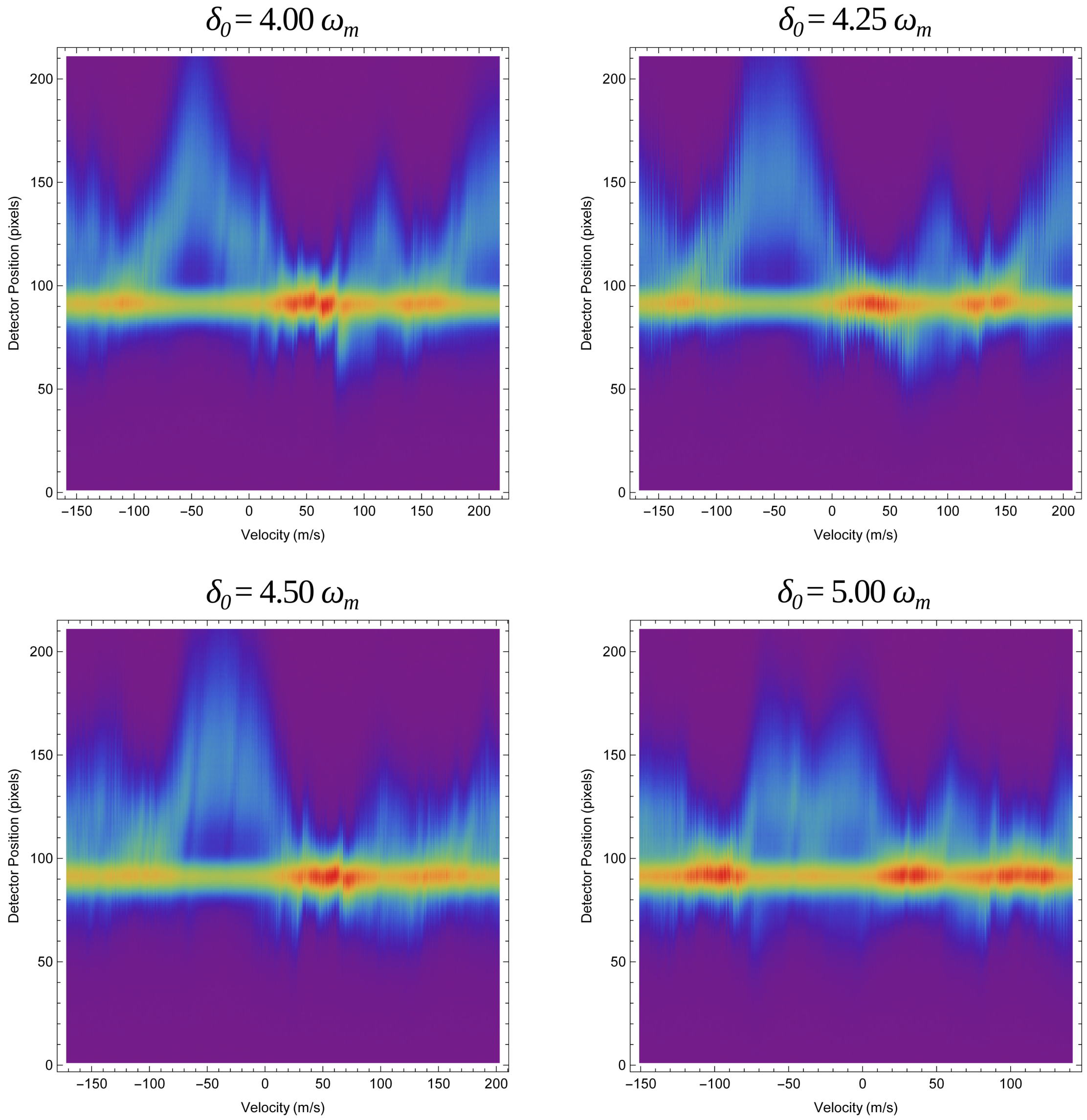
$\delta_0 = 4.00\ \omega_m$

$\delta_0 = 4.25\ \omega_m$

$\delta_0 = 4.50\ \omega_m$

$\delta_0 = 5.00\ \omega_m$

Figure 2.4: The experimental results as seen in Ref. [7] showing the force vs. velocity profile for $\Omega = 3.70\omega_m$ and various values of δ_0. The velocity dependence of ARP seen here immediately shows discrepancies with the simulation results even with comparable parameters.

clock. With a mixture of states, an ambiguity arises as to how this decay clock is treated, especially in the case of phase offsets introduced during an ARP sequence. It becomes difficult to determine whether or not the decay clock is reset to account for any excited state component of a superposition state.

2.2.2 Upgrade to Experimental Setup

How to tackle this issue concerning coherence is the central topic of this thesis: a major upgrade to the existing laser system that provides phase coherence between the ARP lasers. The two-laser system previously implemented will now include a master laser, frequency stabilized to the metastable helium reference, along with two slave lasers that are coherently phase locked to the master. A major experimental difficulty that was overcome in this thesis work was to reduce noise to a minimum due to the sensitivity of the phase locking mechanism.

We would find that the frequency locking system for the original DBR master laser along with the laser diode itself generated excessive phase noise such that major changes became necessary. In this thesis, I will discuss the various systems tested and implemented in order to simultaneously frequency lock the master laser to an atomic reference while phase locking two slave lasers to the master. The details of the final system are described in Chapter 5 of this thesis.

Chapter 3

Experimental Setup

The overall experimental setup consists of two major components: a frequency stabilization system for locking the master laser to the metastable He transition; and the setup for phase locking the two slave lasers to the master laser. The SAS setup simply requires infrared light with a wavelength of 1083.33065 nm from any laser source in order to fulfill its purpose. Likewise, the phase locking setup including the two slave lasers and connected phase locking electronics are in principle independent of the master laser in use. Various frequency stabilization techniques were tested with the goal in mind to simultaneously achieve a low-noise frequency lock to resonance and a phase lock between master and slave lasers. Each of these techniques will be discussed in later sections.

3.1 Frequency Stabilization

In order to prevent any fluctuations or long-term drift of the diodes' output frequency, a feedback mechanism is necessary for the laser to maintain its output frequency. A helium vapor cell serves as the atomic reference for locking the master laser to the $\lambda = 1083.33065$

nm (276.73219 THz) necessary for driving the $2^3S_1 \rightarrow 2^3P_2$ transition. This metastable state is achieved with an initial discharge provided by a high voltage RF signal of 51 MHz. In general, the temperature controller and current driver for the diode laser would respectively be set to 38.6^oC and 165 mA. The energy diagram for this process can be in Figure 3.1, and the along with the relevant parameters for the transition can be seen in Figure 3.1.

Transition	Energy (eV)	$\omega_a/2\pi$ (THz)	λ (nm)	$\gamma/2\pi$ (MHz)	τ (ns)	$\omega_r/2\pi$ (kHz)	I_s (mW/cm^2)	v_r (m/s)	γ/k (m/s)
$2^3S \rightarrow 2^3P$	1.14	276.7	1083.3	1.62	97.9	42.5	0.17	0.092	1.76

Table 3.1: Table of the atomic parameters of Helium relevant to the ARP experiment [17].

Before entering the vapor cell, the beam of the master laser goes through a flat piece of thick glass to provide a transmitted beam as well as two reflected beams. The glass transmits on the order of $> 90\%$ of the incoming beam while reflecting $< 5\%$ off each its front and back surfaces. The transmitted beam now carries considerably more power than either of the reflected beams, and thus will now act as the pump beam for the SAS setup. The two reflected beams now act as the probe and reference beams that will be counterpropagating against the pump beam. The pump beam is reflected off of a 50/50 beamsplitter and back through the cell overlapping with the probe beam. The probe and reference beams simply transmit through the cell and impinge upon a pair of detectors that provide the DC signal. The overall setup for this scheme is shown in Figure 3.3.

With some of the He atoms excited into the metastable state by the discharge, the pump beam can drive them into the 2^3P_2 state and saturate the transition, making equal populations in the ground and excited states. The probe beam that runs counter to the pump beam interacts with these same atoms and serves to cause a stimulated emission event upon some of the atoms that are excited. The PZT mirror in the laser cavity is driven with a triangular ramp on the order of 21 Hz to scan over the frequency range, and a Doppler-

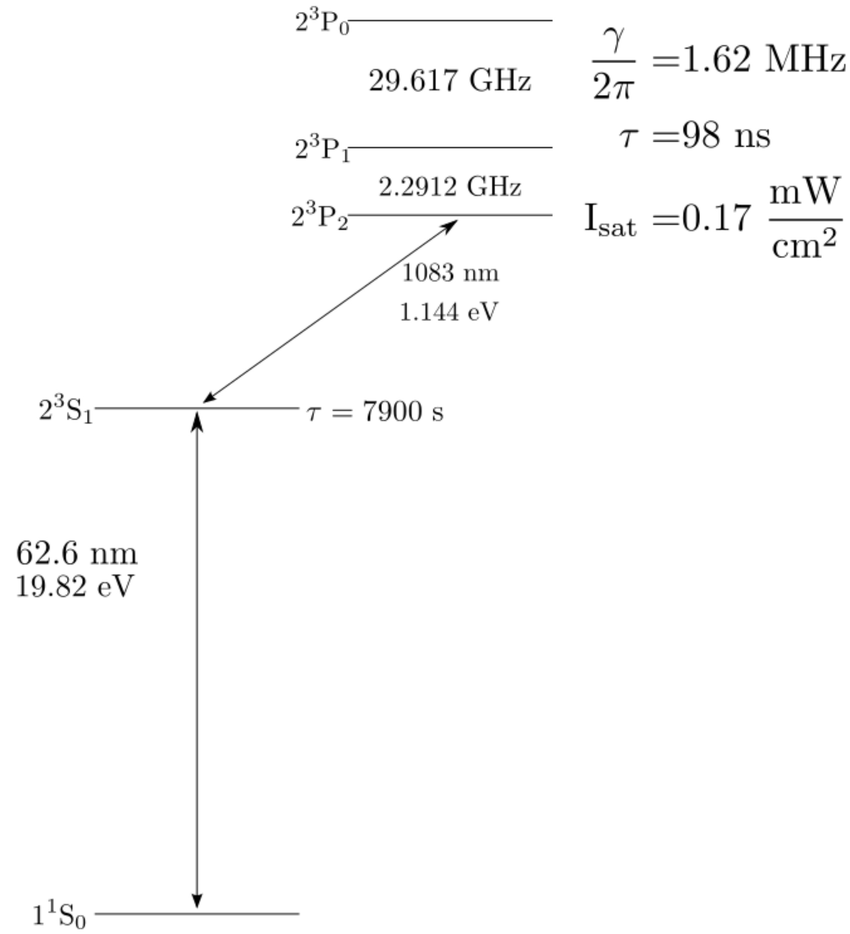

Figure 3.1: The energy level diagram for Helium relevant to our experiment. Helium atoms are prepared into the metastable 2^3S_1 state by our RF discharge in the SAS cell. The 2^3S_1 level with an average lifetime of approximately 7900 s becomes the ground state for our experiment. Figure from Ref. [7]. (Not to scale.)

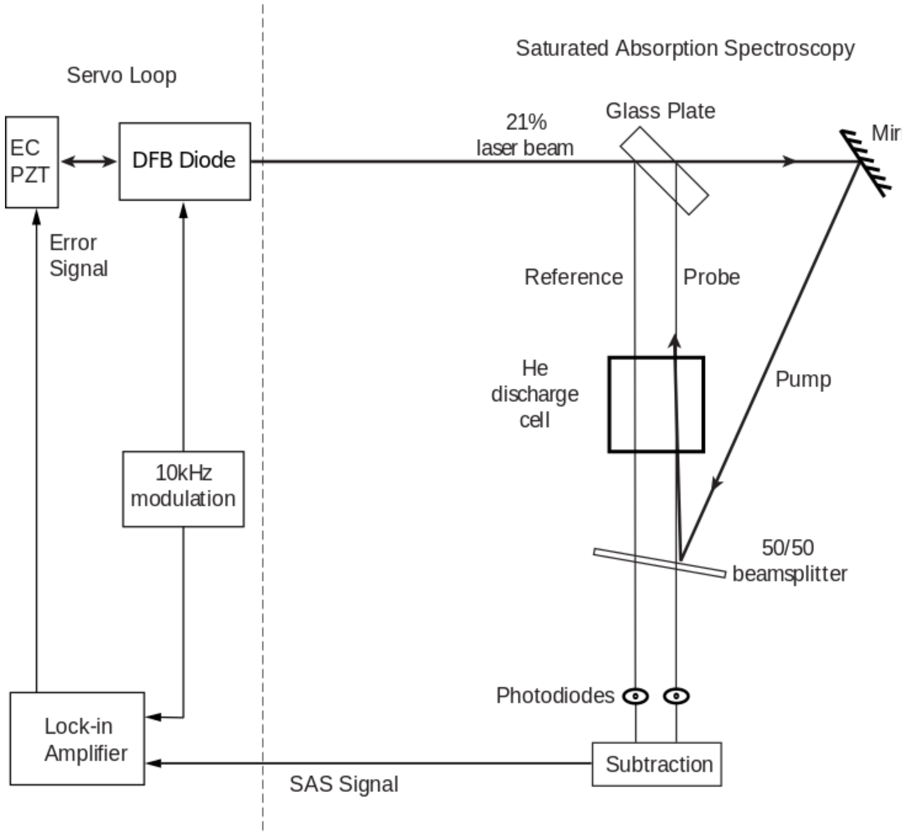

Figure 3.2: The frequency stabilization scheme originally used for locking the distributed feedback (DFB) master laser system to the $2^3S_1 \rightarrow 2^3P_2$ transition. The right of the dotted line represents the optical setup while the left side represents the electronics for the feedback loop that includes the extended cavity mirror (EC PZT). Figure modified from Ref. [6].

broadened saturation absorption profile appears as expected.

The reference beam acts as a baseline for the simple Doppler-broadened absorption profile with no saturation or stimulated emissions as it does not interact with the pump and probe beams in the vapor cell. The reference signal from its respective photodiode is subtracted from the signal on the probes detector to provide a Doppler-free SAS signal. This provides ann error signal for tuning the current into the master laser to the resonant frequency of the $2^3S_1 \rightarrow 2^3P_2$ transition and provides the first step towards stabilizing the lasers output to this frequency.

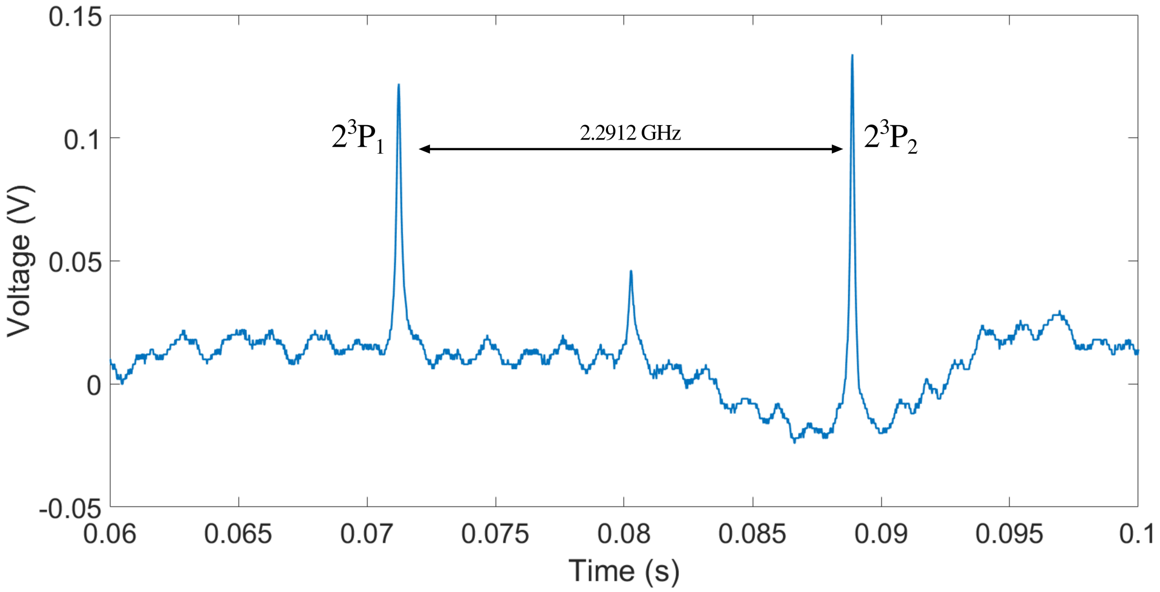

Figure 3.3: An oscilloscope trace of the saturated absorption spectroscopy signal for the $2^3S_1 \rightarrow 2^3P_2$ showing a nearby transition that sits 2.2912 GHz away from the 1083.33065 nm transition. Using a DL-100 laser for the spectroscopy, the peak of interest was measured to have a width of 20.8075 ± 0.2528 MHz, and the other to have a width of 33.8128 ± 0.2001 MHz. A weak crossover peak arises from the overlap of these two possible states.

The spectrum from a properly aligned SAS setup can be seen in [Figure SAS scope figure], which shows multiple transitions as opposed to just the one. As the PZT for the laser is swept some MHz around the 1083.33065 nm transition, a second transition is also visible. This second transition derives from the next closest fine structure transition ($J = 1 \rightarrow J = 1$), which sits around 2.2912 GHz away from the stronger transition ($J = 1 \rightarrow J = 2$). Using a DL-100 for the spectroscopy, the peak we are interested was measured to have a width of 20.8075 ± 0.2001 MHz, and the other was measured to be 33.8122 ± 0.2528 MHz wide. The resulting spectrum seen on an oscilloscope includes both of these transitions as well as a weak crossover peak between the two.

The ability to observe these transitions depends upon the linewidth of the master laser, which became clearly evident when comparing the different master laser systems that will be mentioned in the next chapters. An output that has too broad of a linewidth as seen with the Distributed Feedback (DFB) diode laser would allow only the most dominant peak to appear. A much narrower linewidth as seen with the Toptica DL-100 anti-reflection (AR) coated Fabry-Perot diode laser allowed the three peaks to appear in the same spectrum as shown.

In addition, the natural stability of the master laser played a key role in the phase locking process. The greater the drift in the laser's center frequency over time, the stronger the feedback signal became in order to maintain a frequency lock. Such large corrections would lead to much phase noise introduced to the phase locking mechanism, and thus caused difficulties in maintaining a phase lock for longer than the duration of the experiment.

3.2 Phase Locking

In the previous ARP experiment that focused on the velocity dependence of the ARP force [7], a pair of similar but independent lasers were frequency locked to the helium resonance and were used to impart a force onto helium atoms. When interacting with the atoms, each continuous wave (CW) beam is converted into a series of pulses by means of a phase modulator, intensity modulator, booster optical amplifier setup. More on the pulse production process is described in Ref. [7]. The two lasers send light in opposite directions, which will result in the momentum transfer that will maximize the ARP force. These pulses are designed to be long enough to meet the Adiabatic condition while short enough to be greater than τ.

The most prominent issue with that setup may have involved the independence of the original two lasers. One interpretation of the measured ARP force results could be that the pulses do not interact with the helium atoms coherently. In other words, the lack of coherence between the light in the pulses results in an incoherent excitation/de-excitation sequence. Some of the atoms could experience a force, but just not in accordance with the model of the numerical simulations. This coherence question is addressed with this new setup that includes phase coherence between the two light sources (slave lasers) that will provide the interaction with the helium atoms.

A simple analogy to describe a phase lock involves a pair of clocks. One of the clocks is store bought and has a radio antenna that is able to receive external signals. The other clock acts as the standard that all other clocks around the world will adjust their times such that they are considered accurate. As the store bought clock drifts over time due to mechanical or electrical design, it will need to be readjusted periodically. The reference clock will transmit a radio signal to the store bought clock to speed up or slow down.

Phase can be thought of as the drift in time seen with the store bought clock. The phase locked loop is represented by the feedback mechanism established between the store bought clock and reference clock that aims to establish a certain standard of time. We see this in the real world with the advent of atomic clocks, which have become the most accurate time standards in the world.

The phase locking process begins with mixing light from one of the slave lasers with the frequency locked master laser. Mixing is performed with fiber optic beam splitters that allow beams to either be split into various ratios or combined. The combinations used for our setup involved either 50/50 or 90/10 splitters, which allows us to control how much light goes to each part of the experiment in a compact setup with no free-space light beams. Combining beams was usually performed with 50/50 splitters where two beams would be combined and split into a pair of mixed beams with even power. A diagram of these splitters can be seen in Figure 3.4.

The master laser is stabilized through SAS during the phase locking process. The PZT

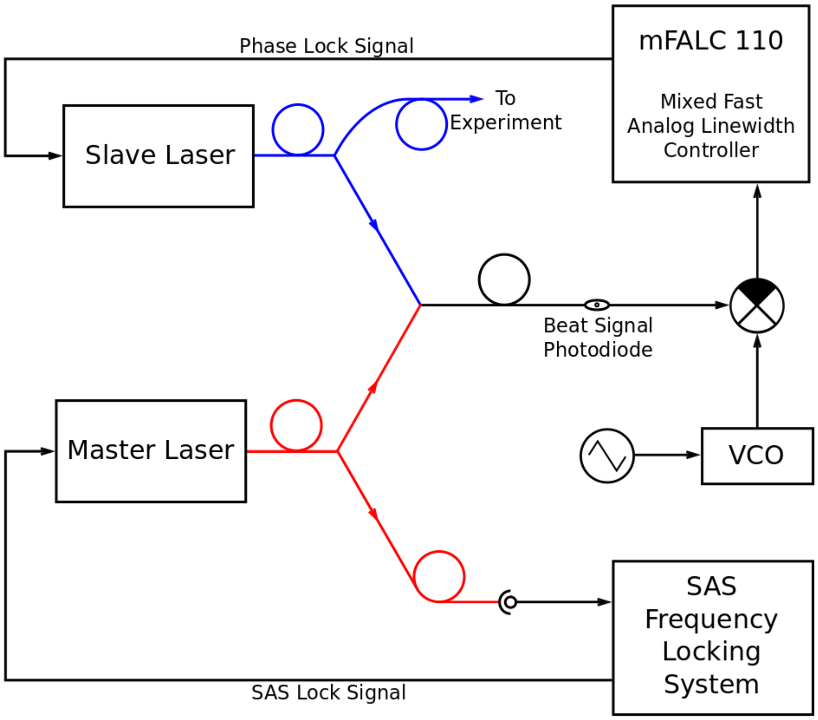

Figure 3.4: A general overview of the experimental setup that includes both the frequency stabilization setup for the master laser as well as the phase locking loop with a slave laser. In the actual experiment, two slave lasers are phase locked to the master laser simultaneously.

on either slave laser can be tuned to adjust the beat frequency it and the master up to the order of 300 MHz on a high-speed oscilloscope or a 2.5 GHz spectrum analyzer. The phase locking electronics in the mixed Fast Analog Controller (mFALC) are able to handle signals between 1 MHz and 300 MHz. The mFALC will lock the beat signal to a frequency based on the local oscillator sent to it. An example oscilloscope trace for this can be seen in Figure 3.5.

We also compare the results that used phase coherent light to phase incoherent light as a part of the investigation into the effects of phase on the ARP force. For one master-slave

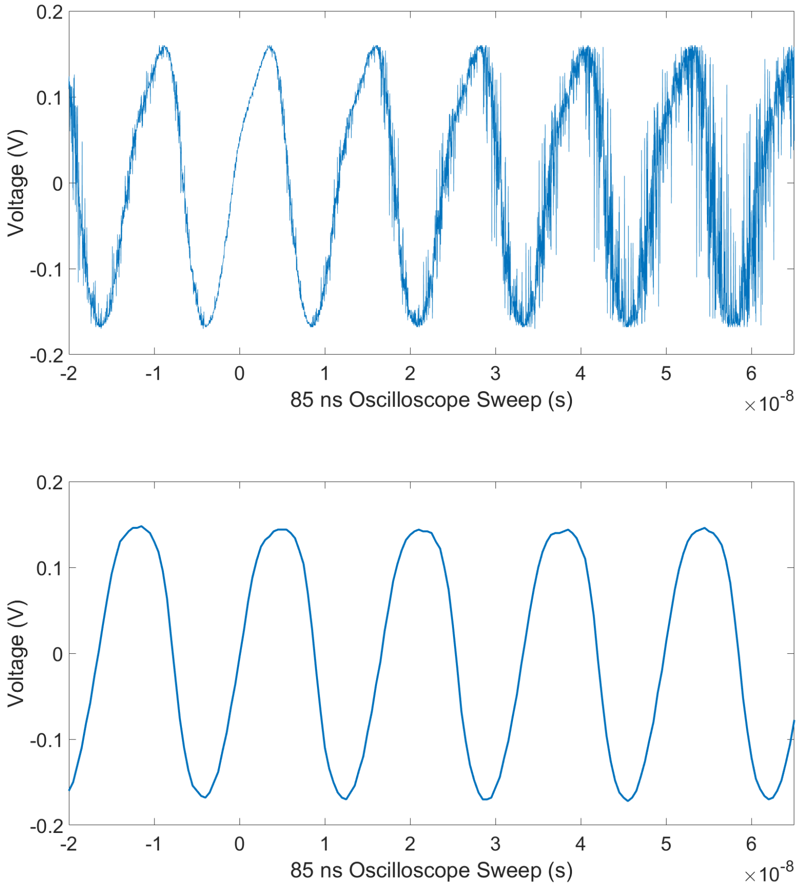

Figure 3.5: The oscilloscope trace for a phase lock attempt with a 60 MHz local oscillator signal used as the reference. The top image shows the unlocked beat signal hovering around 100 MHz taken with an equivalent time trace to show the phase drift of the signal. The bottom image shows the phase locked beat signal at 60 MHz after tuning the PZT on the slave laser.

pair, the LO is from a stable signal generator while we feed the other laser pair with a far less stable sinusoidal signal from a voltage-controlled oscillator (VCO). With two separate sources, we introduce a phase difference between the ARP pulses, and the VCO is far less phase stable than a standard signal generator and will drift on the order of several kHz per second. This changing phase provides the phase incoherence we require for this comparison.

Observing the beat signal on a spectrum analyzer shows several other coherent RF signals present in the lab vicinity. The most prominent of these being the 10 MHz clock from various electronic measurement instruments and the 51 MHz signal for driving the helium discharge in the SAS cell. The 10 MHz signal will appear no matter what as it is essential for the operation of our high frequency RF equipment. The 51 MHz signal could be eliminated by placing a faraday cage around the discharge cell. More details of the phase locking electronics can be found in Chapter 5.

These phase locked slave laser beams are then converted into pulses with the fiber optic modulators mentioned earlier. Since this modulation section is external to the Phase Locked Loop (PLL), it should not result in any loss of coherence between each master and slave laser pair. Thus, the phase information established by the PLL for each beam should not be disrupted by the time the atoms interact with the light.

3.3 ARP Light Production

The diode lasers in ARP setup produce over 80 mW of power after the extended cavity, and can have over 50 mW of light coupled into a fiber. In the full experimental setup, two slave lasers each have their own fiber lines and components including in this order: a phase modulator (PM), booster optical amplifier (BOA), amplitude modulator (AM), and 4 Watt fiber amplifier (4WFA). Figure 3.6 shows the entire experimental setup for the velocity dependence of the ARP Force experiment.

The pulses in this setup are timed such that the phase between pulses within a pair ϕ_{rel} is π that will sweep the $\vec{R}$ to the north pole of the Bloch sphere. The successive pulse sequence will bring $\vec{R}$ back to the south pole. With a retroreflected beam from one laser, phase does not become an issue as long as the initial delay on the Data Timing Generator is programmed correctly.

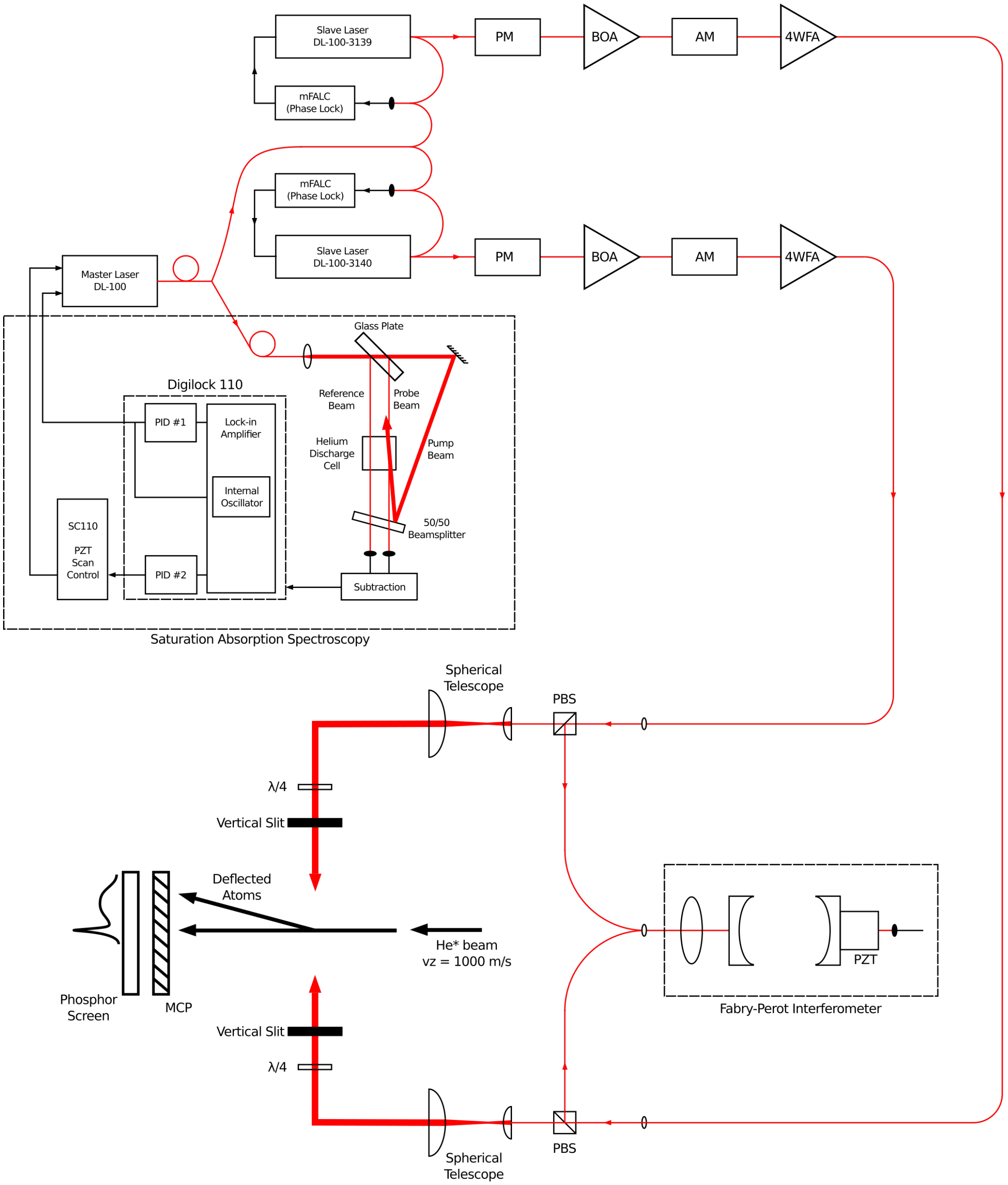

Figure 3.6: Diagram of the full experimental setup. The components in this setup are labeled as follows: Phase Modulator (PM); Booster Optical Amplifier (BOA); Amplitude Modulator (AM); 4-Watt Fiber Amplifier (4WFA); Micro-channel Plae (MCP); Mixed Fast Analog Linewidth Controller (mFALC).

The duty cycle for the pulse generation process also plays a role in the overall strength of the ARP force. For the experiment, a duty cycle of 17% is chosen, which leads to a dead time of $2\pi \ / \ \omega_m$ as it provides the largest force over time. As the duty cycle is decreased, the time between absorption and stimulated emission will change from $2\pi \ / \ \omega_m$ to $4\pi \ / \ \omega_m$. Based on a momentum change of $2\hbar\vec{K}$ and a sweep rate of $\omega_m = 100\gamma$, the resulting ARP force can be expressed as $\vec{F}_{ARP} \ / \ 2 = \hbar\vec{k}\omega_m \ / \ 2\pi$.

However, the ARP force is strong only for the first several pulses and will exponentially degrade in strength with each successive pulse pair. Spontaneous emission becomes increasingly likely to occur before the second pulse in the sequence arrives. The second pulse that would normally drive the atom down to the ground state would do the exact opposite, and can ultimately lead to an ARP force in the opposite direction. As a result, the force on average can vanish [6]. Experimentally, some atoms will be left in the excited state and may only have spontaneous emission as a means of decaying back down to the ground state. The largest initial ARP force can be observed with no dead time present, but the force is reduced to zero as the possibility of force reversal increases after several dozens of pulse pairs. A dead time of $2\pi/\omega_m$ is chosen for the experiment, which leads to a longer period between absorption and stimulated emission (T $= 2\pi/\omega_m \rightarrow 4\pi/\omega_m$. The momentum change remains the same ($2\hbar k$), and the overall force is reduced to $\vec{F}_{ARP}/2 = \hbar\vec{k}\omega_m/2\pi$. Given a sweep rate of $\omega_m = 100\gamma$, the largest possible ARP force is $\sim 32\vec{F}_{rad}$. The added dead time helps to remedy this issue it provides a means for restoring the original direction of the ARP force by allowing atoms enough time to return to the ground state before the second pulse sequence begins [18] [19].

3.3.1 Phase Modulator

The first optical component the light out of either slave laser will be a Photline model NIR-MPX-LNO3 electro-optic modulator (EOM) designed as an integrated waveguide with fiber pigtails at each end. This modulator is fabricated in a manner such that the electrodes can be placed in close proximity to each other, which leads to less voltage required to drive a strong modulation. The bulk Thorlabs EOM used for the DFB locking setup require hundreds of volts to drive a π phase shift. This EOM is the phase modulator responsible for providing the cosinusoudal frequency chirp at ω_m from Ref. [7]. Each phase modulator is driven by a HP 8657D RF signal generator whose signal is amplified by a MiniCircuits ZHL-1-2W-S+ RF 29 dB amplifier. Details regarding these modulators can be found in Ref. [19] [6] [7].

Following the phase modulator, the light will pass through a Thorlabs Booster Optical Amplifier model BOA1137P (BOA), which plays a crucial role in provide enough amplification to bring the optical power over the -3 dBm operating threshold of the Keopsys fiber amplifiers. The phase and amplitude modulators have a combined insertion loss of 8 dB on each line while the fiber couplers. Every component in the fiber line is permanently spliced, which is estimated to produce a combined loss of ∼2 dB. The combination of components in our fiber lines led to a total insertion loss of at least 10 dB (ultimately, at least a factor of 10 loss in power), which make the BOAs necessary for this setup.

3.3.2 Booster Optical Amplifier

These BOAs are semiconductor (GaAs) based optical amplifiers fabricated to conform to a standard 14-pin butterfly package that are mounted to a Thorlabs LM14S2 universal butterfly mount. These amplifiers are designed in a similar manner as semiconductor laser diodes, but instead of possessing a cavity designed to facilitate multiple reflections, they are designed for a single pass through the cavity. This is done by coating the facets of the semiconductor with an anti-reflection coating as opposed to a highly reflective coating that would be used in conjunction with another reflector in an extended cavity setup.

Polarization also plays an important role for the BOAs as they only amplify light linearly polarized along the slow axis of the polarization maintaining (PM980) fiber pigtailed to each end of the amplifier. Thus, splicing the fibers plays a significant role for maintaining enough power and the correct polarization through this component as well as the modulators. Mating sleeves that join two connectorized fibers together do not entirely guarantee that polarization will be maintained, and can lead to power loss as well. The correct polarization is maintained through the phase modulator, BOA, and amplitude modulator by splicing the PM fibers together.

The two BOAs respectively operate at a center wavelength of 1050 nm and 1053 nm. One BOA is driven by an ILX Lightwave model LDC-3722 Laser Diode Driver that is a dual current and temperature controller set to respectively operate at 301.2 mA and 9.99 kΩ (∼25.0^{o}C). The other is driven by a Newport model 505 Laser Diode Driver and Newport model 325 Temperature Controller set to respectively operate at 299.8 mA and 9.99 kΩ (∼25.0^{o}C). These settings raise the output wavelength to 1083 nm while also optimize the gain at this wavelength. Amplitude Modulator

After exiting the BOA, the light will then pass through a Photline model NIR-MX-LNO3 amplitude modulator. The integrated waveguide design is loosely similar to that of the phase modulator, but the key distinction here is the Mach-Zehnder interferometer waveguide that will split the light down parallel lines and recombine into a single waveguide. Two separate electrodes are placed in the center of the interferometer that respectively handle DC and RF signals. The grounding electrodes are placed on the outside on both sides of the interferometer. The DC signal delivered to the modulator can be adjusted so the interferometer produces only destructive interference as long as there are no RF signals. The RF signal will provide the voltage that will bring the modulator to the condition for interfering constructively as the pulse enters, and return to interfering destructively as the pulse diminishes.

Each amplitude modulator is driven by both a DC voltage from a Power Design model 2005 precision power supply, and RF pulses produced by a Tektronix model DTG5274 Data Timing Generator running at 320 MHz with a 17% duty cycle and a repetition rate of 80 MHz. Weve measured these pulses to have a width of ∼3.125 ns. The Data Timing Generator (DTG) also plays a key role in providing the master frequency clock for not just itself, but the HP8657A signal generators for the phase modulators as well. This synchronization is necessary for properly aligning the frequency chirp and RF pulse in time to produce the correct chirped pulse for ARP.

3.3.3 Fiber Amplifier

Finally, the Keopsys model KPS-BT2-YFA 4 Watt Fiber Amplifiers provide the amplification necessary for reaching the optical power for ARP. These amplifiers are based on Yb-doped fibers that absorb 980 nm light well and provide additional gain through stimulated emission proportional to the diode pump power in the fiber amplifier boxes. As long as the -3 dBm (0.5 mW) average power threshold from the 1083 nm seed light is met, the light can be amplified to the experimental maximum of ∼1.1W. The new laser system allows us to do this much more easily while the old DBR setup provided an added challenge due to its limited power output despite taking advantage of fiber optic components designed for telecommunications. However, once the -3 dBm threshold is reached, the power output of the fiber amplifiers can be adjusted by changing the current through their respective diodes.

3.3.4 Beam Transport and Signal Monitoring

The light out of each amplifier is shaped and transported to the interaction section of the vacuum chamber. Each line has a polarizing beam splitter (PBS) cube right after exiting the fiber coupler out of the fiber amplifier. The part of the beam not being sent to the experiment from both lines is mixed in a fiber combiner and sent for live monitoring with a homemade Fabry-Perot interferometer. The Fabry-Perot used here has a cavity length of 25 mm, and mirrors with diameters of 12.7 mm, have 25 mm focal lengths, and are 9.5 mm thick. The free spectral range of the cavity is ∼3 GHz, and has a resolution of ∼30 MHz. Figure 3.7 shows the schematic diagram for the interferometer. In order to observe the signal from just a single line, the output of the PBS on either side simply needs to be blocked. A Thorlabs model DET08FC fast photodiode capable of detecting signals up to 5 GHz provides the intensity measurements for the pulses, and the Fabry-Perot measures the frequency spectrum.

These pulses can also be controlled by the generator to have a specific delay, which plays a key role in finding the maximum observable force without any detuning as this becomes the calibration for the rest of the experiment in this configuration. This becomes a valuable tool for properly adjusting the phase and amplitude modulator parameters to make sure that two key requirements for ARP are met: residual CW light is extinguished, and the relative phase between the phase and amplitude modulator signals are 0 or π. The DC offset in the amplitude modulator helps maintain a destructive interference condition as long as it is not receiving any RF pulses. However, it can be possible for the original CD light to leak through if not properly set, which can lead to strong amplitude fluctuations in the modulated pulse. An improperly adjusted phase between the two modulators will leads to frequency sweeps that cause asymmetries about the carrier signal in the Fabry-Perot spectrum. When the

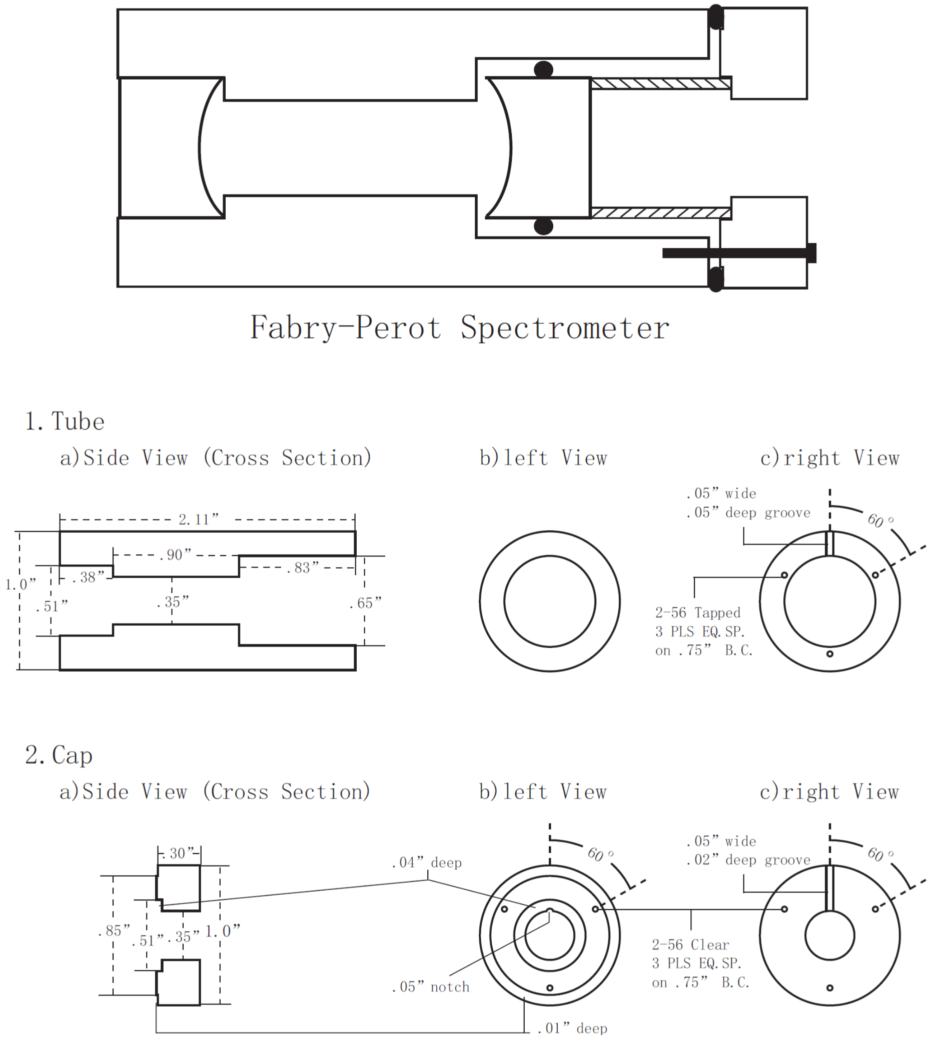

Figure 3.7: Drawing for Fabry-Perot Interferometer taken from Ref [6].

phase is adjusted to $\phi = 0$, then a fully upward frequency sweep is performed, and $\phi = \pi$ leads to a fully downward sweep. In either case, the signal is swept symmetrically about the carrier, and a comparison between aligned and misaligned signals can be seen in Figure 3.9. A more detailed analysis of this process can be seen in Ref. [6].

The light being sent to the vacuum system for the experiment is further shaped in order to fit the shape of the atomic beam from the Helium source. Light from the PBS going to

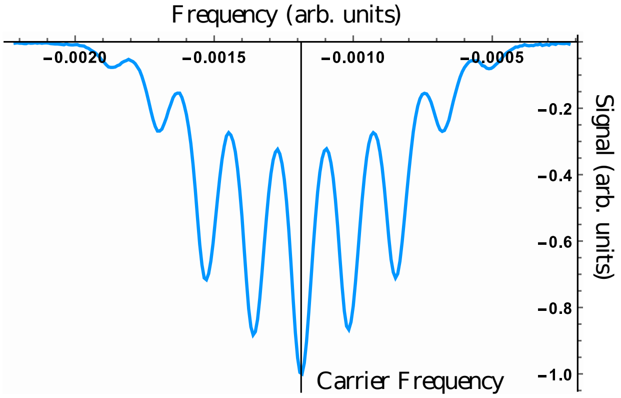

Figure 3.8: The Fabry-Perot spectrum for a train of pulses produced by the amplitude modulators. Each peak is separated by the repetition rate of 80 MHz with a full signal bandwidth of 320 MHz.

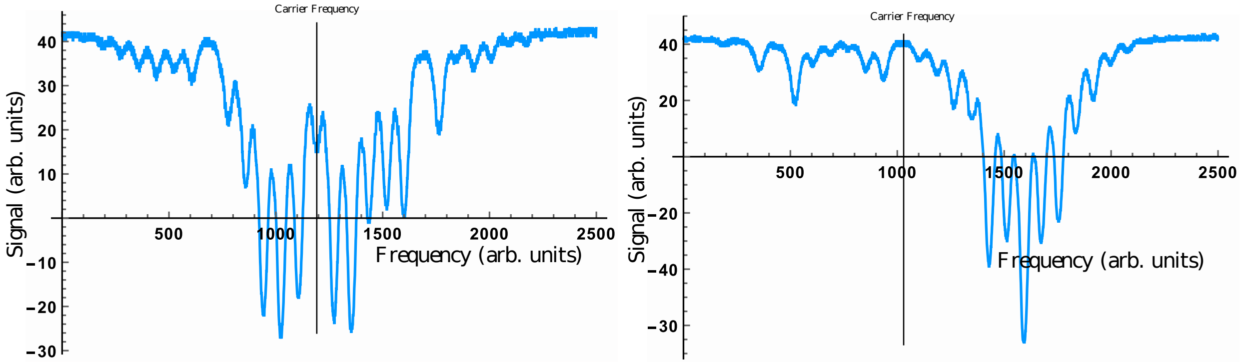

(a) Properly Aligned Chirped Pulses

(b) Misaligned Chirped Pulses

Figure 3.9: Part (a) The Fabry-Perot spectrum for an ARP pulse with a chirp properly aligned to the amplitude modulation. The goal here is to find a point of rough symmetry by adjusting the phases of the signals driving the two modulators. Part (b) shows the case of a misaligned pulse where we see a lack of symmetry with respect to the carrier signal.

the experiment is linearly polarized, and a spherical telescope first expands the beam, and is followed by a cylindrical telescope that will shrink the beam waist down to 6 mm. The then light passes through a $\lambda/4$ waveplate to change the polarization from linear to circular in order to strongly drive the $2^3S_1 \rightarrow 2^3P_2$ transition. Lastly, the light is sent through a vertical slit that will limit the interaction time with the atoms as they travel on average at

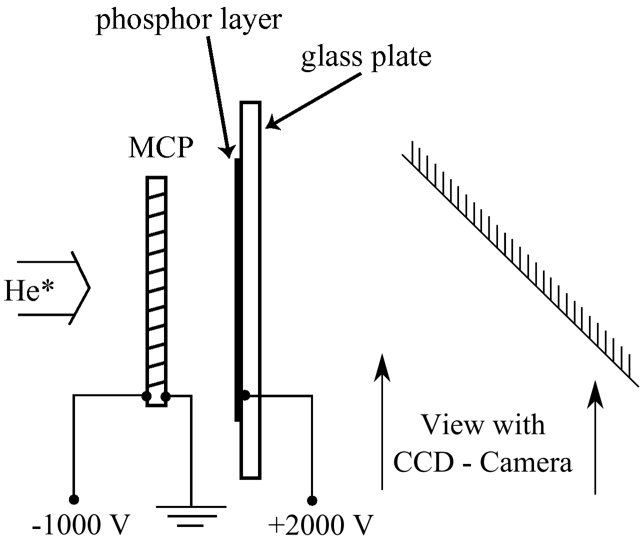

Figure 3.10: A diagram of the Micro-channel Plate/Phosphor Screen detector inside of our vacuum system. He* atoms incident on the MCP will strike the MCP driven by a -1000 V bias and cause electrons to eject. This process is repeated by the electrons until exiting the MCP and striking the phosphor screen, which will fluoresce and appear on the CCD camera. Modified from Ref. [6] [7]

1000 m/s. By limiting the slit width to 3 mm, the interaction time between the light and atoms is limited to 3μs ($\sim$30 lifetimes).

3.3.5 Detection

Detecting He* atoms involves a combination of a multi-channel plate/micro-channel plate (MCP) and phosphor screen that allows us to detect the cross section of an atomic distribution as atoms are deflected by the ARP force. A diagram of this setup can be seen in Figure 3.10, and more on the rest of the vacuum system is well described in Ref [7].

As He* atoms travel down the vacuum system, they will encounter a thin disk of lead coated glass consisting of many 10 μm wide tubes (channels) oriented in a 12 μm radius hexagonal pattern perpendicular to the disk surface. When a He* atom enters one of the channels and strikes the channel wall, the 19.8 eV of internal energy carried by the atom can cause multiple electrons to cascade. A negative bias of -1000 V is placed on the MCP while being grounded on the back surface, which allows electrons to multiplicate and accelerate down the channel. This cycle repeats as the new electrons continue to cascade and produce more electrons until they exit the MCP.

These electrons then impact a phosphor coated glass plate placed directly behind the MCP that will cause a fluorescence that is proportional to the electron flux based on the number of He* atoms incident on the screen. A +2000 V bias is placed on the phosphor screen that will accelerate the electrons exiting the MCP towards the screen. A mirror placed at 45^o behind the phosphor screen, and the fluorescence is imaged by a Thorlabs model DCU224M CCD camera from outside the vacuum system. This detection method works well for metastable helium, but the phosphor screen also detects UV light emitted by the source. The vacuum system is constructed in such a manner that causes the UV light from the source to travel the same path as the helium atoms, which makes them indistinguishable when viewed with the CCD camera.

The CCD camera operates at a 1 frame per second as a result of having to increase the exposure time enough just to be able to observe a bright enough phosphor screen. As the parameters for the amplitude and phase modulators are changed, snapshots are taken as opposed to a video that requires a much higher frame rate (e.g. considerably shorter exposure time). Each image is analyzed using a combination of ImageJ, an image program developed by the National Institute of Health, and Mathematica.

Chapter 4

DFB Laser System

The previous experimental setup centered on a pair of Distributed Bragg Reflector (DBR) diode lasers as the light sources for eventual ARP pulse production. These diodes are fabricated through an epitaxial growth process involving etching and chemical vapor deposition that allows the many lasers of the eventual monolithic design to be produced on a single wafer. From an initial GaAs substrate, a single-mode index guided ridge waveguide is constructed to act as the resonant cavity of the electrically pumped gain medium. The output is of this cavity is limited to one side of the cavity with a highly reflective mirror on one end and an anti-reflection (AR) coated output facet [20].

Our initial phase locking test was conducted by locking the new DL-100 slave lasers to each other using the mixed fast analog linewidth controllers (mFALC, phase locking electronics) built by Toptica Photonics. These lasers were quickly able to provide a beat signal between the two beams and phase lock to various local oscillator reference frequencies. The frequency domain picture seen on our RF spectrum analyze showed us a linewidth of < 100 Hz, given a bandwidth resolution of 10 Hz. This became the benchmark for us in terms of what a successful phase lock should be, and it led us to the naive conclusion that such a clean signal could be achieved routinely with any two lasers provided the phase locking electronics were working properly. More details on these lasers and phase locking results are in Chapter 5.

Unfortunately, when the DBR laser was tried with phase locking with one of the DL-100 lasers, we immediately observed a beat signal possibly too noisy to phase lock. It appeared that the DBR laser's light that could be beat against either DL-100 and adjusted to show a beat frequency comparable to the local oscillator frequency, but severe broadening made the center of the signal of it difficult to discern. It was necessary to make sure this laser was frequency stabilized as well, but that only exacerbated the problem. The correction signal from the feedback loop further impeded the phase lock because the correction signals added additional phase noise to the beat signal. Ultimately, a phase lock could not be achieved between the DBR master laser and either slave. Therefore, we proceeded to replace the DBR diode that had already provided enough service in many previous experiments suspecting that the age of the diode caused it to degrade over time.

4.1 DFB Diode Design

In terms of general design, the DFB and DBR diodes have similar structures with regards to the construction of a resonant cavity waveguide sandwiched between semiconductor cladding layers. However, differences arise when considering the structure of the surface grating as well as its placement within the entire diode. In the initial growth process of the monolithic structure for a DFB laser, a low contrast, weakly reflecting grating surface is etched into the entire length of the gain medium. This is then followed by a regrowth process in order to "bury" the grating under a low index cladding.

Single frequency operation can be achieved in a similar manner as with the DBR setup, but with a grating spanning the entire length of the gain medium in this case. However, the new symmetry of this setup poses a different problem from the DBR case as the wavelength satisfying the Raman-Nath diffraction condition results in opposing reflections interfering destructively [21]. As a result, the laser intrinsically operates at two modes around the wavelength that satisfies the diffraction condition. Operating at a single mode with this design can be achieved by breaking this symmetry, which can be done in practice by AR coating one of the facets of the diode in order to remove opposing reflections. As a result, there is no highly reflective mirror in place on either facet, unlike a DBR diode.

During the growth process, a surface grating is etched into the semiconductor cladding surrounding the gain region. A high contrast, highly reflective grating surface is etched in with upwards of 2000 teeth over the 500 μm length of the mirror. As light is fed back into the diode, the grating provides a means of limiting the possible output modes by satisfying the Bragg condition [22]. Without the proper optical feedback, beam distortions in the gain medium permit a multimode operation. This topic will be revisited when discussing the extended cavity schemes for these lasers.

4.1.1 Optical Feedback Domains

Studies have shown that the effects of the ratio of feedback to emitted power ratio in a DFB diode can be broken down into five regimes of diode operation as seen in Figure 4.1 [23]. Regime 1 has the lowest level of feedback to the diode that can be controlled with the length of the cavity (distance to the reflector). The boundary between regimes 1 and 2 is marked by this relationship between power fed back and the length of the cavity, but the phase of the light being fed back also plays a role as a result of adjustments in cavity length. In regime 2, the DFB laser can undergo mode hopping as a result of the modes available in the extended cavity. Regime 3 exists in a narrow band of feedback power, which is thought to be appropriate to single out an operational mode. The long cavity schemes that will be mentioned were attempts to find these regions of stability.

In regime 4, the internal cavity modes of the DFB would destabilize and undergo "coherent collapse" as the linewidth of the output expands to the order of GHz when the laser undergoes a multimode operation. This is apparently independent of the cavity length and also insensitive to phase. Regime 5 occurs when feeding back more light, which was established with a short extended cavity as already shown. A single mode here seems to dominate as a result of the reduction in spontaneous emission events because the feedback power was increased beyond a critical threshold. Although we can only estimate the amount of power fed back to our laser diode based on the power of the leakage light, we expect that the laser operates in regime 5 during stable operation with $\sim 9\%$ of the original light being fed back.

4.1.2 DFB Extended Cavity Designs

The cavity of the master laser, shown in Figure 4.2, consists of a several components: the diode itself, a 70/30 beamsplitter, and a high reflectivity mirror attached to a piezoelectric transducer (PZT). The laser provides the initial light in the system and the beamsplitter transmits 70% of the light. The remaining 30% of the light is reflected towards the PZT mirror and retroreflected back to the beamsplitter. The 70/30 splitter now sends 21% of the initial light straight through while 9% is reflected back into the DFB diode. This feedback causes the laser to operate on a single, stable mode with a reported linewidth of 2 MHz by the laser manufacturer, Eagleyard.

The initial 70% transmitted through the beamsplitter becomes the main beam for the

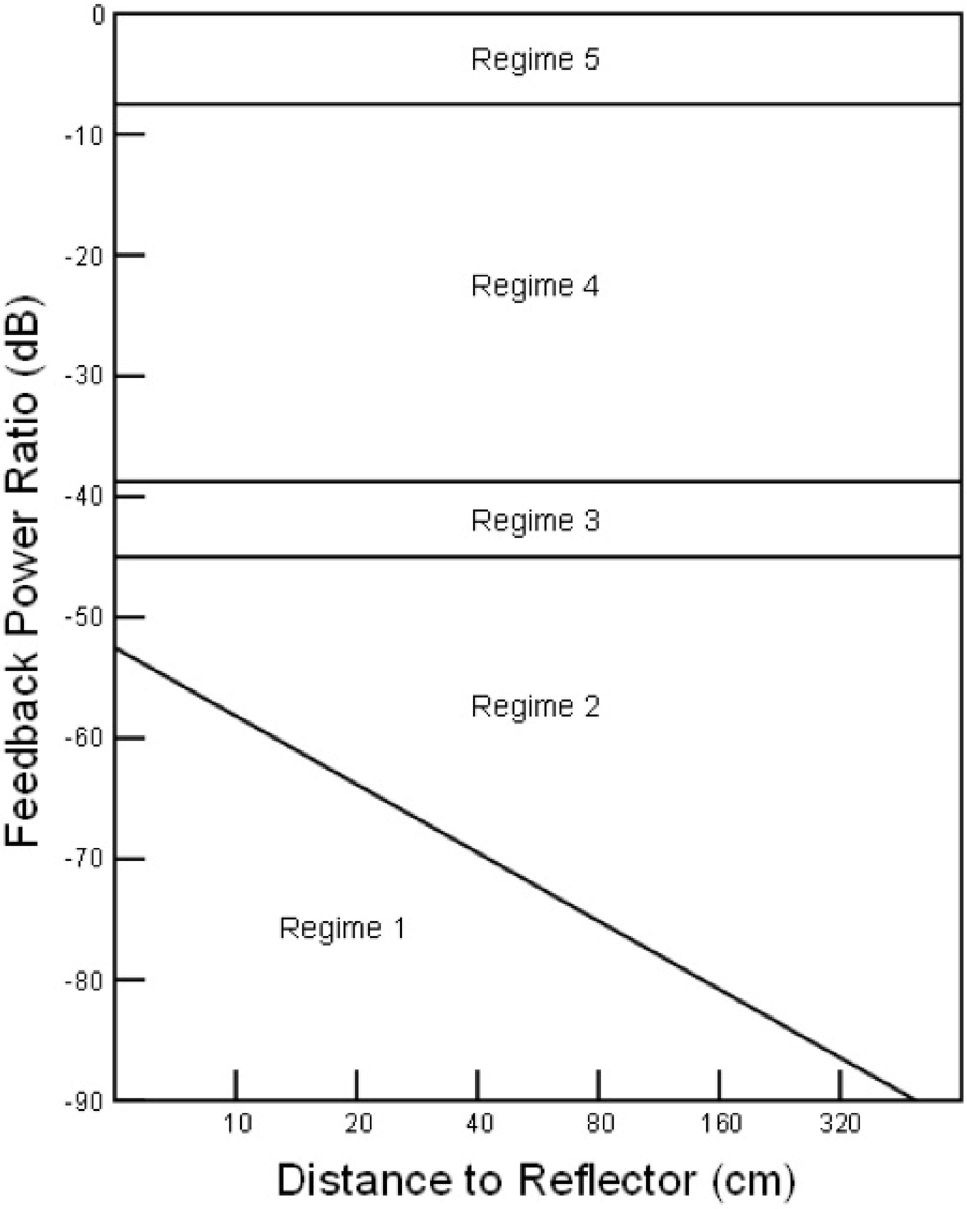

Figure 4.1: The regimes of operation for a semiconductor laser based on the ratio of power fed back into the diode against the length of the feedback cavity. Regimes 1, 3 and 5 represent regions of stable, single mode laser operation. Regimes 2 and 4 represent regions of instability in the diode that can lead to multimode operation as the linewidth expands to the order of GHz.

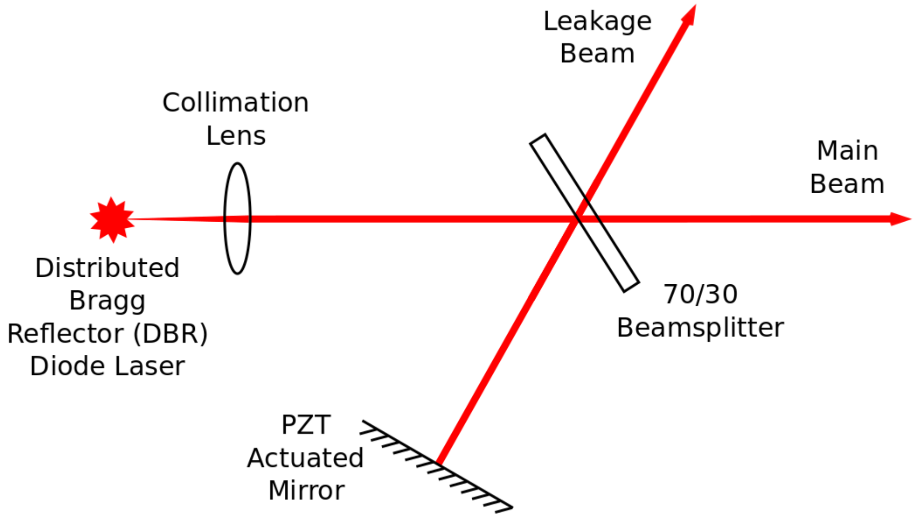

Figure 4.2: A basic design for an extended cavity for our DFB master laser system. The diode outputs light is collimated by a lens mounted by the output facet. This light is split by a 70/30 beamsplitter that transmits 70% of the inital light and reflects the remaining 30%. The 70% light is used in the experiment while the 30% light is reflected back by the PZT actuated mirror. This reflected light passes through the beamsplitter and results in 21% of the initial light trasmitting into the "leakage" beam and 9% reflecting back into the diode.

experiment. The 21% now transmitted through the beamsplitter provides a leakage beam that is used for the saturation absorption spectroscopy as a part of the frequency locking mechanism for the master laser as shown in Figure 4.2. Stabilizing the output linewidth of DFB, DBR and Fabry-Perot diode lasers largely depend on the ratio of power between emission and feedback, extended cavity length and returning phase.

Unfortunately, the DFB diode that replaced the old DBR diode produced light at 1082.3 nm as opposed to the 1083.0 nm we expected when operating at 20^{o}C. In order for the new DFB to produce 1083 nm light, it needed to be heated to 40^{o}C. Naturally, this was a major cause for concern since operating at this high temperature would undoubtedly cause permanent damage to the diode over time, and severely shorten its lifespan. As a result, the effect of this temperature seemed to manifest itself in the form of a significant frequency

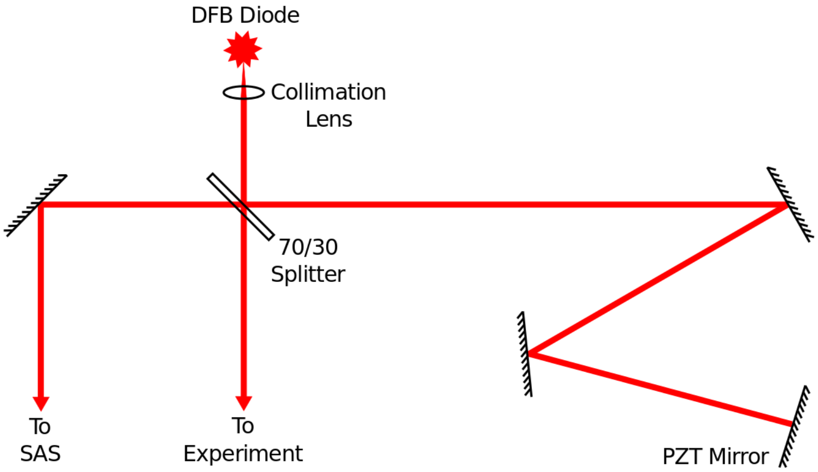

Figure 4.3: The diagram showing the extended cavity design involving multiple reflection in order to increase cavity length. This design was limited by the space available on the isolated breadboard used solely for the DFB laser, which meant the achievable length possible for this setup had a finite limit.

drift of the DFB's output as shown by the RF spectrum analyzer. In order to counteract this drift based on the optical feedback studies, the extended cavity required further study.

Multiple Mirror Cavity

The length of any possible optical feedback path for our laser was limited by the space available in the thermally insulated optical breadboard. In order to overcome this, we used multiple silvered mirrors (see Figure 4.3). The difficulty in the scheme was twofold: the first involved the alignment of multiple mirrors so the PZT mirror handles the feedback properly for the frequency lock; and the second involved the sensetivity of the mirrors to external vibrations. In addition, some minor power losses were expected with each successive reflection.

Ultimately, the length of this cavity did not affect the overall performance of the laser to the degree that was expected. This observation was tested on the RF spectrum analyzer that would provide a direct measurement of overall cavity mode spacing as well as the linewidth of the laser output. Unfortunately, there was no discernible reduction of the overall linewidth compared with the basic extended cavity design. If anything, the cavity mode spacing was reduced slightly by at most a few MHz from approximately 50 MHz.

Fiber Feedback Cavity

Due to the physical and practical limits of placing additional mirrors, a new scheme was considered that used an extended cavity having a polarization-maintaining (PM) fiber as part of it. The diagram for this setup can be seen in Figure 4.4. Light was sent into the 1 m long fiber through a fiber input coupler using a pair of silvered mirrors, exits through an output coupler, and then passes through a half-wave plate (HWP) and a variable attenuator before reaching the PZT mirror. The PM fiber showed a coupling efficiency on the order of $\sim 45\%$ (16.0 mW entering the fiber and 7.5 mW exiting). The amount of power fed back to the DFB was primarily adjusted by the variable attenuator.

Measuring the stability of a single mode and the cavity mode spacing followed the same procedure as before, namely by beating light from a stable source (DL-100) and observing the output on the spectrum analyzer. When either the feedback path into the DFB was misaligned or the available power was too low, the laser would undergo a multimode operation. This showed that the cavity mode spacing of this setup was narrowed to ~ 30 MHz compared to the ~ 50 MHz mode spacing seen earlier. In addition, neither of the schemes mentioned here resolved the issue of the seemingly intrinsic drift of the DFB output.

Ultimately, the system reverted back to the basic extended cavity design and a relatively stable region could be found where mode hopping was reduced to a minimum. Nonetheless, mode hopping still occurred as the frequency drift persisted, which naturally would affect any attempts at frequency locking the DFB let alone phase locking to an external system.

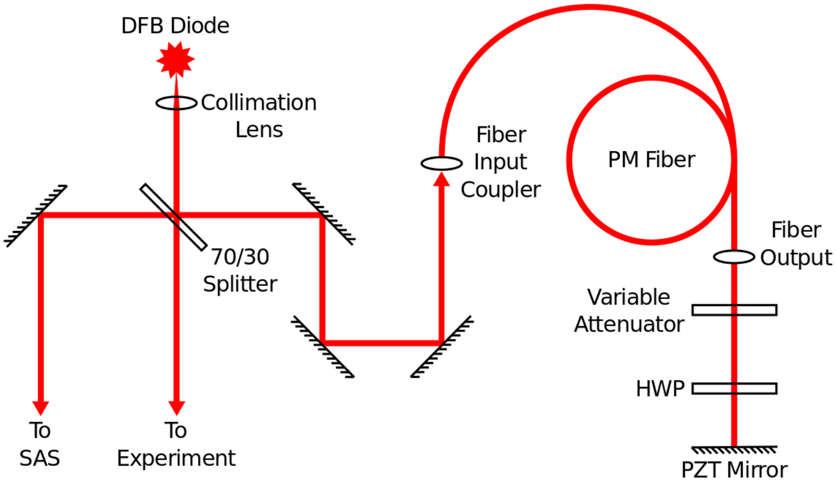

Figure 4.4: The diagram for the extended cavity design involving optical feedback through a fiber modified from [24]. This was a significantly more compact design compared to the multiple mirror setup, which was limited only by the length of the fiber used. In this case, a 1 m long PM fiber was installed in order to have control over the polarization returning into the laser.

4.2 Frequency Stabilization

4.2.1 FM Current Dither

The previous setup of this laser system used a 10 kHz frequency modulation of the current to the diode. A modulation was thus applied to the absorption signal and this was detected by a PAR model 126 Lock-in Amplifier to provide the error signal. This error signal was sent to our SRS PID regulator that handled the production of the correction signals as the laser drifts either above or below resonance at the "top-of-fringe" absorption peak. The laser was stabilized with the PZT mirror in the extended cavity setup as it received these correction signals from the PID regulator.

The new setup for the phase locking system involved the old DFB setup and two new slave lasers and their linewidth controller electronics, built by Toptica Photonics. The initial phase lock was tested with the two new slave lasers free running and beat together to produce and lock to a 20 MHz signal. In short, this test proved successful after the phase locking PID settings and impedance issues were better understood. Our rather naive conclusion was that this system would be universal to all laser systems, namely, that we would be able to phase lock our DFB laser to either of our slave lasers.

We would soon discover a significantly noisier beat signal with the DFB free running and either slave laser. Unfortunately, this signal could be phase locked only intermittently and not long enough for the purposes of the experiment. Some of this noise could be reduced by using one of the current controllers from the new slave lasers, which provided a modest improvement in terms of noise visible on the frequency spectrum. However, when coupled together with the intrinsic drift already observed, we began to lose confidence in this setup.

Unfortunately, further problems arose when we tried to simultaneously frequency stabilizing the DFB master laser and phase locking a slave laser together. The ultimate result was the sheer inability to achieve a phase lock with this setup using the SRS PID regulator. While the DFB master laser could initially be frequency locked, the laser soon jumps lock and settles at a new frequency well off of resonance. At certain times, a phase lock could be achieved but only in this off resonant condition. The combination of adding a modulation to an already apparently unstable laser along with periodic spikes in voltage sent by the PID regulator led us to rethink our frequency stabilization scheme.

4.2.2 External Modulation

The next attempt in establishing a frequency lock in our master laser involved removing modulation placed directly onto our diode current. This required an external modulation of a portion of the master laser's output in order to implement SAS while allowing the remaining light to interact with the slave lasers as a part of the phase locking process. Phase modulation by means of a broadband electro-optic modulator (EOM) manufactured by ThorLabs acted as an immediate solution.

The phase delay provided by the EOM as light passes through it is described below with a strong dependence, where $V(t)$ is the voltage applied to the $\mathrm{LiNO_3}$ crystal and $M(t)$ is the frequency dependence of the phase delay as a result of the optical phase mismatches and RF losses:

$$\phi(t) = \kappa M(\omega_m)V(t) \tag{4.1a}$$

$$\kappa = \frac{\pi}{\lambda G} n_e^3 r_{33} \eta L \tag{4.1b}$$

where κ depends on the crystal properties. Based on the sinusoidal radio frequency (RF) signal applied to the crystal, the time-dependent electric field of the resulting light emerging from the crystal is given by:

$$E(t) = E_0 \cos[\omega_\ell t - \beta \sin(\omega_m t)] \tag{4.2a}$$

$$\beta = \frac{\pi V_0}{V_\pi(\omega_m)} \tag{4.2b}$$

where V_0 is the applied voltage and ω_m is the modulation frequency. V_π is the "half-wave voltage" for shifting the phase of the optical field by π.

$$V_\pi(\omega_m) = \frac{\lambda G}{n_e^3 r_{33} \eta L M(\omega_m)} \tag{4.3}$$

Ultimately, the time derivative of the phase in the light field can be shown to produce a

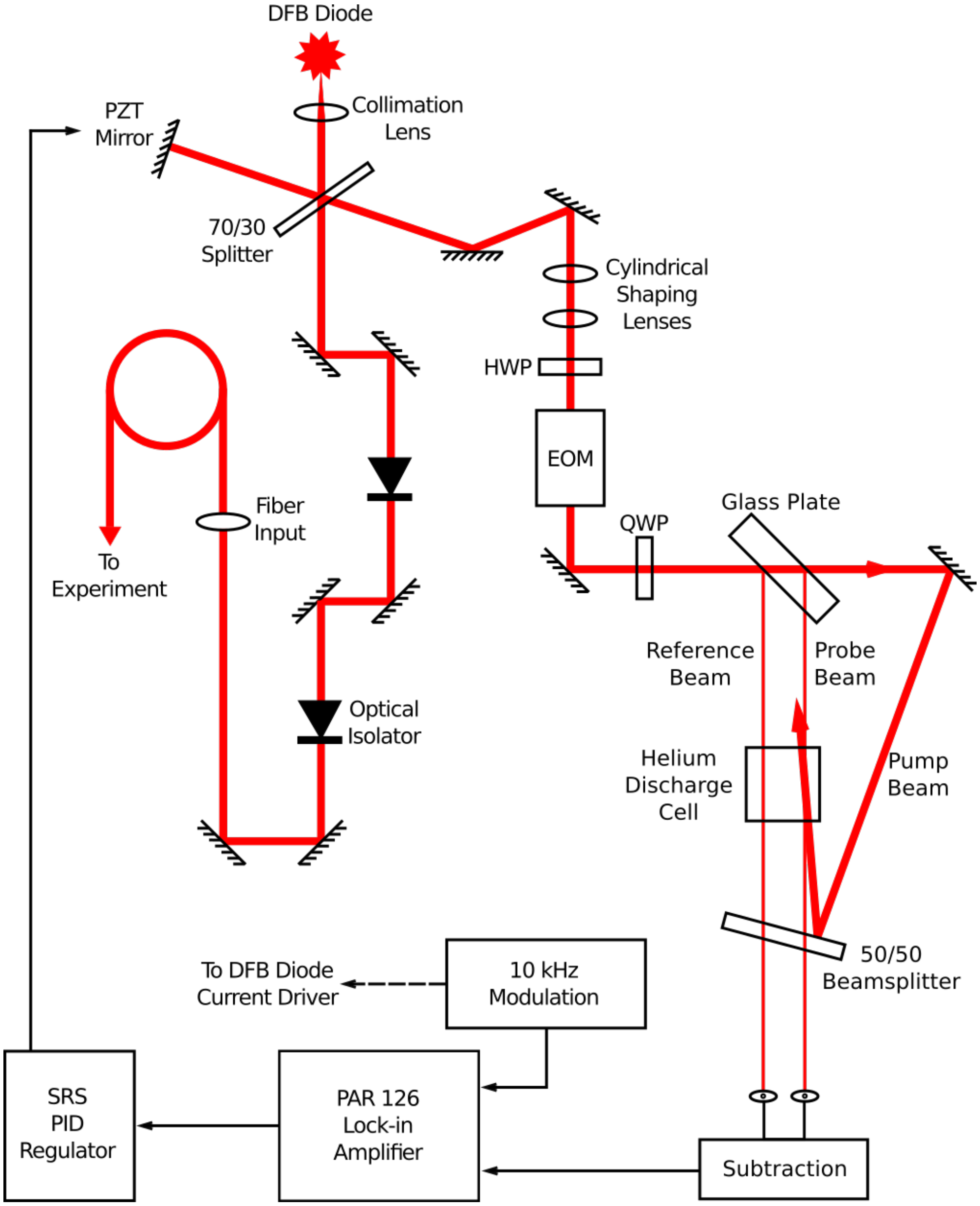

Figure 4.5: The setup for frequency stabilizing the DFB diode laser with an external modulation from an EOM. Two beams emerge from the extended cavity setup of the DFB, which provides the light for the the experiment and the SAS lock. The light going to the experiment is coupled into a fiber after passing through two opticla isolators to prevent any unnecessary optical feedback into the diode. The light for the SAS lock passes through the EOM, which adds the dither to the absorption signal obtained from the rest of the SAS setup.

frequency modulation:

$$\omega(t) = \frac{d\phi(t)}{dt} = \omega_\ell - \beta\omega_m \cos(\omega_m t) \tag{4.4}$$

The presence of ω_m in Eq. 4.4 dictates that a high modulation frequency is needed for an adequte modulation of the light beam.

The ThorLabs specifications for a non-resonant phase modulator designed for wavelengths between 900 and 1250 nm (EO-PM-NR-C2) indicate a half-wave voltage on the order of 225 V_{PP}.

Tank Circuit

In order to emulate the 10 kHz current modulation directly on the diode based on the tuning coefficient of the current driver(-300 MHz/mA) several amplification circuits were designed and tested. The first attempt at providing an RF signal with the amplitude and frequency necessary for a phase modulation, an LC resonator (tank) circuit was designed and tested. Initially, the circuit consisted of only a readily available capacitor-inductor combination that could provide a bandpass output with a Q-factor of ∼30. The goal here was to provide a signal strong enough to drive a phase modulation with the EOM while being a low enough frequency to act as a reference for the lock-in amplifier. The range of frequencies the Princeton Applied Research lock-in amplifier (PAR-126) could handle in this case was up to 240 kHz.

The voltage of a 150 kHz RF signal could be amplified fivefold, but the voltage would decay over time as a sign of instability in this resonator. In addition, the PAR-126 operated with a 600 Ω input impedance, which meant a slightly different design was needed so that and a transformer could provide impedance conversion from 50 Ω to 600 Ω. The redesigned circuit is shown in Figure 4.6. The Sprague transformer installed in the circuit provided a

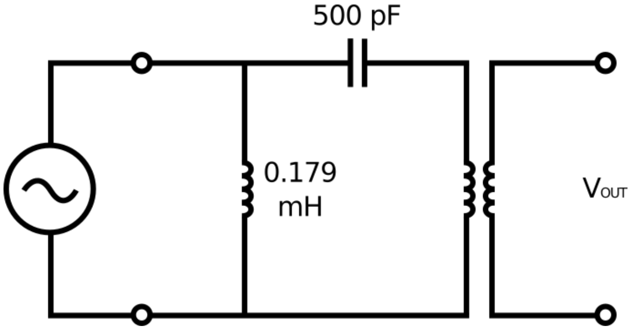

Figure 4.6: The diagram for the tank circuit used for driving our EOM with a high voltage sinusoidal signal. The bandpass output obsevred with this circuit showed a Q-factor of ~ 30 centered on 150 kHz. This circuit provided a high voltage enough voltage for our purposes, but would degrade over time and no longer lead to a sufficient phase modulation on the laser beam.

further fivefold step up, but the same problem with voltage decay persisted. Ultimately, the stability of the resonator and transformer output made this circuit impractical, and much less efficient than a commercially available high voltage operational amplifier.

PA341CC High Voltage RF Amplifier

In order to provide a more stable source of RF amplification that could meet our specifications, an Apex operational amplifier (PA341CC op-amp) circuit was designed to replace the tank circuit. The diagram for this circuit is shown in Figure 4.7.

This chip provided a slew rate of 8 V/μs with a gain bandwidth product of 10 MHz. However, these values played significant roles in limiting the practical frequency range. The slow slew rate meant the fastest frequency the circuit could amplify without signal distortion was about 50 kHz, but distortions started becoming observable on an oscilloscope trace at ~100 kHz. The 10 MHz gain bandwidth product also pointed towards the maximum possible amplification being possible for a 50 kHz signal.

A sinusoidal input frequency of 50 kHz could indeed be amplified from 10 V_{PP} to 150 V_{PP}

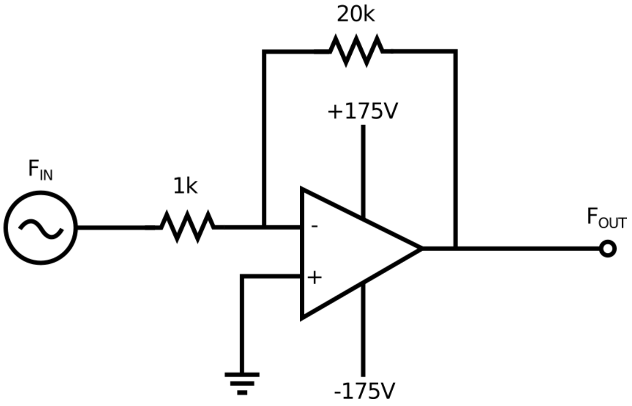

Figure 4.7: The circuit diagram for the PA341CC high voltage op-amp built for driving our EOM with a stable output of 50 kHz, $\sim$ 150 V sinusoidal signal. However, at around 100 kHz the input sinusoid would distort into a triangular shape, which is likely due to the low slew rate (8 V/μs) of the chip.

while maintaining a reference lock with the PAR-126. Furthermore, the leakage beam for the SAS lock showed the presence of a modulation when passed through the EOM. In addition, when this modulated signal was observed on the scanning Fabry-Perot interferometer, first and second order sidebands could be seen on the RF spectrum analyzer.

The problem arose when an error signal that showed a clear phase relation was unable to be processed out of the lock-in amplifier. As a result, feedback loop could not firmly establish a proper reference to the center transition frequency, and a frequency lock did not seem possible with this setup.

RF Down-mixing Scheme

The most complicated EOM setup came in the form of an RF downmixing scheme to maximize the frequency of the RF signal going into the EOM while providing a reference lock signal for the lock-in amplifier (PAR-126). The ZHL-1-2W+ model RF amplifier tested from mini circuits for this setup showed a possible amplification of 29 dB with a maximum input of 10 dBm (0.7 V_{PP}) over a frequency range of 5 to 500 MHz.

The general RF downmixing scheme involved a short list of components and processes. The first step simply involves mixing the input signal for the EOM with a similar signal that differs by some tens of kHz as shown in Figure 4.8. The resulting beat signal would include both the sum and difference of the two original signals. Thus, both a MHz scale and kHz scale signal are produced through this mixing, and the high frequency component can easily be filtered out. This should leave the kHz signal alone ready as a modulation on the SAS, which also acts as a reference for the lock-in amplifier. At the same time, the original MHz signal can be delivered to the EOM through the RF amplifier for phase modulating at a high frequency.

We found that the RF amplifier still operated at frequencies lower than the rated minimum, but on the same order of magnitude. Thus, input frequencies of 2 and 3 MHz could be tested. When mixed with a signal only 20 kHz different (i.e. 5.00 MHz mixed with 4.98 MHz), the mixed output could be seen on an oscilloscope as having both MHz and 20 kHz signals. Low-pass filters served to eliminate the high frequency signal so that the lock-in amplifier can accept it as a modulation reference for the SAS signal.

An error signal could be intermittently established, which on occasion could be sent into the SRS PID electronics box. We found that any frequency lock would not hold for more than one second and if it held for any longer, it tended towards being locked off of resonance. A top-of-fringe lock would jump away from resonance within a second due to the drift in the laser's output.

In addition, a problem arose because the entire electronics setup as we were using enough equipment to require power from multiple wall outlets. The resulting 60 Hz ground loops could be seen on the oscilloscope. Although this wasn't the reason why this frequency locking scheme would ultimately fail, it was a testament to the overall complexity and user unfriendliness of the system.

Naturally, if a frequency lock could not be maintained, then a maintaining a stable phase lock that can last for at least the duration of the experiment would be incredibly difficult. The most problematic result of these tests was the inability to establish a phase lock in conjunction with a DFB frequency lock. Only when the DFB master laser was free running could the phase lock be established, which likely meant that the laser was off resonance. In addition, the longest time recorded for this free running phase lock was just over seven minutes. Unfortunately, this setup required a significant change as a means of enhancing robustness and user friendliness.

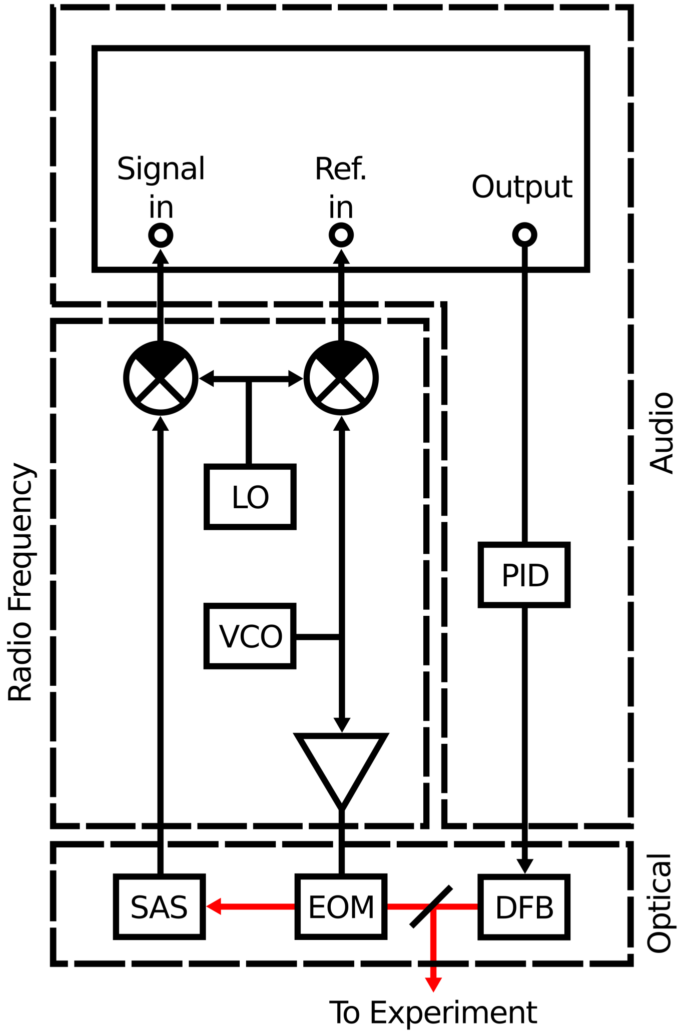

Figure 4.8: The downmixing diagram for driving our EOM with a MHz frequency as opposed to kHz as discussed in the previous attempts. A function generator provides a 3.00 MHz local oscillator signal and is mixed with a 2.98 MHz signal provided by a VCO. The high frequency component of this signal is filtered out while the low frequency component is sent to the lock-in amplifier as the reference modulation for establishing an error signal. The EOM is driven by the 2.98 MHz signal from the VCO and modulates the beam used for SAS. The SAS signal is further mixed with the 3.00 MHz signal and becomes the signal for lock-in amplifier. The error signal provided by the lock-in is sent to the PID regulator that delivers feedback signals to the PZT mirror in the DFB extended cavity for frequency stabilization.

Chapter 5

Toptica System

The DL-100 laser system designed by Toptica Photonics, Inc. center around an AR coated Fabry-Perot laser diode as opposed to either a DBR or DFB diode. In terms of construction, the most basic difference between the DBR/DFB laser diodes and a AR coated Fabry-Perot laser diode is whether or not a grating has been built into the semiconductor structure. The output facet for the Fabry-Perot diode has been AR coated in order to allow optical feedback into the diode while the other end has a highly reflective coating.

The grating is a standard part of the extended cavity of the Fabry-Perot laser, and such is how the DL-100 laser has been designed. However, the location and angle at which the emitted laser light hits the grating teeth will lead to different levels of stability and ultimate power output. The two most notable configurations differ based on the positioning of the grating and a diagram for each can be seen in Figure 5.1 (Littman-Metcalf) and Figure 5.2 (Littrow).

In the Littman-Metcalf configuration, the grating is set at a shallower angle compared to the Littrow configuration in order to cover a larger physical surface area of the grating. As a result, less individual grating teeth are covered at once by the initial light, which provides

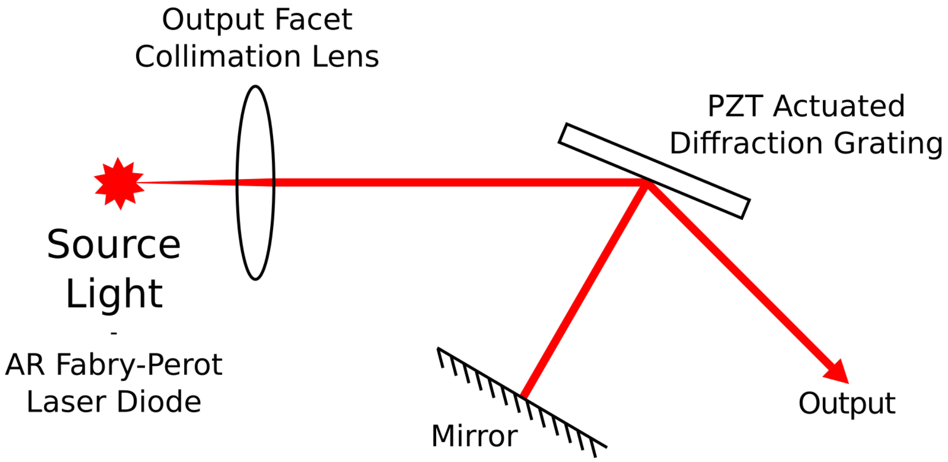

Figure 5.1: The diagram for a Littman-Metcalf setup for a grating stabilized diode laser. The shallow angle for the grating with a fixed position leads to the incoming light covering fewer grating teeth, which leads to finer wavelength control. An adjustable mirror provides control over the first order reflections back into the diode, but less control over the zeroth order light. The result is slightly less power than that of a Littrow configuration. Figure based on Ref. [25].

a finer control over wavelength selection through the optical feedback process. The grating in this setup is also fixed in place, which allows the output direction to remain constant [25].

However, this configuration also results in requiring an extra mirror with an adjustable angle to control the first order reflections for the feedback. At the same time, the zeroth order beam is lost after the reflections between the grating and mirror leading to a significant loss in output power.

In the Littrow configuration, which was elected for use in our DL-100 lasers, the initially emitted light from the laser diode will pass through a beam expanding telescope and impinge upon the grating on a piezoelectric transducer (PZT) actuated mount. Acting as both a reflective surface and a diffraction grating, the zeroth order light simply reflects off of the grating surface towards a steering mirror to continue down the output path. The first order reflection off of the grating provides optical feedback into the diode, which at the same time alters the optical path of the zeroth order beam as the grating angle is adjusted.

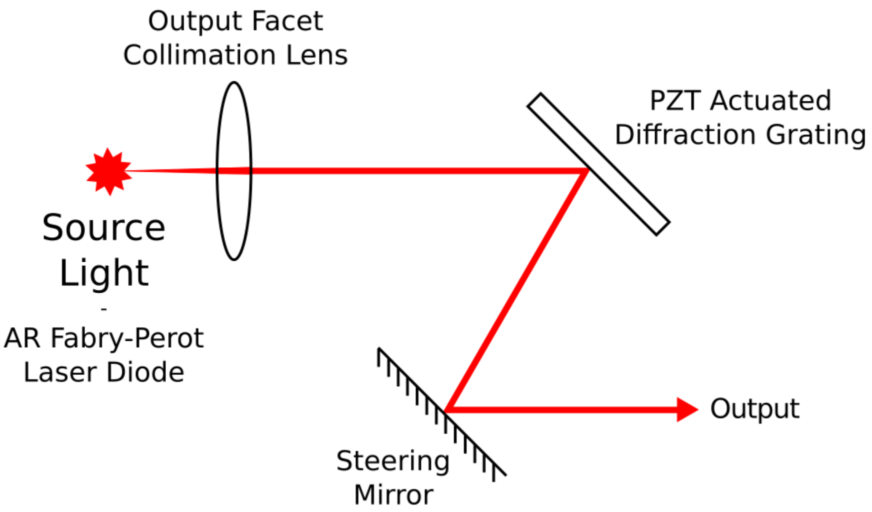

Figure 5.2: The diagram for a Littrow setup for a grating stabilized diode laser. The steeper angle for the adjustable grating leads to a less wavelength control compared to the Littman-Metcalf configuration, but leads to more power as control over the zeroth order light is maintained. Figure based on Ref. [26].

The diffraction grating mounted together onto the same brass block as the steering mirror in order to properly manage the direction of the output. Following this section is a series of beam shaping optics including: a second collimation lens, anamorphic prism pair and an optical isolator. The overall design of the DL-100 laser system can be seen below:

The collimation lens following the diffraction grating performs the same task as the lens in front of the output facet of the diode; however, at this point the beam is still more elliptical than circular in shape. The anamorphic prism pair serves to shape the intrinsically elliptical output from the output of the diode into a circular shape compatible for efficient coupling into a fiber.

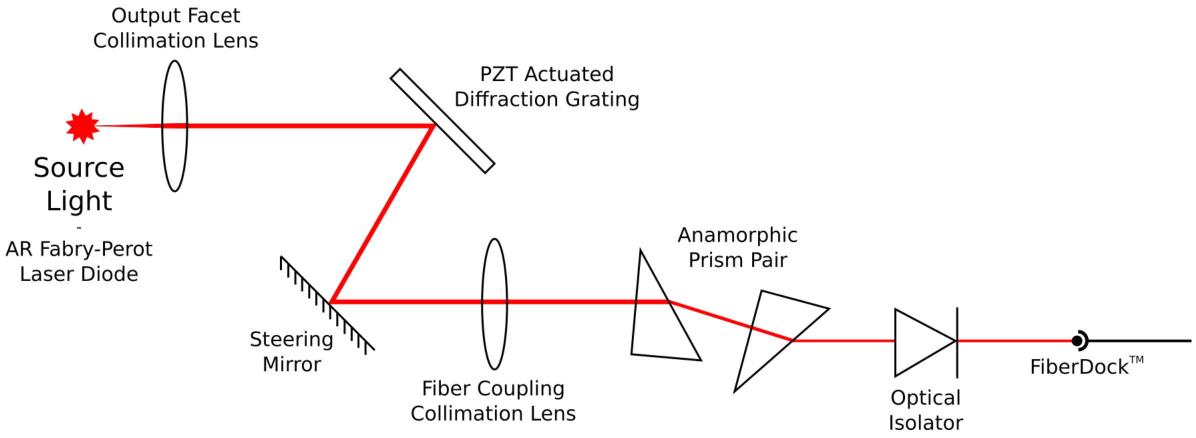

Figure 5.3: The extended cavity and optical setup for the DL-100 lasers used in our experiment. The source light is collimated by a lens on the output facet of the diode, and the beam is diffracted by a grating in the Littrow configuration. The light is then reflected by the steeing mirror that is followed by a another collimation lens. This light then passes through an anamorphic prism pair for further beam shaping and sent through an optical isolator. The final step of collimation and beam shaping culminates in coupling the light into a fiber in a compact setup.

5.1 Laser Driver Electronics

5.1.1 DCC 110 and DTC 110

Precise control of the current through the laser diode plays a significant role in the stability of the output of the laser system. Temperature control with the laser diode also plays a major role in the overall stability as well as initial wavelength selection. Each DL-100 laser system includes both a DCC 110 current controller and DTC 110 temperature controller, which will be the focus of this subsection. Each grating stabilized DL-100 requires a SC 110 piezoelectric transducer (PZT) scan control, which will be described in the next subsection.

All DL-100 lasers are grating stabilized, but have been tested to run without the grating to see the natural center wavelength of each laser diode. These will free run at slightly different frequencies when the TEC is held at 20.0^{o}C. For example, our master laser (DL-

100-3172) free runs with no grating stabilization at a wavelength of 1118.6 nm, slave laser #1 (DL-100-3139) runs at 1116.7 nm, and slave laser #2 (DL-100-3140) runs at 1109.6 nm. Lasing thresholds for each free running diode generally sit at or around 61 mA in terms of current controller settings. Threshold values for grating stabilized lasers sit around 95 mA.

Factory specifications usually indicate that testing had occurred with the diodes running at 20.0^{o}C with the grating being able to select the wavelength of the laser over nearly a 100 nm range. This put the 1083 nm output we desire well within the tested parameters of our lasers. The TEC can be set to temperatures anywhere between -10^{o}C and 100^{o}C, but during day to day operations the temperature is kept at a constant 20^{o}C. As described earlier with the DFB laser setup, too high a temperature can play lead to major instabilities in the output of a laser.

Laser ID	Free-Running (mA)	Grating Stabilized (mA)	Temperature (^oC)
3172	66	99	20.0
3139	61	84	20.0
3140	61	96	20.0

Table 5.1: Table of lasing threshold settings for each laser involved in our experiment when free running and grating stabilized. 3172 represents our master laser. 3139 and 3140 represents our two slave lasers.

The DCC current controller provides a linear dependence of the output frequency versus the current sent through the diode. Each diode is tested to operate between the two extreme points, namely the lasing threshold current for the diode that include: the lasing threshold current and the maximum it can handle. Generally, the DCC 110 is one of the lowest-noise current controllers on the market and was shown to provides a -150 MHz/mA profile with a strong linear correlation. This is a factor of two improvement over the previous Thorlabs and ILX Lightwave current drivers used with the DFB diodes that provided a slope of -300 MHz/mA.

5.1.2 SC 110

The piezoelectric transducer (PZT) grating in any of our DL-100 lasers are controlled by individual SC 110 scan control boxes. Given that the DCC 110 and DTC 110 for each laser has been satisfactorily set, the grating for each laser is initially tuned by adjusting the physical mount by hand in the cavity. That will provide the coarse tuning while the SC 110 will provide the fine tuning with its 23 GHz mode-hop free tuning range. Both the frequency locking and phase locking processes involve similar procedures in terms of the primary functions of the SC 110.

The frequency locking process involving the DL-100 designated as the master laser involves tuning grating in order to find the 1083.33065 nm ($J = 1 \rightarrow J = 2$) transition for metastable helium. However, the grating stabilization with the AR Fabry-Perot diode scheme in any of our DL-100 lasers provides the quietness in terms of noise and drift. Day to day operation does not require adjusting the grating mount while tuning the DC offset on the SC 110 is enough to find a particular transition.

The phase locking process involves more control over the signal of one laser's output (slave) in order to find the beat signal between it and another laser (master). As mentioned earlier, the beat signal can really only be seen at the level of a few GHz on a spectrum analyzer. The SC 110 eases the process of tracking down a high frequency beat signal and bringing it down to lower frequency usable in the experiment, and more will be described in the section involving the mFALC.

One key function of the SC 110 involves the hidden connection between the SC 110 and DCC 110 on the electronic supply rack. This function called the feed forward involves the ratio of PZT scan to current scan, which leads to the ability to adjust the current setting of a particular laser through the DC offset adjust on a SC 110. This function plays an important role as a special means of adjusting the mode-hop free tuning range of a particular SC 110.

The output of a laser with a clean PZT sweep with a properly tuned feed forward will show a well-defined mode spacing on a Fabry-Perot interferometer (FPI) and with a clean ramp of the original DC signal sent to a photodiode monitor. An improperly tuned feed forward will lead to gaps in the mode spacing and inconsistencies in the mode peaks on the same FPI scan. In addition, the ramp on the photodiode signal will become distorted corresponding to the distortions seen in the FPI scan.

Adjusting the feed forward involves just this process of monitoring the laser output as the feed forward trimpot is adjusted on the SC 110. In our case, we use a homemade FPI with a free spectral range of 30 GHz along with a Thorlabs DET08CFC 5 GHz bandwidth photodetector. However, day to day operation should not involve adjusting the feed forward along the same lines as adjusting the grating.

5.1.3 Digilock 110

The frequency stabilization setups to this point have all shown that they either cannot maintain a frequency lock to the resonance transition or the lock is stable but includes enough noise to be unable to produce a stable phase lock with a slave laser. The intrinsic frequency oscillation on the output of the DFB only served to provide an added challenge to solidifying the entire stabilization scheme. In addition, the collection of homemade electronics built for previous experiments combined with the assortment of commercially available controllers and generators would result in enough noise to prevent a phase lock between the master and slave lasers from being achieved.

A drastic increase in compatibility and noise reduction was necessary in order for to achieve a phase lock between a master and slave laser while simultaneously having the master laser frequency locked to resonance. Controlling the amount of excess noise produced by a collection of independent electrical components seemed out of reach at this point. This seemed to strongly point towards testing the low noise frequency locking system offered by Toptica, the Digilock 110, which was made available to us for testing before purchase.

One DL-100 laser would act as the master laser while the other laser would remain a slave laser. The goal of this test was to obtain a frequency lock with a low enough modulation depth to the current through the DL-100 laser diode, which carries as little excess noise as possible such that a phase lock to the slave laser can be achieved. The updated setup can be seen in Figure 5.4.

As per its namesake, the Digilock 110 operates so that the entire locking process can be performed on a computer environment on a virtual oscilloscope. The ”Main In” port accepts a Doppler-free SAS signal while providing a triangular ramp signal as a means of scanning the PZT in the DL-100. The same signal is available for output on through the ”Trigger” port in the form of a synced TTL signal to observe the SAS signal on an external oscilloscope.

Side-of-Fringe Locking

The simplest locking mechanism that can be performed with the Digilock involves locking to the side of a SAS peak with one PID regulator. With two PID regulators available for controlling the feedback either to the PZT scan control (SC110) or the current through the DL-100 laser diode, the user is free to choose which PID regulates the feedback loop. This process is still a manual process since the user chooses all of the settings including the DC level setpoint, P, I and D, and DC offset for the entire lock.

With the setpoint and PID values set to the users needs, the PZT sweep can be turned off and the DC offset can be adjusted to match the setpoint for the PID. At this point the

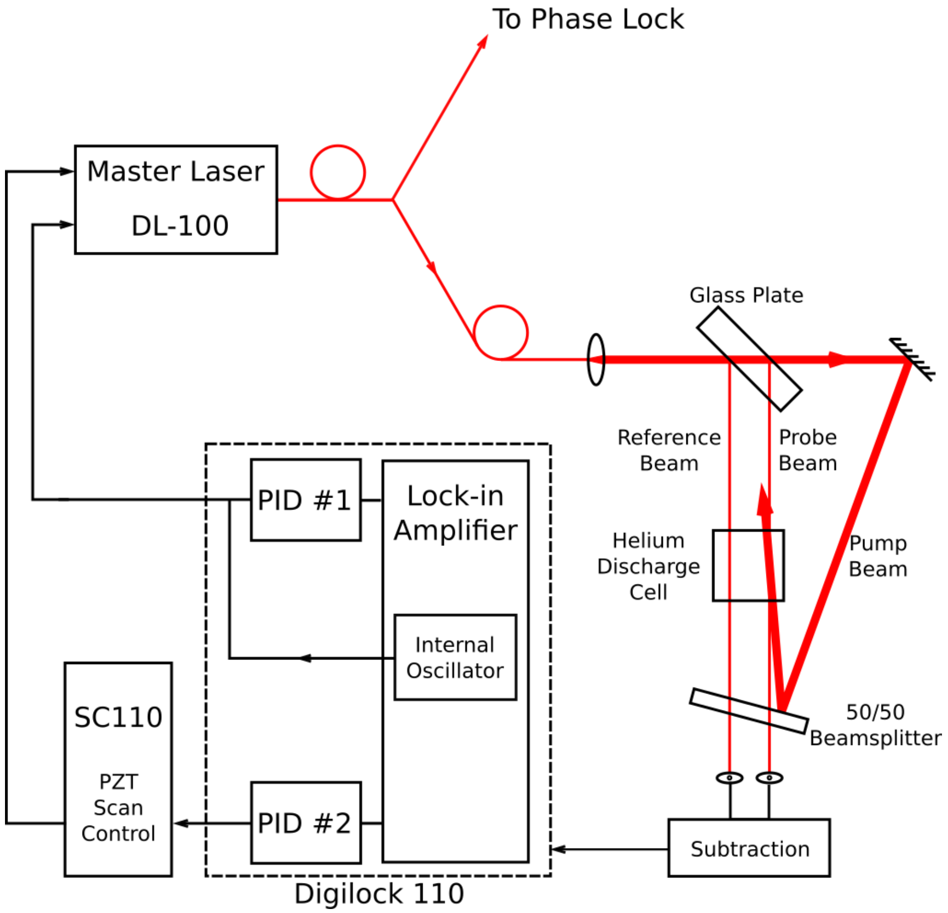

Figure 5.4: The SAS frequency locking setup for the DL-100 lasers including the Digilock system. The difference between this setup and the old DFB setup is the use of two PID regulators with the Digilock compared to just one in the DFB setup. The digilock received the Doppler-free absorption signal from the SAS setup, and its internal lock-in amplifier provides the error signal based on a low-noise frequency modulation of the diode current. Both PID regulators receive the error sigal, make corrections accoridngly, and send the feedback signals to their respective laser components. PID #1 sends signals back to the current modulation electronics connected to the laser head. PID #2 sends signals back to the PZT actuated grating.

feedback loop can be activated for the PID settings to take their effect. Any adjustments can be made iteratively to manually achieve the most stable lock.

In addition, this manual setup can be supplemented by an automated where the user determines the setpoint and the Digilock manages the rest of the process in terms of matching the DC offset. The user is still free to select the PID settings freely to satisfy their conditions of a stable lock.

Digilock Lock-in Amplifier

The Digilock contains its own lock-in amplifier, no different from any conventional model, in order to produce a standard error signal based on a Doppler-free SAS signal. The one limitation this system possesses lay within the modulation frequency where it is limited to discrete steps of even fractions of 781.25 kHz. During the locking process, a modulation frequency closest to the one chosen by the user is determined by the system. For example, when a 7 kHz modulation was chosen. The system searched for the closest frequency matched these discrete steps and found 6.98 kHz. The amplitude of the modulation can be adjusted freely with precision to 0.0001 V_{PP}.

This system also possesses the ability to optimize phase relationship of the error signal through an automated iterative process of adjusting the input phase shift. As a result, 0 and π shifts will show anti-symmetric error signals while $\pi/2$ and $3\pi/2$ shifts will show no signal. With a zero crossing through the top of the resonance peak established, the top-of-fringe locking process can begin.

Top-of-Fringe Locking

Not unlike the AutoLock with the side-of-fringe setup, the top-of-fringe setup can be performed in a similar manner with the AutoLock given the optimization of the lock-in amplifier settings for "locking to an extremum". One or both PID regulators can be used in this case with the lock-in output being sent to either, which allows each to find the top of the SAS peak. In the case of both PID regulators operating simultaneously, the Digilock will determine the DC level of the top of the peak and send this information to both regulators.

The low-depth modulation provided by the lock-in amplifier in a system already designed to reduce excess electronic noise to a minimum allows us to accomplish a frequency lock based on a direct current modulation, similar to the original DBR setup. With the Digilock setup including the DL-100 as a master laser, it became possible to achieve a stable phase lock to a slave laser for much longer than the 10 minute runs the eventual ARP experiment demands.

This lock is simultaneously supplemented through stabilization of the PZT actuation to maintain the DC offset of the frequency lock to the top of resonance. Although this is a separate PID regulator, both regulators are connected to the same lock-in amplifier and utilize the same error signal for making corrections. Video tutorials for this locking process can be found online at Ref. [27].

5.2 Phase Locking

The heart of this project is contained mostly within the circuitry of the mixed Fast Analog Linewidth Controller (mFALC) that carries the responsibility of establishing the phase locked loop (PLL). The phase locking process begins with individually adjusting the frequency ramp and amplitude of the sweep produced by the SC 110 going into a particular slave laser's PZT. The frequency can be adjusted by a 10 position selector switch with discrete ramp outputs ranging from 0.4 Hz to 10 kHz. Adjustments in the amplitude will naturally dictate the overall signal strength of the scan, where zero ramp amplitude will result in no apparent scanning. Note that the logarithmic nature of the amplitude scaling leads to a scan over a GHz in the output of a DL-100

Initially, the two lasers that are to be phase locked will likely have frequencies that differ by several GHz, which exceeds the 2.5 GHz maximum frequency visible on our spectrum analyzer. Ideally, by this point, the master laser is stabily frequency locked to resonance.

Finding the beat signal then requires scanning the PZT on the slave laser such that its output frequency is scanned over a range of several GHz. This way, the beat signal will appear when the PZT oscillation periodically sweeps the beat frequency within the 2.5 GHz range of the spectrum analyzer.

From here, it's necessary to adjust the DC offset for the slave laser's PZT control so that it can show up on the spectrum analyzer without an oscillation placed on the PZT. As the beat signal is eased to within the visible range of the spectrum analyzer, the scan amplitude can be turned down to show the true center of the beat signal. Once the beat frequency becomes visible on the spectrum analyzer, the scan amplitude can be turned to zero along with the PZT scan. The last step is to adjust the DC offset for the beat signal so that its frequency matches the local oscillator frequency.

Once these conditions are met, the scan amplitude can be reduced to zero and the resulting beat signal should not longer be undergoing any oscillations given the stability of the lasers. The beat signal frequency can still be adjusted with the DC offset to fall in the 10 MHz to 200 MHz capture range possible for the mFALC. A local oscillator signal (LO) will provide the reference for the mFALC phase lock while the PID feedback loop is handled by a differentiator component along with a series of integrator circuits designed to handle various signal speed ranges. Achieving a lock involves adjusting the specific frequency windows for each integrator and differentiator in order to narrow the capture window of the PLL in terms of the LO frequency.

5.2.1 Mixed Fast Analog Linewidth Controller

The beat signal between the two lasers will produce a sum and difference based on their respective frequencies, the sum frequency becomes a parasitic and unnecessary component of of the mixer. Thus, it becomes important to filter out this component to avoid any unwanted phase noise that may arise as a result. Otherwise, the PID regulator in the mFALC will continue maintaining the phase lock. A general depiction of this feedback loop can be seen in Figure 5.5 [28].

The general design of a PLL circuit includes the following components:

- The phase-frequency detector in the system is a double-balanced mixer that compares the frequency between the input frequency (IF) and local oscillator (LO) in order to determine the phase present in the beat signal. The output of the mixer provides a phase error signal that includes the zero-crossing point representing the in phase condition, and the rest of the electronics in the feedback loop make corrections to the signal in order to lock the IF to always be in phase with the LO.

- An internal low pass filter [system] for eliminating any parasitic high frequency components of the mixed signal.

- An op-amp based lag-lead compensator (PID regulator) that integrates and smooths the processed signal to provide stability for the locking process by adding phase feedback. This is discussed in further detail in the section 5.2.2.

- A voltage controlled oscillator (VCO) for providing the correction signals fed back to the phase-frequency detector at the beginning of the loop. As the detected phase error increases, the voltage applied to the VCO will provide a signal to iteratively correct for such error with successive completions of the loop. A voltage applied in the opposite manner will exacerbate the phase error and prevent a lock from being achieved.

Each of these circuits involves lag and lead compensators that act in combination to smooth and amplify the incoming signal for a target frequency (LO) while simultaneously

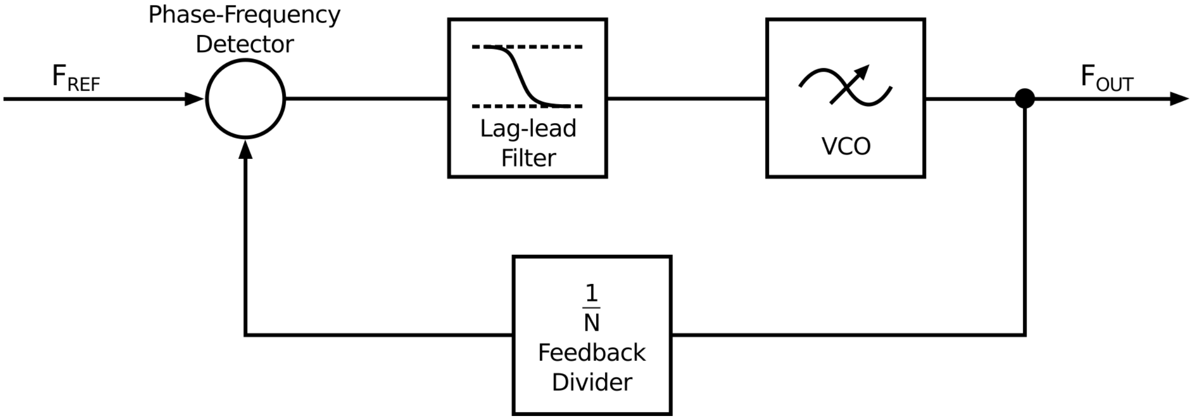

Figure 5.5: A basic description of a phase locked loop setup. The input signal is sent through a phase-frequency detector and produces an error signal, and a VCO further down the circuit line receives correction signals from the charge pump based on the error signal and returns the signal through a negative feedback loop to the beginning of the circuit. A divider is shown here to that can exist in other systems as a means of locking to scaled down reference frequencies. Figure based on Ref. [28].

controlling the phase shift the signal undergoes as it is fed through these circuits and eliminating any undue noise surrounding the desired signal in the frequency domain. A phase lock for our system can be successfully achieved with the following functions available on the mFALC: the fast (FLI), slow (SLI), and extra slow limited (XSLI) integrators along with the fast limited differentiator (FLD).

5.2.2 Brief Overview of Compensators

In control theory, compensators play a major role in a variety of applications that help improve any unwanted signal fluctuations including but not limited to: automobile design, aeronautics, or robotics. A PID controller involves a combination of several differentiators (lead) and integrators (lag) filters that provide correction signals based on frequency error that arises in the system. In addition, these compensators will respectively provide positive and negative phase feedback to the system that in order to improve the stability of the loop.

Once a signal falls within the capture region of the phase lock loop circuitry, it will stay locked as long as strong phase noise doesnt interrupt the feedback process [29].

Lead (PD) compensators

For a standard PID setup, the derivative term serves to predict the future behavior of the system based on calculating the time derivative of the error signal to find any rate of change corresponding to new error. PD refers to the compensator carrying the proportional-derivative terms in the PID controller. The correction signals from the PID are then sent to the VCO in the PLL circuit and fed back to the mixer, and can also be adjusted to fit the needs of the user.

Lead compensators provide a positive phase advance to the system over a frequency range falling between two corner frequencies. Positive phase addition maximizes to π radians at $1/\sqrt{a}$ times the upper corner frequency while falling to zero on either side. Here, a refers to the gain factor for the compensator, which ties into the location of the lower corner frequency relative to the upper corner frequency, and T refers to the period of the frequency. The upper corner frequency refers to the higher gain side located at $1/T$ rad/sec while the lower corner refers to the lower gain side located at $1/aT$ rad/sec. [30].

The differentiator in the mFALC PID loop behaves as a lead compensator designed to handle the high frequency component of the input signal with a lower corner frequency as low as 19 kHz and an undefined upper corner frequency depending on the selection. The setting with the highest and well-defined upper corner frequency sits at 4.8 MHz. This differentiator also acts as a high-pass filter based where the user is able to select the corner frequencies for the circuit.

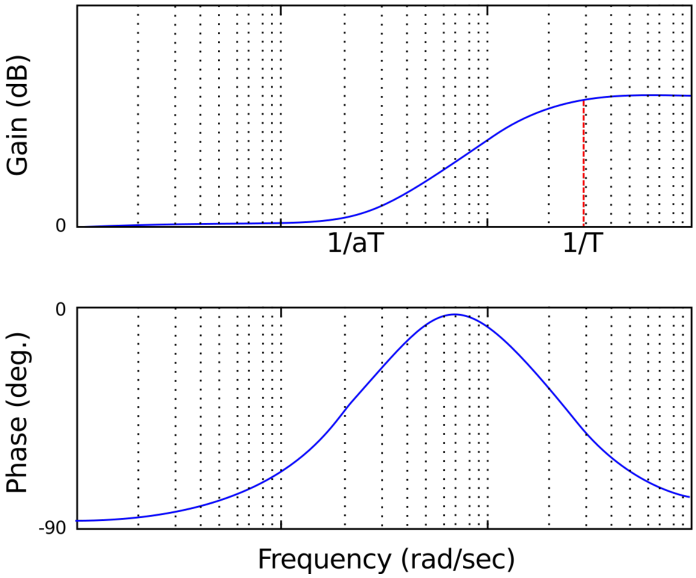

Figure 5.6: General frequency and phase response for a lead compensator. The center of the rolloff sits at $1/\sqrt{aT}$. The maximum negative phase added to the control loop usually occurs at this frequency as well. Figure based on Ref. [28].

Lag (PI) compensators

The lag compensators act like any integral term in a standard PID setup where it looks at past signal errors that should have been corrected by integrating the instantaneous error over time. PI refers to the compensator carrying the proportional-integral terms in the PID controller. Each of these can also be adjusted to optimize the frequency-phase response for specific frequency ranges of the input signal.

Lag compensators also provide a positive phase advance to the system over a frequency range falling between two corner frequencies. The magnitude of the negative phase addition maximizes to $-\pi$ radians at $1/\sqrt{a}$ times the upper corner frequency while rising to zero on either side [30]. Just as with the lead compensator, the upper corner frequency for the lag compensator is located at $1/T$ rad/sec, and the lower corner frequency is located at $1/aT$ rad/sec.

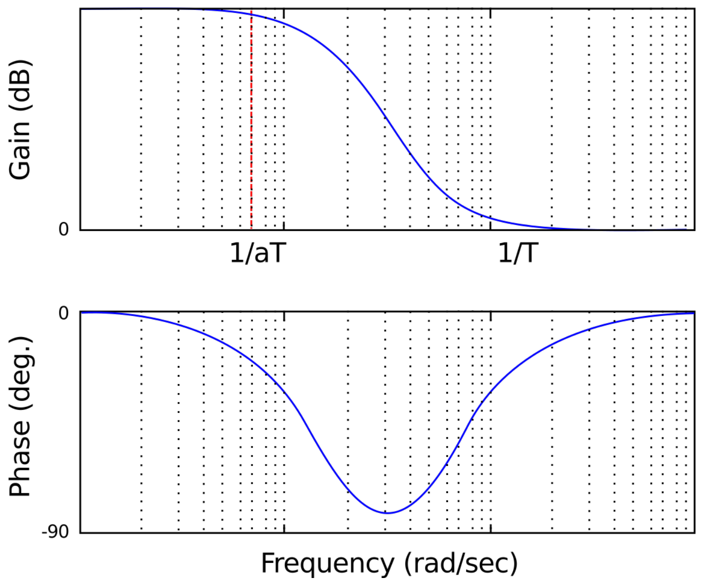

Figure 5.7: General frequency and phase response for a lag compensator. The center of the rolloff sits at $1/\sqrt{aT}$. The maximum negative phase added to the control loop usually occurs at this frequency as well. Figure based on Ref. [28].

The three integrators in the mFALC PID loop behave as lag compensators. These components as a whole cover a frequency range starting with an upper corner frequency as low as 0.9 Hz and an lower corner frequency as high as 7.5 MHz. Each integrator also acts as a low-pass filter for their respective frequency ranges.

Phase Margin

Phase margin needs to be mentioned here as it plays a significant role in the stability of a feedback loop such as this. This margin is defined as 180^o - $|\phi|$ where ϕ represents the overall phase added to the system by each compensator. At unity gain (0 dB), the feedback in the system will remain positive, but a large enough phase shift will result in a negative feedback that will stabilize loop [29].

As the phase margin for the system is improved, so is the damping term in the overall PID setup. Too low a phase margin can then lead to a weak damping and unnecessary oscillations in the system as the positive feedback regime is entered. In terms of the PID design, Lag compensators generally improve upon the loop gain for lower frequencies in the system while lead compensators tend to increase the stability of the system by adding to the phase margin [29] [30].

Lag-Lead (PID) compensator

The Toptica mFALC compares the phase between two AC signals with a double balanced mixer. The output of the mixer contains a signal that has the original two input signals superimposed on each other. A similar mixing process was performed earlier in the frequency down conversion setup for frequency stabilizing the DFB laser. However, an error signal is produced in this case to phase lock the beact signal to a specific local oscillator frequency.

The PID settings on the mFALC consists of the lag-lead compensator (filter) combination mentioned earlier that includes three integrators (lag) and a differentiator (lead). In combination, the lag-lead filter serves another function as a low-pass filter whose -6 dB/octave rolloff point can be adjusted. The goal of this making adjustments to this setup was to find the rolloff frequency that corresponds to the frequency variations in the system. However, the rolloff needs to be at a low enough frequency so that the loop can keep up with these variations [29].

Each subsection provides the possible configurations of each compensator component along with the rolloff frequencies calculated based on the corner frequencies for each setting. In addition, the maximum possible phase shift achievable at these corner frequencies are listed.

5.2.3 Toptica mFALC Components

Extra Slow Limited Integrator (XSLI)

The XSLI covers the lowest frequency range windows of 90 Hz to 2000 Hz down to 0.9 Hz to 20 Hz. This circuit can also be set to have a completely flat frequency response such that little or no amplification (rated to 0 dB) is performed. The frequency response for each setting can be seen in Figure 5.8 and Table 5.2.

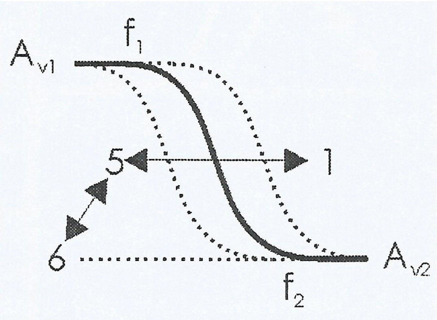

Figure 5.8: The bode plot for the XSLI showing the corner frequency response for settings #1 to #5 and the flat response from #6. A_{v1} represents the relative amplitude of the signal (f_1) able to pass through, and A_{v2} represents the relative amplitude of the signal (f_2) that is filtered by the integrator [31].

	$A_{v1} = 26$ dB	$A_{v2} = 0$ dB			
Switch #	f_1 (Hz)	f_2 (Hz)	a	Max Phase (deg)	Max Phase Freq. (Hz)
1	90	2000	22.22	-66.05	424
2	25	600	24.00	-66.93	122
3	9	200	22.22	-66.05	42.4
4	2.5	60	24.00	-66.93	12.2
5	0.9	20	22.22	-66.05	4.25
6	-	flat response	0.00	0.00	-

Table 5.2: Table of corner frequencies for each setting on the extra slow limited integrator (XSLI). The flat response from #6 is selected for both slave lasers in our setup.

Slow Limited Integrator (SLI)

The SLI covers the lowest frequency range windows of 5 kHz to 300 kHz down to 11 Hz to 650 Hz. Just like the XSLI, this circuit can also be set to have a completely flat frequency response with a constant 1.6 dB amplification maintained. The frequency response for each setting can be seen in Figure 5.9 and Table 5.3.

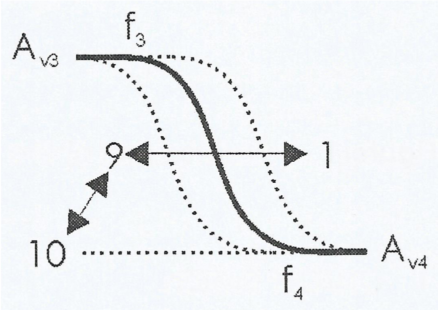

Figure 5.9: The bode plot for the SLI showing the corner frequency response for settings #1 to #9 and the flat response from #10. A$_{v3}$ represents the relative amplitude of the signal (f_3) able to pass through, and A$_{v4}$ represents the relative amplitude of the signal (f_4) that is filtered by the integrator [31].

	A$_{v3}$ = 37 dB	A$_{v4}$ = 1.6 dB			
Switch #	f_3 (Hz)	f_4 (Hz)	a	Max Phase (deg)	Max Phase Freq. (Hz)
1	5k	300k	60.00	-75.29	38.7k
2	2.4k	140k	58.33	-75.08	18.3k
3	1.1k	65k	59.09	-75.18	8.45k
4	500	30k	60.00	-75.29	3.87k
5	240	14k	58.33	-75.08	1.83k
6	110	6.5k	59.09	-75.18	845
7	50	3k	60.00	-75.29	387
8	24	1.4k	58.33	-75.08	183
9	11	650	59.09	-75.18	84
10	-	flat response	0.00	0.00	-

Table 5.3: Table of corner frequencies for each setting on the slow limited integrator (SLI). The flat response from #10 is selected for both slave lasers in our setup.

Fast Limited Integrator (FLI)

The FLI covers the lowest frequency range windows of 1.4 kHz to 10 kHz up to 650 kHz to 7.5 MHz. The flat response selectable for the FLI works on the opposite voltage amplification end of the Bode plot, which intends to maintain a steady 15 dB amplification maintained. The frequency response for each setting can be seen in Figure 5.10 and Table 5.4.

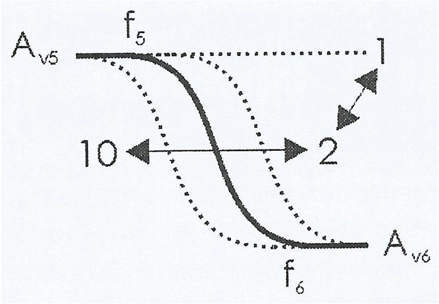

Figure 5.10: The bode plot for the FLI showing the corner frequency response for settings #2 to #10 and the flat response from #1. A_{v5} represents the relative amplitude of the signal (f_6) able to pass through, and A_{v6} represents the relative amplitude of the signal (f_6) that is filtered by the integrator [31].

	A_{v5} = 15 dB	A_{v6} = -6 dB			
Switch #	f_5 (Hz)	f_6 (Hz)	a	Max Phase (deg)	Max Phase Freq. (Hz)
1	-	flat response	0.00	0.00	-
2	650k	7.5M	11.54	-57.19	2.21M
3	300k	3.5M	11.67	-57.36	1.02M
4	140k	1.6M	11.43	-57.04	473k
5	65k	800k	12.31	-58.18	228k
6	30k	370k	12.33	-58.21	105k
7	14k	170k	12.14	-57.98	48.9k
8	6.5k	80k	12.30	-58.18	22.8k
9	3k	37k	12.33	-58.21	10.5k
10	1.4k	10k	7.14	-48.97	3.74k

Table 5.4: Table of corner frequencies for each setting on the fast limited integrator (FLI). The flat response from #1 is selected for both slave lasers in our setup.

Fast Limited Differentiator (FLD)

The FLD covers a range of frequencies with an unlimited upper limit as seen in 5.5. The flat response that can be chosen here works in the same manner as the XSLI such that a 0 dB amplification should be expected. The frequency response for each setting can be seen in Figure 5.11 and Table 5.5.

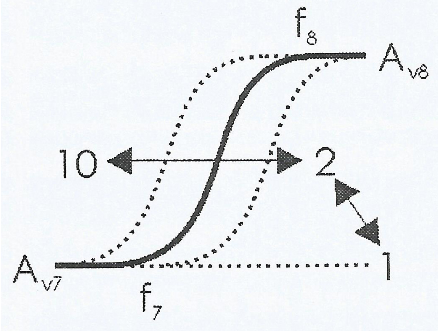

Figure 5.11: The bode plot for the FLD showing the corner frequency response for settings #10 to #2 and the flat response from #1. A_{v7} represents the relative amplitude of the signal (f_7) that is filtered by the integrator, and A_{v8} represents the relative amplitude of the signal (f_8) able to pass through [31].

	$A_{v7} = 0$ dB	$A_{v8} = 15$ dB			
Switch #	f_7 (Hz)	f_8 (Hz)	a	Max Phase (deg)	Max Phase Freq. (Hz)
1	-	flat response	0.00	0.00	-
2	8.5M	*	-	-	-
3	4.2M	*	-	-	-
4	1.9M	*	-	-	-
5	900k	4.8M	5.33	43.17	2.08M
6	420k	2.3M	5.47	43.72	982k
7	190k	1M	5.26	42.90	436k
8	90k	480k	5.33	43.17	208k
9	42k	230k	5.48	43.72	98.2k
10	19k	100k	5.26	42.90	43.6k

Table 5.5: Table of corner frequencies for each setting on the fast limited differentiator (FLD). Switch #5 is chosen for both slave lasers in our setup.

For settings #2 to #4, there is no well defined upper corner frequency as indicated by the *, which naturally leads to problems understanding at what frequency the amplification occurs. When any of these settings are selected, the mFALC is no longer able to capture the beat signal and lock it. When setting #5 is chosen, which has a defined upper corner frequency, a stable phase lock is achieved with a beat signal that becomes amplified well above the observed noise floor. Setting #6 provides a similar result with a lock that is slightly less stable lock as the slower kHz frequencies begin to pass through.

5.3 Phase Locking Results

The resulting configuration that appeared to be optimal involved completely flat frequency responses from all of the integrator components (XSLI #6, SLI #10, and FLI #1) leading to the only amplifying component becoming the fast limited differentiator (FLD, set to position #5). With this setting, the FLD is set to have corner frequencies of 900 kHz and 4.8 MHz at the low and high frequencies respectively and a 15 dB amplification for signals of 4.8 MHz and beyond.

However, for settings #1 to #4 for the FLD that has no well defined upper limit in terms of a corner frequency, the feedback loop shows that it is not captured let alone maintain a phase lock. The specifications for the FLD suggest that for these high frequency settings, the upper corner frequencies fall beyond the value of the input signal and lead to little or no amplification such that locking cannot be achieved. A well defined corner frequency that allows signals between 10 MHz and 200 MHz as suggested in the specifications seems necessary.

The primary goal for this upgrade was to achieve a phase lock between each slave laser and a frequency locked master laser to a fixed local oscillator (LO) frequency. In other words, the LO defines the fixed frequency offset between the slave and master laser. Again, for the

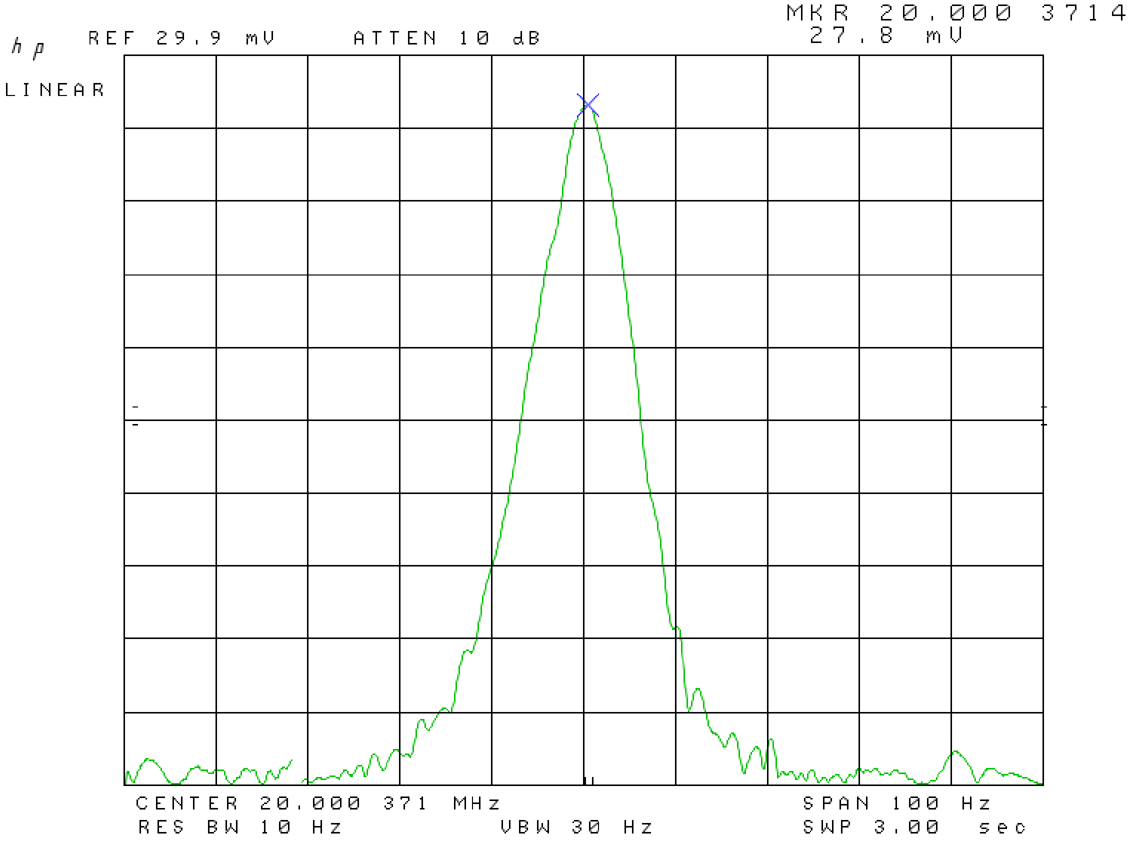

Figure 5.12: The phase locked beat signal as seen on our RF spectrum analyzer on a linear voltage scale. The marker shows that the center of the peak sits at 160.0028454 MHz while the local oscillator frequency in this case was set to 160.00000 MHz. With a bandwidth resolution of 10 Hz over a 100 Hz span, the width of the peak is ∼18 Hz.

experiment, one slave laser is set to a detuning, δ, above resonance where the master laser is frequency locked and the other to δ below resonance.

The upgrade has shown success where, at the very least, a coherent phase lock can be achieved with a linewidth on the Hertz level as seen in Figure 5.12, but with room for improvement in terms of understanding sources of noise and introducing automation for detuning the slave lasers when making ARP force measurements. These future considerations are discussed in the final section of this thesis.

As mentioned earlier, certain frequencies dominate parts of the lockable 10 to 200 MHz region that provide difficulties in achieving a successful phase lock. The 10 MHz clock signal that seems to originate from either the RF spectrum analyzer or oscilloscopes largely eliminates the possibility of achieving a phase lock at an already unstable region for the mFALC circuitry. In addition, the 51 MHz signal used for the helium discharge cell for the SAS lock provides another unstable region for phase locking.

The LO signal can be set to these frequencies with the intent of producing a phase lock, but the result is usually the inability to lock as the original LO signal is overpowered by the external signal at the same or nearby frequency. The phase lock ultimately became stable enough for use in the experiment, but this and other phase noise in the system remains a part of the system in all likelihood simply due to the imperfections present with each laser diode.

The overall quality of the phase locking loop (PLL) can be gauged in different ways, depending on how critical the stability of a particular system is to its parent system. The linewidth of the PLL in the Fourier spectrum can provide some general insights into the characteristics of the lock, albeit in a crude but quick manner. In our case, this was a starting point for understanding any phase noise that was present in our system. Quantifying phase noise in a more complete manner would tell a better (not perfect) story of the quality of our lock based on where noise is most likely to appear in the frequency domain.

In terms of linewidth, the 10 Hz width of the beat signal was scanned with a 10 Hz bandwidth resolution while locked. Our initial reaction to this effect was to synchronize the 10 MHz clock signals that individually drive the spectrum analyzer and function generator. The result of synchronizing these clocks by having the function generator operate on the 10 MHz clock from the spectrum analyzer produced only a minor change. In a broader sense for the experiment, this offset should play an insignificant role in terms of the wavelength where our lasers operate (276.732... THz) or even at the level of the LO frequency (20 to 160 MHz). Ultimately, the hold time for each phase lock to the slave laser is the primary concern for the experiment.

In general, for waveform sources, phase noise could be measured as a comparison between a stable reference light source and a test source [32]. On an RF spectrum analyzer with a phase lock already achieved between a stable master laser and either slave laser, phase noise can be directly measured by comparing the power of a sideband compared to the power of the entire carrier signal.

By looking at several parts of the beat signal while phase locked for several different LO frequencies, the phase noise could be characterized over the range of possible parameters for a lock. However, only a range between 10 MHz and 200 MHz limits the possible detuning for either slave laser, which means an external solution will be necessary to produce a higher frequency detuning. This will be discussed further when looking at future considerations that will make the experimental setup more complete.

Quantifying phase noise needed this method to directly measure on a spectrum analyzer the level of noise away from the Fourier peak center. However, compared to much more modern spectrum analyzers, our HP 8566A RF spectrum analyzer does not carry any new computerized tools for quickly integrating and normalizing marker measurements to 1 Hz bandwidths. A GPIB connection to an external computer through the KE5FX GPIB toolkit provided the means for communicating with our spectrum analyzer, and the Phase Noise measurement utility provided an automated means of gathering single sideband phase noise data.

The program will accept a carrier signal with a specified amplitude and center frequency, and will then proceed to iteratively scan through orders of magnitude in terms of frequency from 10 Hz up to 1 MHz. (Starting and ending frequencies can be chosen freely to suit the user's purposes.) Raw data is gathered on a linear frequency scale and dBm scale for amplitude, where a conversion takes place to represent the strength of phase noise with respect to the carrier signal (dBc). On the frequency axis, the spectrum analyzer can only scan with a resolution of 10 Hz at best. Thus, by taking into account the bandwidth resolution for a scan over a particular region of interest, the data can be normalized to show the amplitude of a point away from the carrier center per Hz. As a result, the strength of the observed phase noise is represented as dBc/Hz.

$$\mathcal{L}(f) = \frac{\text{Power over 1 Hz bandwidth}}{\text{Power of carrier frequency}} \tag{5.1a}$$

$$\mathcal{L}(f) = 10 \log \left[\frac{1}{2} \frac{\Delta\phi^2_{rms}(f)}{B} \right] \tag{5.1b}$$

Frequency (Hz)	Avg. Power (dBc)	Std. Dev. Mean (dBc)
10	-53.1218	2.1463
100	-51.8443	0.6576
956.8724	-56.0082	0.9419
1000 (sideband)	-27.7342	2.1277
2473.006 (sideband)	-47.6246	0.9451
7967.562 (sideband)	-43.7094	1.1401
10000	-65.6512	1.7866
100000	-76.4566	0.5971
500000 (sideband)	-60.3267	4.0993
983187.2	-73.9672	2.7110

Table 5.6: Table of phase noise data that accompanies Figure 5.13. The power of the phase noise relative to the carrier frequency was measured for each order of magnitude increase in frequency along with any prominent sidebands that appeared.

$\Delta\phi^2_{rms}$ represents the square of the rms deviation in phase at a frequency f away from the carrier center (f_0) within a defined bandwidth B [33].

The general expectation was met, namely that further away on the frequency domain

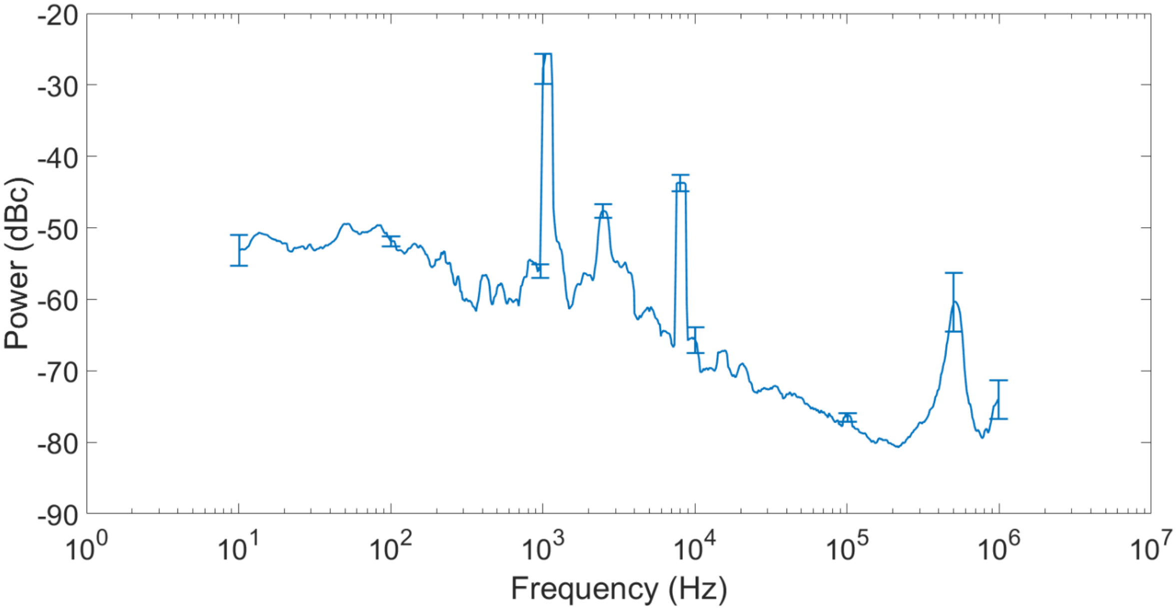

Figure 5.13: The phase noise data gathered for a beat signal phase locked for 160 MHz. Error bars have been placed at each order of magnitude in terms of frequency (10 Hz, 100 Hz, 1 kHz, etc.) along with locations with any strong sideband signals. Of these sidebands, the only one with a definitive source sits at 7.967 kHz from the frequency modulation used for frequency stabilizing our master laser. The strongest of the unexplained sidebands sits at 1 kHz, which overlapped with the order of magnitude measurement points so a nearby point was obsevred at 958 Hz to measure the noise floor around the sideband.

from the locked center, less noise is observed. A strong sideband signal of -27.73 ± 2.12 dBc consistently appeared at a 7.967 kHz offset from the center frequency with the likely source of this being the frequency modulation applied to the master laser for its stabilization process. When looking just 50 Hz away from either side of this sideband signal, the noise seen falls below the -50 dBc and phase noise continues to fall as the offset frequency is increased.

The jitter (signal timing error) present in the signal is calculated based on a approximated summation of the phase noise taken over the same frequency ranges described. Since the data is not taken over a continuous spectrum, it becomes necessary to perform a Riemann sum as opposed to an integral [33].

$$T_{rms-jitter} = \frac{10^{\mathcal{L}(f)/20}}{\sqrt{2}\pi f_0} \tag{5.2}$$

This jitter can also be seen on an oscilloscope trace of the beat signal in the form of a sinusoidal signal oscillating on the time domain. For a perfect beat signal or "clock", this sinusoid will not show this jitter, and a Fourier transform would be an infinitely thin line. Again, the real signal will show a broadened peak as a result of the phase noise present in the system, and the RMS jitter was calculated to be 3.06 ± 0.16 s. In the phasor perspective, the RMS jitter in radians was calculated to be 115.6 ± 6.6 mrad given an average carrier amplitude of -16.73 ± 0.45 dBm.

The noise that we have measured seems small relative to the rest of the carrier signal, but the phase lock is imperfect and will not hold infinitely. The more prominent source of issues regarding the stability of the PLL stems from either the behavior of the feedback signals from the master laser's frequency lock or any sound vibrations present in the lab that can translate to strong disturbances to the PZT for any of the lasers involved in the experiment. In terms of damping noise from the surrounding lab environment, vibration isolation for the lasers of some form will likely prove invaluable for increasingly longer periods of taking data.

The PID settings for the master laser's frequency lock are generally set to produce as low a feedback signal as possible while maintaining a lock so that it doesn't indirectly affect the phase locking process to follow. As a result, the modulation depth is minimized to or below 0.005 mV, such that an error signal with a clear dispersion relation and zero crossing is produced. However, part of the problem that has been overcome but still appears is the 10 kHz modulation frequency used for the lock-in procedure for frequency stabilization that will appear as sidebands on the phase lock spectrum signal. It seems to be a necessary evil in the grand scheme of the laser system, where the low modulation depth still makes the phase locking scheme possible, but is also minor in comparison to the issues encountered with the DFB system.

Chapter 6

Preliminary Results on ARP Forces

The goal of the laser system upgrade described in this thesis is to show an improvement over the previous experimental results regarding the velocity dependence of the ARP force. Optical forces on the order of 32 times the radiative force are predicted in our simulations with no spontaneous emission present. With the effects of spontaneous emission considered, the same simulations have shown forces of $16F_{rad}$ are possible. However, the largest that has been seen experimentally with a two laser setup was on the order of 6 to $7F_{rad}$ [7]. A one laser setup has produced forces on the order of $12F_{rad}$ [6] [19], and the maximum force that could be expected from the simulations was $16F_{rad}$.

Discrepancies arose between the simulation and experimental results that led to questions this thesis hoped to answer that involve the nature of phase during the ARP process. What happens if the phases of the ARP pulses are not synchronized when interacting with the atoms? How is spontaneous emission handled during this process? Is there a clock for spontaneous emission that resets each time the atom decays back down to the ground state? How are the atoms reacting to multiple ARP sequences?

The results from Ref. [7] still showed that the atoms experienced optical forces significantly larger than the radiative force. However, the deflection pattern that were seen in the simulations from detuning the lasers gradually off resonance in opposite directions could not clearly be seen in the experimental results. To reiterate the original problem, we suspect that the use of two independent lasers that likely led to phase incoherent ARP pulse sequences despite respectively having linewidths on the order of 200 kHz play an important role. Based on previous results, it seems that this issue of phase coherence leads to a factor of 2 loss in ARP force strength. This section will describe the steps taken to re-calibrate the setup, and early results gathered from the addition of the phase locking upgrade.

6.1 Velocity Dependence of the ARP Force

Following the benchmark testing of the entire experiment with the single beam setup, the tests for the velocity dependence of the ARP force could begin. The setup would change to the include all three lasers and the simultaneous frequency and phase locking scheme described earlier as seen in Figure 3.6. The results of the upgrade can be seen in Figures 6.1 and 6.2.

Each laser has a linewidth of ∼100 kHz while the phase lock for either pair of lasers is as narrow as ∼20 Hz. As discussed earlier, the phase lock between the slave and master lasers will usually jump after several minutes due to any number of reasons including: acoustic vibrations, brief moments of instability in the frequency lock, electrical noise, etc. Nonetheless, the lock lasts for more than enough time to take data that shows atoms were deflected while a phase lock was achieved.

A bright line persistently appears on the phosphor screen as undeflected He* atoms and light from the helium source reach the detector. The plasma from the source emits UV light that produces a fluorescence similar to that of the He* atoms. In addition, the path taken through the vacuum system by both He* atoms and UV light are identical, which makes these two indistinguishable from each other on the phosphor screen with no apparent force. However, a strong enough ARP force will deflect atoms far enough away from the UV line to make this distinction.

Based on the parameter space found to produce the largest ARP force with the single beam setup, we expected similar results to be produced by the two laser setup. However, initial results showed a drastic decrease in the force at the parameters that produced strong forces with a single laser ($\Omega_0 = 4.77\omega_m$, $\delta_0 = 3.02\omega_m$) while showing a similar strength force when both slave lasers had no detuning off resonance albeit not phase locked. In order to investigate the parameter space, the strength of the force, and the effect of phase locking, the experimental setup could be temporarily reconfigured.

The two laser scheme could be reconfigured to provide a means of measuring the strength of the ARP force with an effective phase lock of 0 Hz. This involved frequency locking the master laser to the usual helium resonance followed by phase locking one of the slave lasers to the master to a stable frequency above resonance. The second slave laser then could be used to phase lock to the first slave laser to the same frequency below resonance, which should effectively provide a phase lock with the master laser having zero detuning from resonance. Thus, we could measure the strength of the ARP force in the π-pulse condition.

Returning to the two-laser setup, the π-pulse condition was tested again, but this time to characterize the decrease in the strength of the ARP force as the slave lasers are detuned from resonance by even a few MHz. The lineout can be taken from a series of snapshots of the phosphor screen for the strongest observed force from each image. This is compiled to compare the strength of the average ARP force to the simulated velocity experienced by the atoms based on the detuning of the slaves lasers.

Our initial findings show that a large ARP force on the order of $4F_{rad}$ is observable with

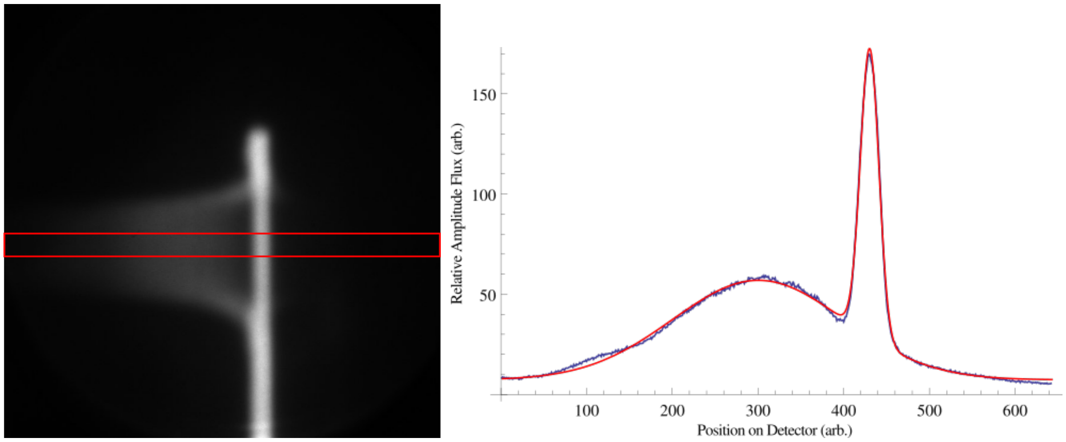

(a) Phosphor Screen Image (b) Phosphor Screen Lineout

Figure 6.1: Part (a) shows the raw image taken by our CCD camera focused in on the part of the phosphor screen where the atomic beam was directed. The bright line in the image defines the starting position of the deflected atoms by placing a 250μm slit in our vacuum system. The red box in (a) indicates the region of interest for a force readout, which is averaged together to produce the lineout seen in Part (b).

the upgraded setup as seen in Figure 6.1a. A vertical slit placed inside our vacuum system defines the starting position of the atoms on the phosphor screen after the MCP. The CCD camera is set to focus on the region of interest where only the slit and deflected atoms are captured.

A thin red rectangle seen in the phosphor screen image represents the section of maximum force observed in the data. These points are averaged together to produce a lineout of the force based on detector position accompanies the raw data (Figure 6.1b). A series of phosphor screen images are gathered in a single data run that covers a velocity range of ±200 m/s in steps of 1 m/s. The images are compiled to a plot comparing the strength of the ARP force against the simulated Doppler velocity. The most striking difference from previous results is a new resemblance to the numerical simulations that pointed towards the velocity dependence we see now (Figure 6.1).

With phase incoherent light, we see a noticeable breakdown in this velocity dependence where it resembles the results seen in the previous experimental setup that did not include a phase locking mechanism. These results were gathered by having one slave laser phase locked to the master laser as with the phase coherent data. The second slave laser was phase locked to a far less stable local oscillator signal produced by a VCO. Selecting LO frequencies to match the other slave lasers detuning, the VCO signal was mixed with another RF source. As a result, this second slave laser would not be phase matched to its counterpart. At this point, we need to keep investigating the effects of this phase instability and its effects on the atoms in terms of interaction time. If the phase jitter here is too slow, then the atoms may not have the opportunity to see it and be affected by it. Nonetheless, there are definitely points of a strong force as seen in Figure 6.2, but the dependence on Doppler velocity seems to disappear without phase coherence.

The overall strength of the force still falls well below the theoretical maximum of $\sim 16F_{rad}$ when the effects of spontaneous emission are considered in the simulations. Again, a single laser setup has shown it is possible to produce a force of $\sim 12F_{rad}$, which we understand as having absolute phase coherence. Our new experimental results have shown a force of $\sim 4F_{rad}$. We are still exploring the effects of adjusting the interaction time of the He* atoms and the beam, and also may still require further adjustments in the optical setup. There are also slight disagreements in the parameters for the maximum force with regards to Ω_0 and δ_0. This may also mean that the experimental or simulation parameters require some retooling as we further explore the ARP force map with our new setup. We are also yet to observe any peak splitting in the velocity map seen in the simulations, but we so far have only explored a small part of the possible force map.

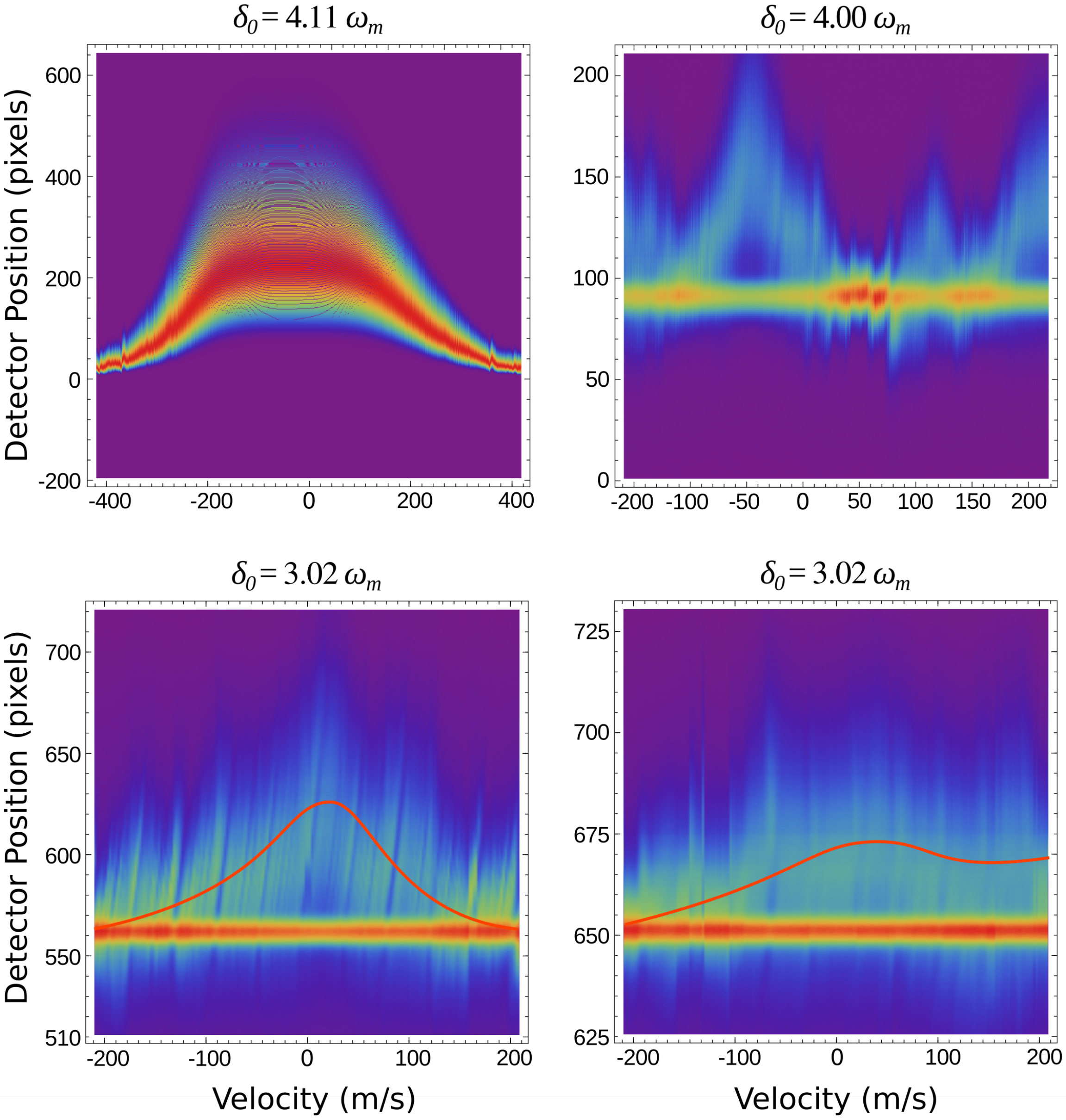

Figure 6.2: The images in the top row represent the numerical simulation results (left) and experimental results (right) from the previous setup. The images in the bottom row represent the new experimental results taken with our new setup. The left image involves phase coherent light while the right image was taken with phase incoherent light. The red lines are simply guides for the viewer to gauge the strength of the force. We now see similarities in the velocity dependence of the ARP force with the simulation results with the phase locking upgrade to the experimental setup. The phase incoherent results also seem to resemble the old experimental results.

6.2 Future Consideration

6.2.1 VCO sweep and Phase Stability

As a means of automating the data taking process, the local oscillator (LO) frequency could be swept such that the phase lock for each slave laser can subsequently be swept over a tunable frequency range. The goal here would be to find mFALC settings capable of sustaining a phase lock for a moving LO signal, such that a single data set can include a wide range of detunings. The previous experiment involved manually moving the detuning for each laser, recording a run, and iteratively repeating the process to cover the detuning range that would show a velocity dependence of the ARP force.

This scheme was briefly attempted with limited success, and fell short of the sweep range demanded by the experiment. The widest sweep range with a stable phase lock maintained was ∼2 MHz while an ∼8 MHz sweep range could be performed with phase locking intermittently maintained. Ramps of 0.01 Hz, 0.025 Hz, and 0.05 Hz could be translated into a 2 MHz sweep seen by the slave laser. Unfortunately, the phase lock would almost always jump due to the abrupt change in direction by the beat signal as it oscillated. In addition, as the sweep range widened, the added phase noise by the VCO placed too great a hurdle for the mFALC to even just capture the beat signal and keep up with the moving LO. As it stands, it seems unlikely that a VCO will provide the hundreds of MHz and upwards of GHz range sweeps necessary for the experiment. Given that the mFALC seems to operate best when set to lock to a single LO frequency along with the prescribed 200 MHz limit, a different solution may be necessary . Exploring the effects of phase stability will continue to play an important role in fully comprehending the nature of the ARP force. We have managed to show clear differences between trials of phase coherent and incoherent ARP light, but more will become clear as the rest of the force map is further explored with our new setup. As it stands, the VCOs may not be providing phase noise that it fast enough for the atoms to react within the given interaction time. Injecting phase noise into the system from an external source may help if this behavior needs to be characterized. However, the effects such a process will have on the phase locking system are currently unknown.

6.2.2 AOM sweep

Another possible means of adding automation involves the slave laser beams being sent through acousto-optic modulators (AOMs) in order to externally produce the detunings, as opposed to internally sweeping the LO signal. With this setup, both slave lasers can be confidently phase locked to the master for much longer than the 5 minute limit required for the experiment, and both slave lasers can be detuned without sacrificing the stability of the PLL. Power loss will undoubtedly be a concern with multiple passes through an AOM, but with two individual slave lasers that may be counteracted along with the Booster Optical Amplifier already in place for the pulse production section of the existing setup.

The difficulty with this scheme involves synchronizing the detuning through two AOMs simultaneously along with the possible need to double-pass in order to maximize the detuning. A possible solution has been seen before in Ref. [34] in the case of a single beam split into two and each arm of double-passed through individual AOMs to achieve upwards of a 450 MHz detuning on each side. Power loss is mitigated by the use of a fiber amplifier before the splitting and modulation process, which is also a possible option if power becomes too much of a concern.

6.3 Conclusion

This thesis has described the installation of a new laser system that improved the previous experimental setup for studying the velocity dependence of the ARP force. We have been able to simultaneously achieve a frequency lock to an atomic reference with our master laser operating at 1083.33 nm while also being able to phase lock two independent slave lasers to the master laser. The phase lock for a particular master-slave laser pair could be adjusted to have a specific detuning above or below resonance. The second slave laser could be phase locked to the exact opposite detuning as its counterpart, which provides a simulated Doppler shift for the He* atoms in our experiment.

This upgrade provides the foundation for addressing issues associated with the previous iteration of the ARP force experiment as discrepancies arose between the numerical simulations and experimental results. In particular, questions began to arise regarding the role of phase coherence during the absorption-stimulated emission process as an atom interacted with light. At the moment, it's difficult to conclusively determine the effectiveness of the phase locking mechanism due the the intrinsic stability of the DL-100 lasers compared to the old DBR lasers used in the previous setup for this experiment. In principle, the phase locking mechanism is the means for providing the phase coherence between our lasers that should strengthen the ARP force; however, our new lasers themselves are far less sensitive to electrical noise and climate fluctuations. As a result, these lasers are less prone to frequency drifts in their outputs, and such an improvement in performance seems to overshadow the effects of the phase locking. Although not every question may be answered by this upgrade, the role of phase in the overall strength of the ARP force should become much clearer as continue to explore our possibilities.

Bibliography

[1] D. Wineland and H. Dehmelt. *Bull. Am. Phys. Soc.*, 20:637, 1975.

[2] T. Hänsch and A. Schawlow. *Op. Comm.*, 13(1):68–71, 1975.

[3] D. Wineland and W. Itano. *Phys. Rev. A*, 20(4):1521–1540, 1979.

[4] H. Metcalf and P. van der Straten. *Atoms and Molecules Interacting with Light.* Cambridge University Press, Cambridge, 2016.

[5] M. Cashen and H. Metcalf. Optical forces on atoms in nonmonochromatic light. *J. Opt. Soc. Am. B*, 20:915, 2003.

[6] D. Stack. *Optical Forces from Periodic Adiabatic Rapid Passage Sequences on Metastable Helium Atoms. PhD. Dissertation.* PhD thesis, Stony Brook University, 2012.

[7] J. D. Elgin. *Study of the Velocity Dependence of the Adiabatic Rapid Passage (ARP) Optical Force in Helium. PhD. Dissertation.* PhD thesis, Stony Brook University, 2015.

[8] P.W. Milonni and J.H. Eberly. *Lasers.* Wiley, New York, 1988.

[9] H. Metcalf and P. van der Straten. *Laser Cooling and Trapping.* Springer, New York, 1999.

[10] C. S. Corder. *Optical Forces on Metastable Helium. PhD. Dissertation.* PhD thesis, Stony Brook University, 2014.

[11] R. Feynman, F. Vernon, and R. Hellwarth. Geometrical representation of the schrödinger equation for solving maser problems. 28(1):49–52, 1957.

[12] W. Phillips and H. Metcalf. *Phys. Rev. Lett.*, 48(9):596–599, 1982.

[13] A. Abragam. *The Principles of Nuclear Magnetism.* Oxford Univ. Press, Oxford, 1961.

[14] D. Sawicki and J. H. Eberly. Perfect following in the adiabatic limit. *Optics Express*, 217(4), 1999.

[15] L. P. Yatsenko, S. Guérin, and H. R. Jauslin. Topology of adiabatic passage. 65:043407, 2002.

[16] Daniel Stack, John Elgin, Petr M. Anisimov, and Harold Metcalf. Numerical studies of optical forces from adiabatic rapid passage. *Phys. Rev. A*, 84:013420, 2011.

[17] H. Metcalf and P. van der Straten. *Laser Cooling and Trapping.* Springer, 1999.

[18] X. Miao, E. Wertz, M. G. Cohen, and H. Metcalf. *Phys. Rev. A*, 75:011402, 2007.

[19] X. Miao. *Optical Forces on Atoms with Periodic Adiabatic Rapid Passage Sequences. PhD. Dissertation.* PhD thesis, Stony Brook University, 2006.

[20] P.F. Chapman R. Tiberio. Ingaas-gaas-algaas laterally-coupled distributed feedback (lc-dfb) ridge laser diode. *Electronics Letters*, 30:1058–1060, 1994.

[21] M.G. Moharam and L. Young. Criterion for bragg and raman-nath diffraction regimes. *Applied Optics*, 17:1757–1759, 1978.

[22] J.S. Major Jr. and D.F. Welch. Singlemode ingaas/ gaas distributed bragg reflector laser diodes operating at 1083nm. *Electronics Letters*, 29:2121–2122, 1993.

[23] R.W. Tkach and A. R. Chraplyvy. Regimes of feedback effects in 1.5 micron distributed feedback lasers. *Journal of Lightwave Technology*, 28:93–108, 1992.

[24] P. Samutpraphoot and V. Vuletic. Passive intrinsic-linewidth narrowing of ultraviolet extended-cavity diode laser by weak optical feedback. *Optics Express*, 22:11592–11599, 2014.

[25] Michael G. Littman and Harold J. Metcalf. Spectrally narrow pulsed dye laser without beam expander. *Applied Optics*, 17:2224–2227, 1978.

[26] J.S. Wilson A.S. Arnold and M.G. Boshier. A simple extended-cavity diode laser. *Review of Scientific Instruments*, 69:1236–1239, 1997.

[27] This can be found at http://www.toptica.com/products/tunable-diode-lasers/laser-locking-electronics/digilock-110-digital-locking/. A series of short video tutorials for understanding and operating the Digilock system.

[28] Mike Curtin and Paul O'Brien. Phase-locked loops for high-frequency receivers and transmitters. *Analog Dialogue*, 33:9–18, 1999.

[29] P. Horowitz and W. Hill. *The Art of Electronics.* Cambridge University Press, Cambridge, 1998.

[30] D. Maksimovic and R. Erickson. *Fundamentals of Power Electronics.* Springer, New York, 1997.

[31] Operation manual for the Mixed Analog Fast Linewidth Contoller (mFALC) provided by Toptica Photonics, Inc.

[32] M. Zhu and J. Hall. Stabilization of optical phase/frequency of a laser system: application to a commercial dye laser with an external stabilizer. *J. Opt. Soc. Am. B*, 10:802–816, 1993.

[33] B. Lorbeer. Phase noise measurements of the new master oscillator for ttf2. Master's thesis, Fachhochschule Lubeck, 1998.

[34] Andrew Chieda, Michael and E E Eyler. Bichromatic slowing of metastable helium. *Physical Review A*, 86(5):053415, 2012.